LEABHARLANN CHOLÁISTE NA TRÍONÓIDE, BAILE ÁTHA CLIATH | TRINITY COLLEGE LIBRARY DUBLIN
Ollscoil Átha Cliath | The University of Dublin

Terms and Conditions of Use of Digitised Theses from Trinity College Library Dublin

Copyright statement

All material supplied by Trinity College Library is protected by copyright (under the Copyright and Related Rights Act, 2000 as amended) and other relevant Intellectual Property Rights. By accessing and using a Digitised Thesis from Trinity College Library you acknowledge that all Intellectual Property Rights in any Works supplied are the sole and exclusive property of the copyright and/or other IPR holder. Specific copyright holders may not be explicitly identified. Use of materials from other sources within a thesis should not be construed as a claim over them.

A non-exclusive, non-transferable licence is hereby granted to those using or reproducing, in whole or in part, the material for valid purposes, providing the copyright owners are acknowledged using the normal conventions. Where specific permission to use material is required, this is identified and such permission must be sought from the copyright holder or agency cited.

Liability statement

By using a Digitised Thesis, I accept that Trinity College Dublin bears no legal responsibility for the accuracy, legality or comprehensiveness of materials contained within the thesis, and that Trinity College Dublin accepts no liability for indirect, consequential, or incidental, damages or losses arising from use of the thesis for whatever reason. Information located in a thesis may be subject to specific use constraints, details of which may not be explicitly described. It is the responsibility of potential and actual users to be aware of such constraints and to abide by them. By making use of material from a digitised thesis, you accept these copyright and disclaimer provisions. Where it is brought to the attention of Trinity College Library that there may be a breach of copyright or other restraint, it is the policy to withdraw or take down access to a thesis while the issue is being resolved.

Access Agreement

By using a Digitised Thesis from Trinity College Library you are bound by the following Terms & Conditions. Please read them carefully.

I have read and I understand the following statement: All material supplied via a Digitised Thesis from Trinity College Library is protected by copyright and other intellectual property rights, and duplication or sale of all or part of any of a thesis is not permitted, except that material may be duplicated by you for your research use or for educational purposes in electronic or print form providing the copyright owners are acknowledged using the normal conventions. You must obtain permission for any other use. Electronic or print copies may not be offered, whether for sale or otherwise to anyone. This copy has been supplied on the understanding that it is copyright material and that no quotation from the thesis may be published without proper acknowledgement.

Novel transparent conducting oxides for application in solar cells

A thesis submitted to the University of Dublin Trinity College in application for the degree of Doctor of Philosophy by

Elisabetta Arca

School of Physics
Trinity College

October 2012

I declare that this thesis has not been submitted as an exercise for a degree at this or any other University and it is entirely my own work. Unpublished and published work of others, are duly acknowledged in the text wherever included

I agree to deposit this thesis in the University library open access institutional repository or allow the library to do so on my behalf, subject to Irish Copyright Legislation and Trinity College Library condition of use and acknowledgment.

Thesis 10000

Summary

In the present thesis deposition and characterization of transparent conducting oxides (TCOs) have been explored. The coexistence of transparency and conductivity in a material is often regarded as an unusual property, since transparent materials are most likely to be insulating while conductive materials are generally quite absorbing. This remarkable property can be easily achieved in wide band gap semiconductors, for which a band gap higher than 3 eV ensures transparency to the visible light while conductivity can be induced by doping, either intrinsic or extrinsic. Among the TCOs, n-type doping has been so far the most successful. In_2O_3:Sn, SnO_2:F and ZnO:Al are the most commonly used n-type TCOs in commercial devices. These materials have been studied, at least, for the past 50 years, both from the theoretical and applicative point of view, therefore their performance have been rather optimized. On the other hand, p-type TCOs are much more recently developed and their performance are much lower than their n-type counterpart. In particular, new and improved materials are required. The ultimate goal of the present thesis was to develop a new p-type transparent conductive oxide with comparable or improved performance with respect to those reported in literature. In order to do that, screening for material composition and deposition conditions was required. This could be performed by using spray pyrolysis, a flexible and versatile deposition technique. An in house system was built up for this purpose, with the aim of allowing high throughput. However this implies that material with lower quality than those produced by more sophisticated techniques such as sputtering or chemical vapour deposition would be produce. Therefore, it was necessary to assess the limit in the performance achievable with this particular set up for known materials. The abundant literature production available for ZnO:Al and SnO_2:F made them a suitable case study for this purpose. This offers, at the same time, the opportunity to study the effect of different deposition conditions and in particular the role of chemical processes on the properties of deposited films. The first system to be studied was ZnO and ZnO:Al. A direct correlation between the solvent used for the deposition and the texturing of the deposited ZnO was

determined. Morphology as well as optical and electrical properties were correlated to the decomposition pathway of both solvents and salts. At the same time, the dependence of structural and optical properties upon concentration of Al were studied. In particular a decrease in the refractive index of the material was observed as a consequence of increasing Al concentration. At the same time, a progressive destruction of the long range crystalline order was observed, and, as a result, the material was progressively getting x-ray amorphous. According to the simulation performed by Dr.Karsten Fleischer this material is suitable as internal anti-reflecting layer to minimize the optical loss due to refractive index mismatch at the glass/TCOs interface in solar cells. This study on ZnO:Al allowed determination of the optimum deposition conditions which were than used to test a new fluorine precursor, benzenesulfonyl fluoride, for the deposition of SnO_2:F. Finally, the deposition of a new p-type TCO was attempted. In order to do that Cr_2O_3 was chosen as a suitable candidate. Both cation and anion doping was performed. The role of the cation was to improve the electrical properties while the role of the anion was to improve the optical properties by modifying the band structure, in particular the top of the valence band. Mg was the most effective cation dopant while N was used as anion dopant. The effect of the different deposition conditions, in particular the role of the salts and of the chemical additives (acids) was studied and a correlation was found between them and the electrical properties. The effect of the nitrogen on both optical and structural properties was investigated. To this end, undoped Cr_2O_3 was deposit by both PLD and MBE, with the aim of comparing the properties of high quality epitaxial films with respect the polycrystalline films grown by spray pyrolysis. Ellipsometric analysis was performed on the epitaxial films and the dielectric function was determined. Significant difference was found between the two. Following the absorption coefficient was compared with respect to that extracted fromtransmission measurements on undoped and nitrogen doped Cr_2O_3. The absorption coefficient of the films deposited by PLD coincide with that extracted for undoped Cr_2O_3 deposited spray pyrolysis, whilethat of the films deposited by MBE is close to that of N-doped films. An attempt to explain these finds has been given.

Acknowledgments

I would like to thanks Prof. Igor Shvets for the opportunity of pursuing my PhD studies under his supervision, for the economical and scientific support. Without his help this PhD studies could not be possible.

I would like to thanks Dr. Karsten Fleischer for the scientific and moral support given to me during these years. I cannot be more grateful for all the time he spent instructing me and for the genuine collaborative attitude he always showed me.

I would like to thanks Prof. James Lunney for the possibility of using the PLD deposition system, Dr. Karsten Rode, Inam and Geroid for the help given in taking care of the instrumentation.

I would like to thanks Dr. Sumesh Sofin, for the pressure support with the MBE and XRD.

I would like to thanks all the present and past members of the Applied physics group, in particular Dr. Cormac Luke O'Coileain, for his friendship and support throughout these years and Dr. Victor Usov for his help.

I would like to thanks Mr. Christopher Smith, for the ellipsometric measurements.

I would like to thanks Dr. Cormac McGuinness, Martin and Steve for been always so helpful in taking care of the XPS apparatus.

I would like to thanks Lina, for all the coffees and laugh we shared, I really, really enjoyed them.

Grateful acknowledgments go to Dr. David Scanlon, for the extremely fruitful discussions and for being always so available for explanations: theoretical calculations are always helpful! Many thanks go to Aefoe and Prof. Greame Watson as well, for the DFT investigation of some of these experimental results.

Many thanks go to Dr. Jean-Christian Bernerde and Prof. Linda Cattin, for their collaboration and for host me in their laboratories in the Nantes University: it was a pleasure to work with you.

Un grazie speciale và ai miei genitori e a Nadia per tutto il supporto e l'affetto, senza di voi non ce l'avrei mai fatta, non potrò mai ringraziarvi abbastanza. Grazie anche a Cristiano e Maria, per il tutto supporto e l'affetto grazie mille di cuore.

Table of content

List of symbols...*i*

List of figures...*ix*

List of tables...*xii*

List of publications...*xiii*

1. Introduction

1.1. Transparent conducting oxide: an overview..........................1

1.2. Outline of this thesis..3

2. Fundamental properties of transparent conductive oxide

2.1. Coexistence of optical and electrical properties: the band structures of a TCO..7

2.2. Electrical properties..11

2.2.1. Hall effect..17

2.3. Optical properties and their correlation with the electrical properties.. 18

2.4. Concluding remarks..26

3. Experimental apparatus

3.1. Introduction..30

3.2. Deposition methods..30

3.2.1. Spray pyrolysis..31

3.2.2. Pulse laser deposition..34

3.3. Characterization..36

3.3.1. Electrical characterization..37

3.3.2. Optical properties..39

3.3.3. Compositional analysis..42

3.3.4. Morphology..43

3.3.4.1. Atomic force microscope (AFM)..43

3.3.4.2. Scanning electron microscope (SEM)................44
3.3.5. Structural analysis...44
3.3.5.1. Powders X-ray diffraction in parallel beam geometry.. 45
3.3.5.2. Grazing incidence X-ray diffraction (GIXD).........47
3.3.5.3. High resolution x-ray diffraction (HRXRD).........49
3.3.6. Thickness determination.......................................50
3.3.6.1. X-ray reflectivity (XRR)..................................51
3.3.6.2. Cross-sectional Scanning Electron Microscopy (SEM) 53

4. N-type TCOs

4.1. State of the art...57
4.2. Zinc oxide and Aluminum Zinc Oxide (AZO)......................58
4.2.1. Effect of the chemical precursors on the properties of deposited film...60
4.2.2. Role of the solvent...61
4.2.3. Role of the precursors salts....................................68
4.2.4. Conclusion...75
4.3. Modification of standard ZnO for usage as internal anti-reflecting layer: introduction 77
4.3.1. Characterization of heavily aluminate ZnO to be used as internal anti-reflecting coating..................................79
4.4. Tin oxide and Fluorinated Tin Oxide (FTO).........................83
4.4.1. An alternative fluorine precursor for the synthesis of FTO: benzenesulfonyl fluoride...85
4.4.2. Results and Discussion..87
4.4.3. Conclusion...95

5. P-type TCOs

5.1. P-type TCOs: state of the art...103
5.2. Dopability of p-type TCO..108

5.2.1. Deposition of new and alternative material: a strategic overview..111
5.3. Cr_2O_3: crystal structure and band structure 112
5.4. Cation-anion doping on Cr_2O_3 by spray pyrolysis................115
5.4.1. Spray pyrolysis deposition of Cr_2O_3:(Mg,N): a new p-type transparent semiconductor....................................116
5.4.2. Effect of the defect chemistry on the properties of Cr_2O_3 grown by spray pyrolysis.....................................125
5.4.3. Determination of the nitrogen content by XPS............131
5.4.4. Conclusion on the growth and doping of Cr_2O_3 by spray pyrolysis..135
5.5. Deposition of undoped and Mg-doped Cr_2O_3 by PLD..............136
5.5.1. Target preparation and thin film deposition................136
5.5.2. Ellipsometric determination of the Cr_2O_3 dielectric function 142
5.6. Conclusions on the optical and electrical properties of undoped and doped Cr_2O_3...149

6. Concluding remarks and future prospective.

6.1. Conclusions and outlook..156

Appendix

A.1DFT calculations of the band structure of Cr_2O_3 and $Mg:Cr_2O_3$..159

List of symbols

a_0	Bohr radius
a^*	reciprocal space lattice parameter
a_f	lattice parameter of the epitaxial film
a_s	lattice parameter of the substrate
$\vec{B}$	magnetic flux
B_n	Debye-Waller factor
C_{ii}	elastic constant for longitudinal waves
d	layer thickness
e	elementary charge
E	energy
E_g	band gap
E_F	Fermi energy
$\vec{E}$	electric field
$\vec{F}$	Lorentz force
F	Figure of merit
f	complex atom form factor
f_n	atomic scattering factor
F_K	structure factor
H_T	Haze parameter
J	current density
I	intensity
I_0	initial intensity
h	Plank constant
k	wave vector
k	extinction coefficient
L_K	Lorentz polarization factor
m^*_c	carrier effective mass
m_e	free electron mass
m_K	multiplicity of the reflex
n_e	number of electron carriers
n_h	number of hole carriers

N	number of donor or acceptor impurities
N_A	Avogadro number
N_i	number of electrical scattering centers
N_{SC}	number of optical scattering centers
n_c	Mott critical density
n_D	number of dopant
n	refractive index
P_K	polarization factor
P_{MD}	March-Dollase parameter
q	phonon wave vector
q_D	charge state of a dopant
r_p	parallel component of the Fresnel reflection coefficient
r_s	perpendicular component of the Fresnel reflection coefficient
R_{sh}	sheet resistance
R_H	Hall coefficient
R	reflectance
S_F	x-ray beam intensity
T	temperature
T	transmittance
t_c	critical thickness
T_{diff}	Diffuse transmittance
T_{tot}	Total transmittance
v_d	drift velocity
V_H	Hall voltage
Z	valence number
α	absorption coefficient
β	absorption term
δ	dispersion term
ΔE	excess energy
Δ_{BM}	Band gap opening due to Burstein moss shift
ΔH	enthalpy of formation
Δ_{RN}	Band gap renormalization
ε_0	permittivity of the free space

ε_m	dielectric constant of a material m
ε_1	real part of the complex refractive index
ε_2	imaginary part of the complex refractive index
ε_∞	high frequency dielectric constant
ρ	resistivity
ρ_e	ellipsometric ratio
μ	mobility
μ_V	Hall mobility
μ_D	chemical potential of the dopant
μ_H	chemical potential of the host
σ	conductivity
σ_{SC}	scattering cross section
ω	frequency
ω_p	plasma frequency
τ	relaxation time
λ_{mfp}	mean free path between travel by a charged carrier between two seceding scattering events
λ	wavelength

List of figures

Figure 2.1 An idealized representation of a semiconductor with both top of the valence band and bottom of the conduction band parabolic.

Figure 2.2 The electron density as a function of temperature. 3 different regions are identifiable: the freeze-out region, the extrinsic region and the intrinsic region. Taken from ref.9

Figure 2.3 A schematic representation of impurity doping for the case of Indium tin oxide (ITO). Taken from ref. 10

Figure 2.4 Schematic view of the coulomb scattering process of an electron by means of a positively charged ion. The scattering cross-section is a function of the parameters b, K and ΘTaken from reference 7

Figure 2.5.Schematic view of the scattering process of an electron by means of (a) an acoustic phonon, (b) an optical phonon. Taken from ref. 7

Figure 2.6 Dependence of the mobility values upon the carrier concentration for different scattering mechanism: μ_N, μ_{gb}, μ_{iis} represents respectively the mobility dependence if the scattering mechanism is due to neutral impurities, grain boundaries or ionized impurities. μ_{tot} represent the upper value of mobility achievable if all of the above are taken into account

Figure 2.7 A schematic representation of the Hall bar.

Figure 2.8 Schematic representations of (a) direct and (b) indirect band gap semiconductor

Figure 2.9 Consequence of degeneracy on the optical properties of semiconductors: the fundamental band gap Eg is open up due to the Burstein-Moss shift. However due to the renormalization effect, the widening is reduced. Taken from ref. 25

Figure 2.10 Effect of the carrier concentration on the Drude tail position. Taken from ref. 29

Figure 2.11 Effect of the morphology on the optical properties of the material. Surface roughness attenuates the intensity of the light in the forward direction as part of the light gets scattered in all direction.

Figure 3.1 On the left: the spray-pyrolysis deposition apparatus; on the right the schematic representation of the pyrolysis process. The effect of the droplet size distribution is highlight.

Figure 3.2 The PLD deposition chamber and a schematic view of the process.

Figure 3.3 Schematic representations of (a) the linear configuration set-up, (b) the Van der Paw geometry used for resistance measurements,(c) the van der Paw geometry used for Hall measurements.

Figure 3.4 A schematic view of the optical process that is used for spectroscopic ellipsometry: a monochromatic linearly polarized light is elliptically polarized upon reflection with intensity difference ($\tan\psi$) and phase difference (Δ). To the courtesy of Mr. C. Smith

Figure 3.5 Schematic view of a photoelectron experiment. It is important to notice that sample and spectrophotometer must be in electrical contact in order for the Fermi levels to align 24.

Figure 3.6 The Bruker D8 discover diffractometer in two different configuration: on the left the powders and high resolution configuration with the PSD detector; on the left the grazing incidence configuration with the Soller slits and scintillation counter detector.

Figure 3.7 Schematic view of the grazing incidence diffraction configuration for analysis of polycrystalline films

Figure 3.8. Scheme of the diffraction geometry for high resolution measurements of epitaxial films deposited on single crystal sapphire.

*Figure 3.9.*Scheme of the x-ray reflection process at the top and the bottom of a thin film.

Figure 4.1 Crystal structure and band structure calculation of ZnO. Taken from 24

Figure 4.2 Effect of the solvent composition on the crystallographic (a) and optical (b) properties of ZnO: (A) 100%water, (B) 75%water - 25% methanol, (C) 50% water-50% methanol, (D) 25% water – 75% methanol, (E) 100% methanol.

Figure 4.3 SEM top view of ZnO:Al (Zn:Al=98.5:1.5)in three different solvents; (a) water, (b) a mixture (50:50) of water and methanol, (c) methanol.

Figure 4.4 An example of Fabry-Perot oscillations for a sample with a thickness of 615 nm.

Figure 4.5 Oxygen concentration as a function of time for spraying of water (dotted line), methanol (solid) and a mixture of water/ethanol (30/70, dashed). The significant drop in the case of the organic solvents is caused by the oxygen consumption due to the burning process.

Figure 4.6 XRD patterns of the sample grown by employing a mixture of ethanol/water (70/30) as solvent and zinc chloride as precursor. The peaks are relative to the phase ZnClOH

Figure 4.7 On the left (a) the specular optical transmission of ZnO:Mg samples grown by using different Mg precursors: (solid curve) magnesium acetate, (dotted) magnesium chloride. On the right (b) the specular transmission for ZnO:Al grown employing aluminum isopropoxide (dotted curve) aluminum nitrate (dashed curve) and aluminum chloride (solid)

Figure 4.8 SEM cross sections of ZnO:Al sample grown by using water as a solvent(left) or methanol (right). The in-depth view shows the presence of rings due to the evaporation of water droplets which are not present for methanol grown films.

Figure 4.9 On the left: resistivity values for a large set of samples as a function of the layer thickness. Full symbols are for as deposited samples while open symbols are for post-annealed samples. Different shapes are representative of the different Al precursors and Al concentrations used: ◀Chloride (2%), ▲Al(acac)$_3$ (2%), ■Al(acac)$_3$ (1.5%), ♦Al(acac)$_3$ (1%). On the right, the mobility and carrier concentration as a function of thickness. All samples are grown by using Al(acac)$_3$ as precursors except for the samples with a thickness of 75 nm for which chloride was used as Al source

Figure 4.10. XRD patterns of $Zn_{1-x}Al_xO_y$: (—) x=15, (—) x=20, (—)x=30, (—)x=50. As the content of Al increases, the crystallinity of the film decreases.

Figure 4.11. Change in the refractive index and extinction coefficient with increasing Al concentration: (—) ZnO, (—) $Zn_{70}Al_{30}O_y$, (—) $Zn_{50}Al_{50}O_y$, (—) $Zn_{70}Al_{30}O_y$. The blue line in the refractive index plot is representative of the refractive index of an ideal anti-reflecting coating.

Figure 4.12(a) UV-Visible transmission measurements of $Zn_{1-x}Al_xO_y$ with increasing Al content: (—)x=0.15,(—)x=20,(—)x=30,(—)x=50. It is worth noting that the increase in transmission cannot be attributed to lower thickness. (b) A schematic representation of the way to enhance the efficiency of the cell by using reducing the loss due to reflection: the grey area represents the efficiency of the absorber as calculated by using the weighting function, (– –) transmittance of a glass/TCO stack, (—) transmittance of a glass/ideal AR/TCO stack,(—) glass/real AR/TCO stack .

Figure 4.13. Crystal structure and band structure calculation of SnO2. Taken respectively from 62 and 63

Figure 4.14 UV-visible transmission measurements and XRD patter of SnO_2 samples as a function of temperature and precursors: (—) DBTDA and 753K, (—) DBTDA and 653K. In the inset the band gap was determined via a Tauc plot: (—) SnCl4 and 753K, (—) DBTDA and 753K.

Figure 4.15 XPS spectra of fluorinated tin oxide samples. On the left the F 1s peak is shown, while on the right the Sn $3p^{3/2}$. For the fluorine peak the background has been subtracted and the intensity has been normalized to the $Sn3p^{3/2}$ peak. The inset shows the correlation between the measured carrier concentration and the F/Sn ratio derived from the XPS analysis.

Figure 4.16 XPS spectra of sample REF-1 showing the effect of Ar cleaning: (black dot) the sample before cleaning, (red line) the sample after cleaning.

Figure 4.17 Arrhenius plot of the resistivity versus reciprocal temperature for samples showing a typical metallic behavior: (red line) FTO deposited by using NH_4F, (black dot) REF-1, (blue dashed) REF-2. As the resistivity of the FTO-NH_4F is higher, different range of scale are used.

Figure 4.18 Resistivity vs reciprocal temperature for a set of samples grown using BSF as fluorine source and varying Sn:F ratio in solution: (— 91:9, — 80:20, — 67:33, — 50:50). An offset equal to $\ln(\rho_{min})$ was subtracted to emphasize the change from a behaviour dominated by the metal like carriers to a semiconducting one. The inset shows the dependence of the temperature of transition from metallic to semiconductor behaviour (■) and absolute resistivity (○) on the nominal F:Sn ratios.

Figure 4.19 On the right: exemplary Hall mobility vs temperature data for REF-1. The line shape of the curve is representative for all samples investigated, although absolute values vary. On the left: power dependence of the mobility values upon temperature shows that in the range between 300 and 150 K, the mobility $\mu^{-2/3}$ varies linearly with temperature. Below 150 K mobility becomes independent of temperature.

Figure 5.1 A comparison between the band structures calculated for ZnO (ref 14) and $CuAlO_2$(ref. 15). Notice the difference between the dispersion of the bottom of the conduction band for ZnO in comparison to the top of the valence band for $CuAlO_2$. The band structure and a schematic view of a delafossite structure is reported (ref 16).

Figure 5.2 Schematic depiction of: (a) the dependence of the formation energy of a defect α (with a value of q_D which can be +,0 or -) on the Fermi energy; (b) the formation enthalpy of some intrinsic defect (anion vacancy V_{A+}, cation interstitial C_{i+}, cation vacancy V_{c-}, anion interstitial A_{i-}) on the chemical potential (taken from ref. 29)

Figure 5.3 Crystal structure ((a) the rhombohedral primitive cell and (b) the hexagonal representation) and band structure calculation of Cr_2O_3 (taken from ref. 43)

Figure 5.4. Schematic view of the valence band maximum and conduction band minimum for the case of a charge transfer insulator, where the top of the valence band consist of mainly oxygen p states, with only a small or negligible contribution from the metal d states, and a Mott-Hubbard insulator, where the VBM is mostly composed of metal d states. Taken from ref. 57

Figure 5.5 UV-VIS transmission measurement of undoped Cr_2O_3 and Cr_2O_3:N as a function of N content: undoped Cr_2O_3 (—), Cr:N ratio 1:2 (—), 1:3 (—), 1:5 (—). The Cr:N ratio refers to the precursor solution. A bare substrate was used as a reference.

Figure 5.6 AFM images of the undoped and N doped samples at different nitrogen concentration: (a) undoped Cr_2O_3 (rms = 40 nm), (b) Cr:N 1:2 (rms = 25 nm), (c) Cr:N 1:3 (rms = 50 nm), (d)Cr:N 1:5 (rms = 25 nm).

Figure 5.7 Cross sectional SEM of Cr_2O_3 doped with both nitrogen and magnesium deposited on glass. The thickness of this particular sample was found to be 115±25 nm.

Figure 5.8 Absorption coefficient calculated from transmission measurements and thickness determination from cross sectional SEM and band gap determination for samples grown with different nitrogen content in the solution: (—) no nitrogen in solution, (—) Cr:N ratio in solution 1:3, (—) Cr:N ratio in solution 1:5.

Figure 5.9 Transmittance and band gap determination of amorphous chromium oxide thin films grown by sputtering as a function of nitrogen flow. Taken from ref.55

Figure 5.10 Specular transmission measurements on (—) undoped, (—) Mg-doped and (—)Mg,N-codoped films.

Figure 5.11. Screening process to determine the best compromise between Mg, N and temperature for the deposition. The Figure of merit was used as screening parameter: (▲)[N]=0M and T=753-783K (■) [N]=0.4 M and T=753 K, and (□) [N]=0.4 M and T=753K. The inset shows the figure of merit for Cr_2O_3:(Mg,N) samples grown using [Mg]=0.01 M and T=783K for different [N] concentration.

Figure 5.12 Grazing incidence x-ray diffraction of (—) undoped, (—) Mg-doped, (—) N-doped and (—) (Mg,N)-codoped Cr_2O_3. The vertical red lines are guidance for the ice.

Figure 5.13 a parameter as a function of crystal size. All the empty symbols are for samples grown using chromium chloride; all the full symbols are for chromium nitrate, squared symbols are for undoped samples, triangular symbols are for only N-doped samples, rhombohedral symbol are for Mg,N-codoped samples.

Figure 5.14 Effect of the pH on the electrical properties of Cr_2O_3:(Mg,N). A steady decline in the resistivity and on the activation energy was observed when the pH was brought to lower values.

Figure 5.15 Effect of the sputtering process on the nitrogen determination by XPS. The $Cr2p^{3/2}$ and the N1s peak were monitored as a function of the sputtering time for an undoped sample. The first row corresponds to the sample as grown, in the second row the sample has been

cleaned for 3 min, in the third row for overall 13 min and in the last row for 23 min. The progressive appearance of a shoulder at 575 eV and of a peak at 397eV (—) is characteristic of a Cr-N bond.

Figure 5.16 Comparison of an undoped (left) and a doped (right) sample. In both case after sputtering a sholder attributed to the Cr-N bonding was present.

Figure 5.17 XRD patterns of the powders for the target preparation after the first thermal cycle for different Mg:Cr ratios: (—)3:97, (—)5:95, (—) 8:92 . The peaks relative to the $MgCr_2O_4$ are indicated with a square.

Figure 5.18 Comparison between two samples grown by using different laser fluency. On the left the sample grown by using a fluency of 1J/cm2 has a rms surface roughness of 8 nm while on the right the sample grown by using a fluency of 0.3 J/cm2 has a surface rms roughness of 5 nm

Figure 5.19 On the left: the out of plane XRD scan of a Cr_2O_3 film grown on sapphire (—). The substrate pattern is given as a reference (—). The symbol ■ indicate a peak coming from the Ag paint used to load the substrate in the PLD deposition holder. On the right: the in plane scan of Cr_2O_3 showing both the substrate and the epilayer reflexes at the same ψ angle: (—) ψ=0, (—) ψ=120 and (—) ψ=240

Figure 5.20 Out of plane XRD patterns of Cr_2O_3:Mg samples (—). A pattern relative to the bare substrate (Al_2O_3) is reported for comparison (—). On the left, the sample with x=0.05 shows only the peaks attributed to the Cr_2O_3 phase. On the right, the sample with x=0.08 show a secondary phase, magnesium dichromate.

Figure 5.21 Mg concentration incorporated in the deposited film with respect to the relative target composition. Determinationhasbeencarried out by XPS measurements.

Figure 5.2 Comparison between the n and k as determined from the point to point calculation (—) with the dispersion as determined from the model (—) for a sample grown by MBE.

Figure 5.3 Comparison between the k values as derived from a fitting procedure which includes (--) the transmission measurements with respect to the same derived from a fitting routine based only on the SE data (—). It is worth noting that the absorption coefficient as determined from

transmission measurements (—) is quite different in comparison to that determined from ellipsometric measurements (—).

Figure 5.24 XRD pattern of (—) under-stoichiometric and (—) stoichiometric Cr_2O_3 grown by MBE. The difference in stoichiometry has only marginal effect on the optical properties (n,k) as determined by spectroscopic ellipsometry

Figure 5.25 On the left. The n, k dispersion as determined for undoped Cr_2O_3 grown by (—) MBE and (—)PLD. On the right, the n and k determined of undoped (—) and Mg doped (0.03, —; 0.05, —) grown by PLD

Figure 5.26 Comparison between the absorption coefficients calculated from transmission measurements for (—) undoped and (—) nitrogen doped Cr_2O_3 grown by spray pyrolysis, transmission measurement for an undoped samples grown by MBE (—)and the absorption coefficient calculated from the extinction coefficient for (—) PLD grown samples. The error bars are representative of the scattering between different samples grown with the same technique.

Figure A.1. Band structure calculation of undoped Cr_2O_3

List of tables

Table 4.1 Effect of different precursors and solvent on the electrical properties of ZnO:Al as deposited (without post-annealing treatments).

Table 4.2 Room temperature electrical properties and growth condition for representative samples used for XPS analysis.

Table 5.1 Figure of merit for several TCOs reported in literature.

Table 5.2 Summary table about the grown samples. The sample types and the sources for the different elements are shown along with the electrical and structural properties.

List of publications

Parts of this work have already previously been published:

[1] Arca, E., K. Fleischer, and I.V. Shvets, *Influence of the Precursors and Chemical Composition of the Solution on the Properties of ZnO Thin Films Grown by Spray Pyrolysis.* J. Phys. Chem. C, 2009. **113**(50), 21074-21081.

[2] Arca, E., K. Fleischer, and I.V. Shvets, *Alternative precursors for the synthesis of SnO_2:F by spray pyrolysis.* Thin Solid Films, 2012. **520**, 1856.

[3] Arca, E., K. Fleischer, and I.V. Shvets, *Magnesium, nitrogen codoped Cr_2O_3: A p-type transparent conducting oxide.* Appl. Phys. Lett., 2011. **99**(11), 111910.

[4] Fleischer, K., E. Arca, and I.V. Shvets, *Improving solar cell efficiency with optically optimised TCO layers.* Sol. Energ. Mat. Sol. Cells, 2012. **101**, 262.

[5] Fleischer, K., Arca, E., Smith, C., and I.V. Shvets, *Aluminium doped $Zn_{1-x}Mg_xO$—A transparent conducting oxide with tunable optical and electrical properties.* Appl. Phys. Lett., 2012. **101**, 121918.

[6] Arca, E., Fleischer, K., and I.V. Shvets, *Tuning the crystallographic, morphologycal, optical and electrical properties of Al:ZnO grown by spray pyrolysis,* submitted to Thin Solid Films

[7] Study of the CuI thin films properties for application as anode buffer layer in organic solar cells. By M. Makha, L. Cattin, S. Dabos-Seignon, E. Arca, N. Stephant, M.Morsli, M. Addou, J.C. Bernède submitted to Apllied Surface Sciences

[8] Arca, E., Fleischer, K., and I.V. Shvets, *Effect of chemical precursors on the optical and electrical properties of spray pyrolysis grown Cr_2O_3:(Mg,N)* (to be submitted to J. Phys. Chem. C)

[9] Arca, E., Fleischer, K., Smith, C., and I.V. Shvets, *A dielectric model of thin film Cr_2O_3 and its dependence on deposition conditions* (in preparation)

Chapter 1

Introduction

1.1. Transparent conducting oxide: an overview

Transparent conducting oxides (TCO) are a particular category of oxides material able to transmit visible light and at the same time able to conduct electricity. Due to their unique features, this class of materials is becoming increasingly important as critical components of a variety of thin film technologies such as smart windows, flat panel displays, solar cells and light emitting diodes (LEDs)[1-10]. This is mainly due to the coexistence of both high transparency to light in the visible region and degenerate conductivity, with values close to those of metals[1]. Tuning of these properties is needed in order to adapt the performance of these materials to the requirements of the technologies in which they have to be implemented[2]. In solar cell modules, TCOs play manifold roles since they can be used as front contacts, back reflectors and intermediate reflectors[11]. They also play a crucial role with respect to the production cost of the module: depending on the composition of the TCO and on the material which the absorbing layer is made of, their cost represents 10 to 30% of the entire cost of the cells. It easy to understand that either improving their performance or reducing their cost can contribute to reducing the overall cost of the photovoltaic device.

Nowadays most of the TCO used are n-type and they are mostly used as passive layer in optoelectronic devices[1,2,12,13]. The most commonly used are indium tin oxide (ITO), fluorinated tin oxide (FTO) and aluminium zinc oxide (AZO)[5,6,8]. The success of these materials lies on the compromise between transparency above 85% in the visible range and conductivity reaching 10^4 S/cm. [2]. Widespread use of ITO has to be limited to the flat panel display technology due to its high cost (the price of indium in 2008 was $685/kg)[2,14]. Indium is a rare element, whose production is connected to that of zinc, as it is extracted as an impurity of the latter[4]. As a result, even an increase in the indium production cannot fulfil the requirement for an up-scaling of the PV-market. Many materials have been recently suggested as

an alternative to ITO[15]. Among the oxides, FTO and AZO have been studied for over 30 years as an alternative for ITO. Although the basic physical properties of transparent conducting oxides are known, there are still a number of questions to be answered. In particular a deep understanding of the fundamental opto-electronic properties of these materials and how they relate to the deposition parameters is still required[3,5,16,17]. A deep understanding of physical and chemical properties of the already existing material will help the design of new material and the design of the deposition route to obtain them[5,17]. In fact, there is a continuous requirement for new materials with optimized properties to fulfil the requirements dictated by the technological progress[1,3,17-19]. Together with high transparency and conductivity, certain specific properties such as work function, surface roughness, thermal and chemical stability, possibility of easily patterning, flexibility, are starting to be required to satisfy the emerging application. Additionally increasing importance is given to green processing and usage of green materials[5,13,20].

n-type TCOs are mostly used for passive application[12]. Device applications have been limited so far by the lack of p-type TCOs. The challenge of getting a p-type TCO was first overcome in 1997 when, for the first time, a p-type transparent conductivity oxide thin film was reported[21]. The interest in these materials is quite high, since their discovery opened up the possibility of using TCOs as active layers in the so-called invisible circuit[22]. This provides the possibility of fabricated devices such as blue or ultra-violet (UV) lights emitting diodesand the possibility of making fully transparent optoelectronics devices (transparent electronics), where the main core of the device is represented by a transparent p-n junction[1,12].Regarding solar cell technology, some of these materials, in particular transition metal oxides such as NiO and Cr_2O_3, have been implemented as hole injecting layers[23-27]. Also for this application, besides good transparency and conductivity, other properties such as morphology and most importantly the work function are essential for the fabrication of good performing devices[28,29]. Fabrication of such devices is currently limited to laboratory scale as either the performances of p-type TCOs reported so far are too poor

for any possible implementation into a commercial device or the growth process is incompatible with the industrial requirements.

From the industrial point of view, TCOs are deposited by spray method, chemical vapour deposition (CVD) methods or sputtering. For these techniques an up-scaling from laboratory to industrial scaling is already a reality. However on a laboratory scale, a number of other techniques are also available. Among those pulsed laser deposition and sol-gel method deserve to be mentioned.

1.2. Outline of this thesis

The final aim of this thesis was the synthesis of new transparent conducting oxide with optimized properties for different applications. TCOs can be implemented in many different devices, each of which will require a fine tuning of particular properties. In this thesis tuning of TCOs properties was done with respect to their implementation in solar cells, although other technologies could benefit from the same material. The physical fundaments of TCOs will be briefly outlined in Chapter 2. Since the ultimate goal was the deposition of new material, a technique able to deliver a high throughput and fast screening of material composition and deposition condition was required. Spray pyrolysis can fulfil these requirements. However the properties of the film deposited are on average lower than those grown by using more sophisticated techniques. In this case, for selected materials, deposition was carried out by means of pulsed laser deposition (PLD). Details of both techniques will be given in Chapter 3. At the beginning it was necessary to understand how the different deposition parameters could be used to fine-tune the optoelectronic properties of the deposited TCO. In order to do that it was necessary to use well known TCOs such as Al:ZnO (AZO) and fluorinated tin oxide (FTO), as, in this way, the experimental results could be compared with the wide literature available for this material. At the same time it was possible to address some of the technological issues related to the implementation of these two materials in the solar cell technology. Focus was addressed to improve the light

transmission inside the solar cell by modifying the dielectric function of the TCO in order to use it as an anti-reflecting coating. Effort was also put on trying to replace toxic chemicals in the production line of FTO. In particular the possibility of using benzenesulfonyl fluorideas fluorine sourcewas explored since, at the time when the study was performed, it was classified as a non-toxic chemical. Details of these studies will be reported in Chapter 4.

Once the limit and the key-aspects of the spray pyrolysis technique were understood, the challenge was then the deposition of new TCOs. The category of p-type conductor was found to be the most attractive. Chromium oxide (Cr_2O_3) was found as a suitable candidate and by means of co-doping with magnesium and nitrogen, a new p-type TCO could be formed (Cr_2O_3:(Mg, N)). It was clear however that spray-pyrolysis was not the best technique to fully explore the potential of this new material due to some intrinsic limit in the technique itself and in the apparatus used. Therefore a more sophisticated technique, PLD, was used to deposit this material. Details of these studies will be described in Chapter 5.

(1) Antonio Facchinetti, T. J. M. *Transparent electronics From synthesis to application*; Wiley, 2010.

(2) Hoel, C. A.; Mason, T. O.; Gaillard, J.-F. o.; Poeppelmeier, K. R. *Chemistry of Materials* **2010**, *22*, 3569-3579.

(3) Ginley, D. S.; Bright, C. *MRS bulletin* **2000**, *25*, 15-18.

(4) Gordon, R. G. *MRS bulletin* **2000**, *25*, 52-57.

(5) D. Ginley, H. H., D.C. Paine *Handbook of transparent conductors*; Springer: New York, 2010.

(6) Fortunato, E.; Ginley, D.; Hideo, H.; C., P. D. *MRS Bulletin* **2007**, *32*, 242-247.

(7) Granqvist, C. G. *Solar Energy Materials and Solar Cells* **2007**, *91*, 1529-1598.

(8) Chopra, K. L.; Major, S.; Pandya, D. K. *Thin Solid Films* **1983**, *102*, 1-46.

(9) Hamberg, I.; Granqvist, C. G. *Journal of Applied Physics***1986**, *60*, R123-R160.

(10) Szyszka, B.; Dewald, W.; Gurram, S. K.; Pflug, A.; Schulz, C.; Siemers, M.; Sittinger, V.; Ulrich, S. *Current Applied Physics* **2012**.

(11) Müller, J. R., Bernd; Springer, J.; Vanecek, M. *Solar Energy* **2004**, *77*, 917-930.

(12) Wager, J. F. *Science* **2003**, *300*, 1245-1246.

(13) Minami, T. *Semiconductor Science and Technology* **2005**, *20*, S35-S44.

(14) Lewis, B. G.; Paine, D. C. *MRS Bulletin* **2000**, *25*, 22-27.

(15) Kumar, A.; Zhou, C. *ACS Nano* **2010**, *4*, 11-14.

(16) Lany, S.; Zunger, A. *Physical Review Letters* **2007**, *98*, 045501.

(17) T.J. Coutts, J. D. P., D.S. Ginley, T.O. Mason In *195th Meeting of the Electrochemical Society* Seattle, Washington, 1999.

(18) A. J. Freeman, K. R. P., T. O. Mason, R. P. H. Chang and T. J. Marks *MRS Bulletin* **2000**, *25*, 45-51.

(19) Ginley, D.; Coutts, T.; Perkins, J.; Young, D.; Li, X.; Parilla, P.; Stauber, R.; Readey, D.; Duncan, C. *MRS symposium proceedings* **2001**, *668*, H2.7.1-H2.7.15.

(20) Szyszka, B.; Loebmann, P.; Georg, A.; May, C.; Elsaesser, C. *Thin Solid Films* **2010**, *518*, 3109-3114.

(21) Kawazoe, H.; Yasukawa, M.; Hyodo, H.; Kurita, M.; Yanagi, H.; Hosono, H. *Nature* **1997**, *389*, 939-942.

(22) Thomas, G. *Nature* **1997**, *389*, 907-908.

(23) Vishal, S.; Gang, L.; Yan, Y.; Chih-Wei, C.; Yang, Y. *Applied Physics Letters* **2006**, *88*, 073508.

(24) Qin, P. L.; Fang, G. J.; He, Q.; Sun, N. H.; Fan, X.; Zheng, Q.; Chen, F.; Wan, J. W.; Zhao, X. Z. *Solar Energy Materials and Solar Cells* **2011**, *95*, 1005-1010.

(25) Fang, G. J.; Qin, P. L.; Sun, N. H.; Fan, X.; Zheng, Q.; Chen, F.; Wan, J. W.; Zhao, X. Z. *Thin Solid Films* **2011**, *519*, 4334-4341.

(26) Yu, W.; Shen, L.; Ruan, S.; Meng, F.; Wang, J.; Zhang, E.; Chen, W. *Solar Energy Materials and Solar Cells* **2012**, *98*, 212-215.

(27) Park, S.-Y.; Kim, H.-R.; Kang, Y.-J.; Kim, D.-H.; Kang, J.-W. *Solar Energy Materials and Solar Cells***2010**, *94*, 2332-2336.

(28) Godoy, A.; Cattin, L.; Toumi, L.; Diaz, F. R.; del Valle, M. A.; Soto, G. M.; Kouskoussa, B.; Morsli, M.; Benchouk, K.; Khelil, A.; Bernede, J. C. *Solar Energy Materials and Solar Cells* **2010**, *94*, 648-654.

(29) Dahou, F. Z.; Cattin, L.; Garnier, J.; Ouerfelli, J.; Morsli, M.; Louarn, G.; Bouteville, A.; Khellil, A.; Bernede, J. C. *Thin Solid Films* **2010**, *518*, 6117-6122.

Chapter 2

Fundamental properties of transparent conductive oxide

2.1. Coexistence of optical transparency and electrical conductivity: the band structures of a TCO

The coexistence of high transparency (>80%) of visible light and resistance as low as few ohms (resistivities in the order of 10^{-4}-$10^{-5}\Omega$cm) is the distinguishing feature of transparent conducting oxides. These two properties are usually considered incompatible as transparent materials are most likely to be insulating and on the other hand, conductive materials such as metals, even in thin layers are quite absorbing. The simultaneous coexistence of these two physical properties can instead be found in some wide band gap semiconductors, in particular oxides, as a result of a defined band structure[1,2].

Transparency is a consequence of the wide band gap as the distance between the top of the valence band and the bottom of the conduction band is higher than 3 eV. For most of the commercially employed TCOs, the top of the valence band is formed primarily by the oxygen *2p* levels while the bottom of the conduction band is formed by highly dispersed *s-like* states of the metal, and in first approximation both bands are parabolic. In many of these oxides, the O_{2p} levels are rather localized; therefore the holes effective mass is quite large and the valence band maximum (VBM) lies quite deep. This determines both a small hole mobility and difficulties in the hole hopping[1,2]. The s-like metal orbitals instead are spatially extended and spherical with good overlaps between neighboring cation[1,3]although it was recently proposed that the oxygen component of the molecular orbital may play an important role in forming the network pathway for the electrons[1,4]. Either way small electron effective mass is obtained for n-type TCO (0.23-0.35m_e, where m_e is the free electron mass)[5]. For most of the TCOs the shape of the bottom of the conduction band and the top of the valence band is approximated to be parabolic. This first order approximation is not always correct and sometimes more complex band structure needs to be

considered[6]. The shape and position of both the valence and conduction band are of primary importance in determining the optical and electrical properties as it will be outlined in the following sections. In perfectly stoichiometric oxide, the Fermi level lies in the middle of the band gap and the system is insulating (Figure 2.1). However native defects (such as non-stoichiometry) or intentional doping can create populated states closer to the bottom of conduction band (donor) or empty states closer to the top of the valence band (acceptor) moving the Fermi level towards the conduction band or towards the valence band respectively. Donors, whose electrons and binding energy can be described and calculated by the *effective mass approximation* are known as shallow, otherwise are known as deep centers.[7] Usually for shallow donors the energy separation (ionization energy) between the donor with respect to the conduction band minimum or the acceptor with respect to the valence band maximum is lower than the thermal energy at room temperature, thus these narrow states are ionized and they create charged carriers. If it is unlikely to be ionized at room temperature, then it is called deep[8]. In the first case an n-type or a p-type transparent conductor is formed.

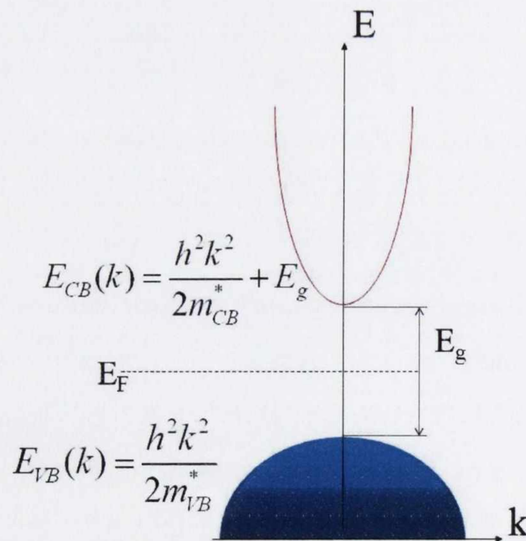

Figure 2.1 An idealized representation of a semiconductor with both top of the valence band and bottom of the conduction band parabolic.

For low doping level the material behaves as a semiconductor and the carrier can be thermally activated up to the saturation region. For

temperatures higher than this, the oxide behaves as an intrinsic semiconductor. In the activation region, information about the ionization energy can be extracted[9] (Figure 2.2)

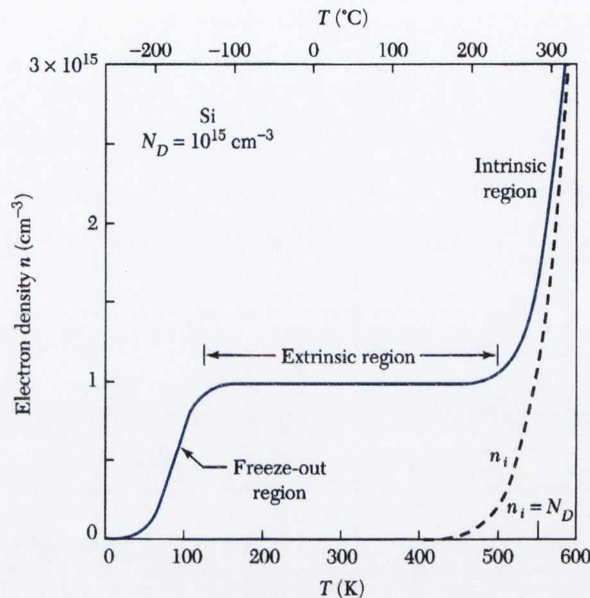

Figure 2.2 The electron density as a function of temperature. 3 different regions are identifiable: the freeze-out region, the extrinsic region and the intrinsic region. Taken from ref.9

An example of doping is schematically shown in Figure 2.3 for the case of In_2O_3. In its perfectly stoichiometric form, this oxide will be insulating, however, different native defects, such as oxygen vacancies (V_o) or the presence of donors, such as tin atoms, can create donor levels close to the bottom of the conduction band. In this case, the Fermi level will lie below the CBM and the material will show a semiconducting behavior, as the carrier will have an activation energy, which in principle, is the energy necessary to promote the electrons from the donor level to the conduction band (ionization energy, 0.03eV for this particular example). As the donor (acceptor) density increases, their states can either merge together (impurity band) or merge with the conduction or valence band[10] (Figure 2.3). In this case, no energy is necessary to promote the carriers and the bottom of the conduction will be populated, thus the material will show a metallic behavior. The donor density at which the donor states merge with the conduction band is defined by the Mott criterion[11](Eq.2.1):

$$n_c^{1/3} \cdot a_0^* \approx 0.25 \qquad 2.1$$

Where the effective Bohr radius a_0^* is given by Eq. 2.2:

$$a_0^* = \frac{h^2 \varepsilon_0 \varepsilon^m}{\pi e^2 m_c^*} \qquad 2.2$$

Where ε_0 is the permittivity of the free space, ε^m is the dielectric constant of the host lattice, m_c^* is the effective mass of the carriers. Once the critical density of impurity is reached, free electron behavior is expected for the conduction electrons and the material is said to be degenerate.

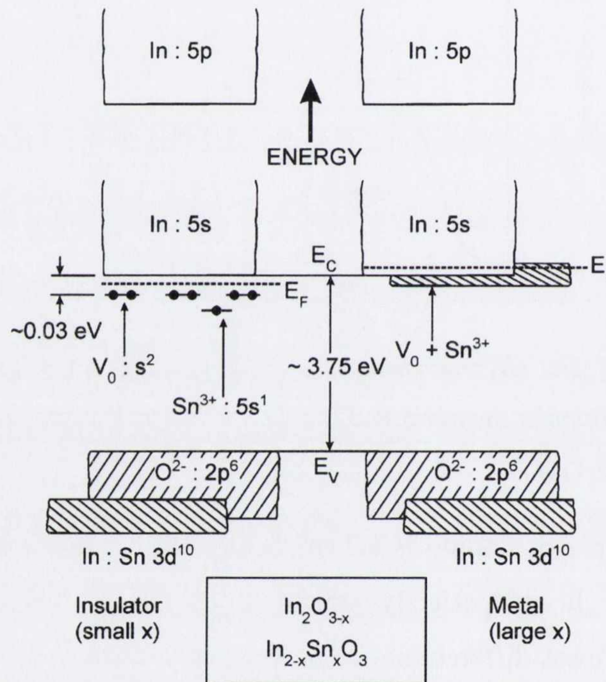

Figure 2.3 A schematic representation of impurity doping for the case of Indium Tin Oxide (ITO). Taken from ref. 10

The criterion to define a system to be degenerate is quite arbitrary since there is a smooth transition between non-degeneracy and degeneracy. Such transition is a simultaneous function of the material characteristics (the Bohr radius of the electron at the impurity center varies depending on the properties of the host oxide), number of impurities center and temperature. It is commonly accepted to define as degenerate, a system which needs to be treated by using the Fermi-Dirac distribution and which cannot be approximated by the Boltzmann distribution. At the same time when the Boltzmann distribution is a good approximation for describing the

properties of the system, in particular the electrical properties, the system is considered not degenerate.

Degeneracy has 2 main consequences on the optical properties, that's to say the "band gap opening" due to Burstein Moss effect and the appearance of a Drude-like tail in the infrared part of the spectra. Details of these two processes will be given in section 2.3. It has also important consequences on the electrical properties, with the thermal activation energy for the carriers reduced to zero. This is only the first example which proves the intimate interconnection between optical and electrical properties in TCOs. A careful investigation of both is thus required in order to assess the quality of a material as a TCO.

2.2. Electrical properties.

The easiest method to evaluate the electrical properties of an oxide is by simply determining its resistance via Ohm's law (Eq. 2.3):

$$V = IR \qquad 2.3$$

Usually, for thin films, the sheet resistance is measured, which is defined as in Eq. 2.4

$$R_{SH} = \frac{V}{I} CF \quad (\Omega/\square) \qquad 2.4$$

Where CF is a correction factor which depends on the geometry of the four point probe used for the measurements[9].

The sheet resistance is dependent on the film thickness, so in order to compare different material it is more convenient to use the resistivity or the conductivity values, which depend only on the material properties, namely the carrier concentration and the mobility. (Eq.2.5)

$$\sigma = 1/\rho = e(n_e \mu_e + n_h \mu_h) \qquad 2.5$$

where σ is the conductivity, ρ the resistivity, μ the drift mobility, n the carrier concentration, e the electron charge, the subscript e stands for electrons while the h stands for holes. If the number of electrons is considerably higher than the number of holes ($n_e >> n_h$) as in n-type

semiconductors, the conductivity is determined by the majority carriers (Eq. 2.6).

$$\sigma = 1/\rho \approx e(n_e \mu_e) \qquad 2.6$$

The drift mobility μ is defined as the *proportionality constant* between the drift velocity (v_d) of the carriers under an applied electric field and the strength of the electric field itself (E) (Eq.2.7).

$$\vec{v}_d = -\mu_e \vec{E} \qquad 2.7$$

However the conductivity is not a linear function of the carrier concentration as the mobility itself varies with the carrier concentrations as well as they both depend on temperature[12,13].

The dependence of the conductivity with temperature is a precious information in order to study the properties of a material. As introduced earlier, degenerate semiconductors show no activation energy, and quite often, a metallic behavior, in other words the conductivity decreases as the temperature increases. Non-degenerate semiconductors show an activated conductivity, with a dependence of the form reported in Eq. 2.8:

$$\sigma = \sigma_0 \exp -(T_0 / T)^n \qquad 2.8$$

The exponent n will vary depending on the type of conductivity. When n=1/4, the conductivity is known as variable range hopping and the carrier motion is considered to be a mix of thermally activated hopping and carrier tunneling from site to site. When strong interaction of the carriers with the lattice causes local distortions, the effective inertia of the carriers is increased and the mechanism is known as polaron conductivity[1,14].

When n=1, the semiconductor exhibit band conductivity, which, for perfect crystal, gives information about the activation energy of a carrier to be excited from a defect to the band. In this classical band conduction the number of carrier varies exponentially with temperature, while the carrier mobility is less sensitive to the temperature[1]. The latter is however very important as its dependence on temperature gives information about the scattering mechanism which limits the carriers drift. To keep the discussion as simple as possible, the case of an n-type conductor will be presented. A similar discussion can be obtained for holes taking into consideration the valence band features.

The drift mobility is dependent on the effective mass of the carrier and on the scattering mechanism via the relaxation time (Eq. 2.9).

$$\mu = \frac{e\tau}{m*} = \frac{e\lambda_{mfp}}{m^* v_d} \qquad 2.9$$

where $m*$is the effective mass of the carrier, τ is the relaxation time (the time that on average, elapses between two successive scattering events), λ_{mfp} is the mean free path (the distance that a carrier travels on avarage between two successive collisions). The effective mass of the carrier is directly linked to the band structure of the material since it is proportional to the curvature of the bottom of the conduction band. (Eq. 2.10)

$$\frac{1}{m*} = \frac{1}{\hbar^2} \cdot \frac{\partial^2 E(k)}{\partial k^2} \qquad 2.10$$

The scattering time and thus the mean free path are determined by all the interaction that charge carriers suffer with their surroundings, such as phonons, ionized impurities, neutral impurities, crystal defects, grain boundaries, which will tend to limit the mobility (scattering mechanisms). All these mechanisms will tend to limit the mobility of the carriers, thus the resulting mobility can be calculated according to the Matthiessen rule (Eq. 2.11)

$$\frac{1}{\mu} = \Sigma \frac{1}{\mu_i} \qquad 2.11$$

Each of these mechanisms will have a peculiar dependence on the carrier concentration and temperature[13,15]. Therefore the extent of each contribution to the total mobility can be considerably different and might be confined to a specific temperature region. For example, in a heavily doped semiconductor the contribution of neutral impurities can be neglected taking into consideration that even at rather low temperature (77K) their concentration is quite low as most of impurities are fully ionized[15,16]. For this reason, it is a common practice to talk about the principle scattering mechanism referring to that particular process which influences the conductivity the most.

The remaining scattering mechanisms can be divided into two categories depending on whether they are intrinsicor not. Intrinsic

mechanisms are unavoidable and thus they set the lower limit of the resistivity reachable[12,17]. Scattering at ionized impurities or by phonons are intrinsic mechanisms[17,18]. Grain boundaries as well as structural disorder are not intrinsic and in principle they can be eliminated by improving the crystal quality[18].

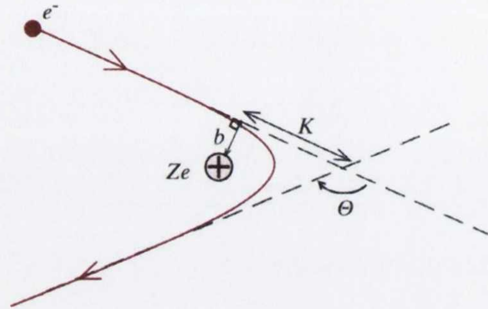

Figure 2.4 Schematic view of the Coulomb scattering process of an electron by means of a positively charged ion. The scattering cross-section is a function of the parameters b, K and Θ. Taken from reference 7

Scattering by ionized impurities is a consequence of the Coulomb interaction between the charged center and the free electrons (Figure 2.4). This problem was treated classically by Conwell, (Conwell-Weisskopf approach) and quantum-mechanically by Brooks and Dingle[7,19-21]. The two models resemble each other except that for very high carrier concentration, and in both cases the mobility depends on temperature as $\mu \propto T^{3/2}$ [7]. For degenerate semiconductors, instead, mobility is independent of temperature and it can be calculated according to Eq.2.12[22].

$$\mu_{IID} = \frac{24\pi^3\hbar^3(\varepsilon_0\varepsilon)^2 N}{Z^2 e^3 f(x) N_i m^{*2}} \qquad 2.12$$

Where $m^*$is the reduced mass, ε the absolute dielectric permittivity, N_i the density of scattering centers and f(x) the screening function (Eq.2.13 and 2.14):

$$f(x) = \ln\left(1+\frac{4}{x}\right) - \left(1+\frac{4}{x}\right) \quad 2.13$$

$$x = \frac{4e^2 m^*}{(3\pi^5)^{1/3}\hbar^2 (4\pi\varepsilon_0\varepsilon) N^{1/3}} \quad 2.14$$

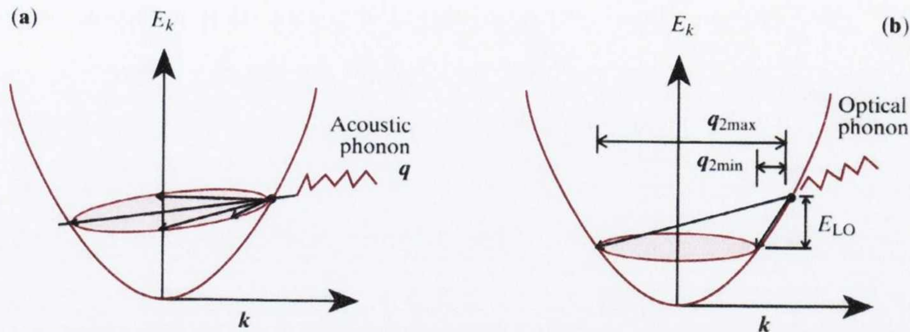

Figure 2.5. Schematic view of the scattering process of an electron by means of (a) an acoustic phonon, (b) an optical phonon. Taken from ref. 7

Phonons represent the second intrinsic scattering mechanism in semiconductors (Figure 2.5). Optical phonons are energetic modes therefore their contribution to scattering of electrons at room temperature can be neglected. Scattering due to acoustic phonons will be characterized by a dependence of carriers' mobility on temperature as $AT^{-3/2}$ according to the Eq. 2.15 and 2.16[22]:

$$\mu_L = \frac{(8\pi)^{1/2} e\hbar^4 C_{ii}}{3E_I^2 (m^*)^{5/2} (kT)^{3/2}} \quad 2.15$$

$$E_I = V\left(\frac{dT}{dV}\right)\left(\frac{dE_g}{dT}\right) \quad 2.16$$

Determining the mobility value by using this formula is possible provided that the value of the elastic constant for longitudinal waves C_{ii} and for the volume expansion coefficient $\left(\frac{1}{V}\frac{dV}{dT}\right)$ are known[22].

In polycrystalline materials, the flow of electrons will imply that the latter needs to pass from one grain to another. In this process, a barrier can be represented by the grain boundaries, complex structures composed of highly disordered atoms, which separate adjacent crystalline grains. If the barrier is present, one electron can tunnel through or be thermionically emitted[23]. There are two theories to describe the nature of grain boundaries: in the first the grain boundaries represent an impurity segregation "sink",

with a concentration of impurity atoms much higher than inside the grain.[23,24] The second suggests that the unordered structure in the grain boundaries creates defects and dangling bonds, able to act as traps and thus limiting the number of free carriers. After trapping, the traps themselves become charged, thus creating a potential barrier that prevents the current flow (reduction of the mobility).[23,24] Grain boundaries are of considerably importance for polycrystalline material and their effect becomes more severe as the grain size approaches the value of the mean free path of an electron. Mobility limitation due to grain boundaries can be determined according to Eq. 2.17.

$$\mu_{GB} = le\left(\frac{1}{2\pi m^* kT}\right)^{1/2} \exp\left(\frac{-E_a}{kT}\right) \qquad 2.17$$

Where E_a is the activation energy and l is the grain size.

All the equations (2.12-2.17) yield to values of mobility express in $cm^2V^{-1}s^{-1}$.

The highest mobility achievable is determined by the summation over all scattering mechanisms, as it was calculated in Dekkers PhD thesis (Figure 2.6)

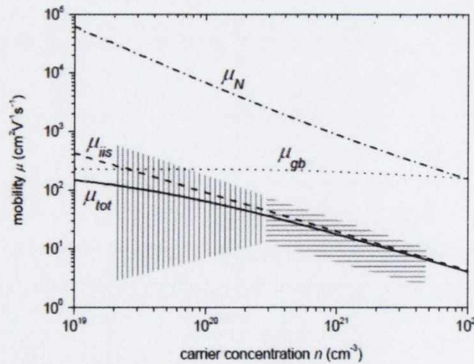

Figure 2.6 Dependence of the mobility values upon the carrier concentration for different scattering mechanism: μ_N, μ_{gb}, μ_{iis} represents respectively the mobility dependence if the scattering mechanism is due to neutral impurities, grain boundaries or ionized impurities. μ_{tot} represents the upper value of mobility achievable if all of the above are taken into account

Resistivity measurements only give the product of the mobility and the carrier concentration. In order to estimate both values, it is common practice to measure the Hall Effect.

2.2.1. *Hall effect.*

Hall Effect measurements allow to obtain information not only about the carrier concentration and the mobility of the carrier but also about the type of carrier (h or n) responsible for the conductivity[25]. Two different configurations can be adapted for the measurement: Hall bar or Van der Paw geometry.

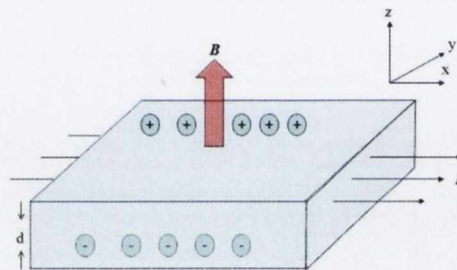

Figure 2.7 A schematic representation of the Hall bar.

Taking into consideration the scheme in Figure 2.7, an electric field is applied along the x direction and as a consequence a constant current *I* is set it up in this direction. While an electron is moving along the applied electric field, it will also experience the force of a magnetic field applied perpendicular to the electric field. As a result, the electron will be deflected in the direction normal to both the electric and magnetic field by the Lorentz force (Eq. 2.18).

$$\vec{F} = -e(\vec{E} + \vec{v} \times \vec{B}) \qquad 2.18$$

Thus the electrons will drift towards the negative y axis of the sample, building up a negative voltage. This latter represents the Hall Voltage, V_H Eq.2.19).

$$V_H = \frac{IB}{end} \tag{2.19}$$

Where I is the current, B the magnetic flux. If the sheet resistance is known, then it is possible to calculate the Hall mobility (μ_H) (Eq. 2.20):

$$\mu_H = \frac{|V_H|}{R_{SH}\, I\, B} \tag{2.20}$$

It is worth noting that drift mobility and Hall mobility are related to each other via the Hall factor r_H, whose magnitude depends on the scattering mechanisms that contribute to τ and is usually close to 1 (Eq. 2.21 and 2.22)

$$\mu_H = r_H \mu \tag{2.21}$$

$$r_H = \frac{\langle \tau^2 \rangle}{\langle \tau \rangle^2} \tag{2.22}$$

The Hall mobility can be directly calculated from measurable quantities in the Van der Paw configuration, namely the sheet and the Hall resistance, without prior knowledge of the thickness of the conductive layer. Determination of the carrier concentration and resistivity, instead, requires independent estimation of the film thickness.

2.3. Optical properties and their correlation with the electrical properties.

One of the prominent features of a TCO is its transparency window which covers most of the visible spectra range. The amount of light transmitted will be limited by two main effects: reflection and absorption. It follows that the portion of light that can be transmitted through a medium (T) depends on the reflectivity (R) and the absorbance (A) of the medium itself.

In general terms, a light beam incident on an optical medium will be partially reflected at the front and at the back surface of the films. If the optical medium is represented by a thin film, the thickness *d* can be

comparable with the wavelength of light. In this condition and provided that the absorption of light is negligible, the light is reflected at the front and back surface in a coherent way. This gives rise to an interference pattern (Fabry-Perrot oscillations), whose spacing (*ΔE*) is related to the refractive index (*n*) of the layer and its thickness (*d*) (Eq2.23).

$$\frac{ch}{2n\Delta E} = d \qquad 2.23$$

Where *c* is the speed of light in vacuum and *h* the Plank constant.

For a strongly absorbing medium, multiple reflections will be negligible. In this case, during the propagation, that portion of light which is resonant with the transition frequency of the atoms in the medium will be absorbed[26]. Because of the absorbing process, the light intensity passing through a medium will be attenuated with distance (Eq. 2.24)

$$dI = -\alpha\, \partial z \times I(z) \qquad 2.24$$

where z is the direction of propagation

The solution of the above equation gives an exponential decay of light intensity (Beer's law, Eq. 2.25)

$$\frac{I}{I_0} = e^{-\alpha d} \qquad 2.25$$

Where α is the absorption coefficient which is defined as the fraction of power absorbed in a unit length of medium, and is related to the transmittance (T) and the reflectance (R) according to Eq. 2.26[26].

$$T = (1-R)^2 e^{-\alpha d} \qquad 2.26$$

It is quite common to quantify the absorption of an optical medium in terms of its optical density or absorbance, which is defined as in Eq. 2.27 [26]:

$$A = -\log_{10}\left(\frac{I}{I_0}\right) = \frac{\alpha d}{\log_e(10)} = 0.434\alpha d \qquad 2.27$$

All the information about the fundamental optical properties of a material (absorption coefficient, transmittance and reflectance) can be extracted from its complex refractive index (ñ) (Eq. 2.28)

$$\tilde{n} = n + ik \qquad 2.28$$

The real part of the refractive index is defined as the ratio of the propagation velocity of light in free space (c) to the velocity of light in the medium (v) (Eq. 2.29)

$$n = \frac{c}{v} \qquad 2.29$$

The imaginary part (extinction coefficient, k) is directly connected to the absorption coefficient of the material (Eq. 2.30) [27].

$$\alpha = \frac{4\pi k}{\lambda} \qquad 2.30$$

The reflectivity depends on both n and k as in Eq.2.31.

$$R = \left|\frac{\tilde{n} - 1}{\tilde{n} + 1}\right|^2 = \frac{(n-1)^2 + k^2}{(n+1)^2 + k^2} \qquad 2.31$$

The complex refractive index can be related to its complex dielectric constant (Eq. 2.32-2.35).

$$\tilde{\varepsilon}_r = \varepsilon_1 + i\varepsilon_2 \qquad 2.32$$

$$\tilde{n}^2 = \tilde{\varepsilon}_r \qquad 2.33$$

$$\varepsilon_1 = n^2 - k^2 \qquad 2.34$$

$$\varepsilon_2 = 2nk \qquad 2.35$$

Away from strong absorption edges, the absorption coefficient (k) vanishes and the refractive index becomes a constant number (Eq. 2.36)

$$n = \sqrt{\varepsilon_\infty} \qquad 2.36$$

where ε_∞ is the high frequency dielectric constant[27].

In semiconductors the absorption coefficient is a strong function of the photon energy andfor parabolic band structure it can be used to determine the optical band gap (Eq. 2.37) [26].

$$\alpha(\hbar\omega) \propto (\hbar\omega - E_g)^\gamma \qquad 2.37$$

Where hν is the photon energy and γ is a constant, whose value depends on the type of transition. Indeed, band to band transition can be classified as allowed or forbidden, depending on if a transition respects the selection rules or not. Allowed transitions respect both the energy conservation and momentum conservation rules and they can be further

classified into direct or indirect[26]. Direct transitions occur between a maximum and a valley position at the same k point. In this case the γ coefficient is equal to ½. Indirect transitions occur when the valley is displaced in the k space, and therefore the interaction with a phonon (which is absorbed or emitted) is necessary to conserve the momentum (Figure 2.8).

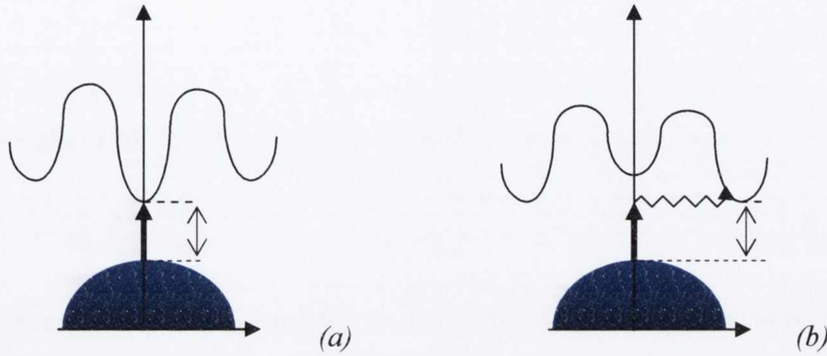

Figure 2.8 Schematic representations of (a) direct and (b) indirect band gap semiconductor

It follows that the absorption coefficient is modified as in Eq. 2.38[26].

$$\alpha(\hbar\omega)^{ind} \propto (\hbar\omega - E_g \pm \hbar q)^2 \qquad 2.38$$

Where q is the phonon wave vector and the ± sign depends on whether a phonon is absorbed or emitted.

In the case of perfectly parabolic band structure, for non-degenerate semiconductor, band gap represent the first optical transition. However, when degeneracy takes place, the first allowed optical transition is higher than the fundamental gap, according to the Burstein-Moss effect (Figure 2.9). The magnitude of the shift (Δ_{BM}) is usually calculated according to the free-electron theory, according to Eq. 2.39.

$$\Delta_{BM} = \frac{\hbar^2}{2m^*}(2\pi^2 n_e)^{2/3} \qquad 2.39$$

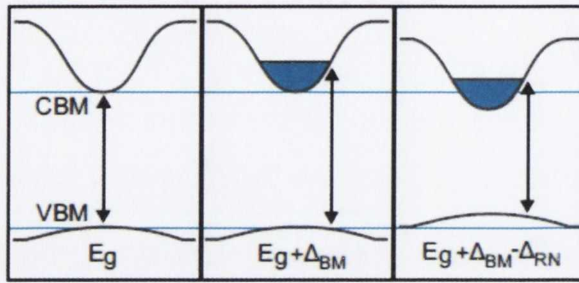

Figure 2.9 Consequence of degeneracy on the optical properties of semiconductors: the fundamental band gap Eg is open up due to the Burstein-Moss shift. However due to the renormalization effect, the widening is reduced. Taken from ref. 28

However the experimental values for the band-gap opening are usually much less than what expected from those predicted by the free-electron model. In order to account for this discrepancy, a re-normalization effect has been proposed. The origin of this latter has been attributed to many-body effects including electron-exchange interactions, minority carrier correlation and carrier-ion correlation, in order to account the shrinkage of the band gap (Δ_{RN}) as balancing to its opening (Figure 2.9), thus estimating the band gap for a degenerate semiconductor as in Eq.2.40[28-31].

$$E_g^{DEG} = E_g + \Delta_{BM} - \Delta_{RN} \qquad 2.40$$

The second consequence of degeneracy on the optical properties is the set on of intra-band transition (Drude-like tail). The Drude frequency (ω_p) depends upon carrier concentration N (which can correspond to either n_e or n_h depending if n-type or p-type) (Eq. 2.41)

$$\omega_p^2 = \frac{N q^2}{\varepsilon_\infty \varepsilon_0 \, m^*} \qquad 2.41$$

Therefore as the carrier concentration increases, the Drude tail will be pushed towards shorter wavelength (Figure 2.10).

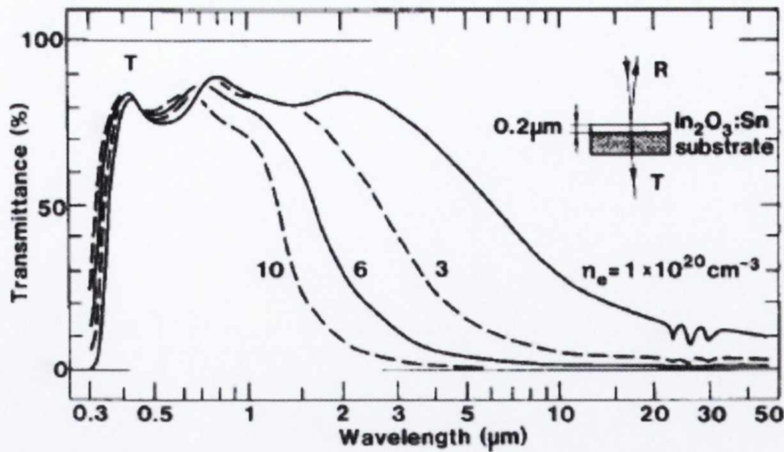

Figure 2.10 Effect of the carrier concentration on the Drude tail position. Taken from ref. 32

It follows that the window of transparency is limited from the fundamental band gap in the UV-part of the spectra from the Drude tail in the infrared. In order to guarantee a good transparent window to the visible light, it is necessary to have band gap higher than 3 eV (λ~400 nm) and plasma tail below 1.55 eV (λ~800 nm)[27,32,33]. This implies that, for example for indium tin oxide, the carrier concentration should be lower than $2.6 \cdot 10^{21} cm^{-3}$ [10]. This is the reason why, in particular for solar cell application, it is preferable to increase the conductivity by increasing the mobility of the carrier rather than increasing the carrier density[34].

Morphology can contribute to macroscopic optical properties of the material. In case of highly rough surface, the specular transmission of the sample can be quite low with respect to that expected according to the complex refractive index for that material (Figure 2.11).

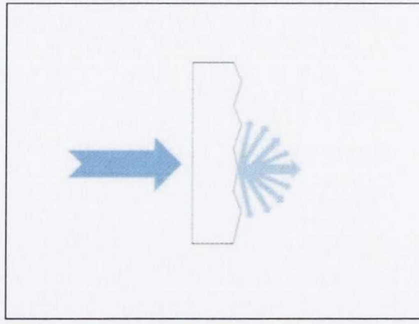

Figure 2.11Effect of the morphology on the optical properties of the material. Surface roughness attenuates the intensity of the light in the forward direction as part of the light gets scattered in all direction.

The reason for this is that light gets scattered at a rough surface and its intensity along the z direction gets attenuated in an analogous ways to absorption[26] (Eq. 2.42)

$$I = I_0 \exp(-N_{SC}\sigma_{SC}d) \quad 2.42$$

Where N_{SC} is the number of the scattering centers per unit volume and σ_{SC} is the scattering cross-section. From an experimental point of view, it is possible to distinguish between the two cases, scattering or absorption, only by employing specialized equipment (spheres detector) which allows evaluating the contribution from diffuse and absorbed light. In fact the total transmission and the total reflection, i.e. the light transmitted and the light reflected over the inter sphere, is the same as expected according to the refractive index of the material. Scattering at rough interfaces is not always a detrimental property. On the contrary, in particular applications this is a desired effect. For example this effect is used for photon management in solar cell. In particular surface texturized TCO front contact is useful in order to enhance the path length in of light in poorly absorbing materials (such as amorphous silicon thin film cells)[35-40].

Two parameters are used to describe the scattered light: the angular distribution function (*ADF*) which describe how the intensity of the diffuse light varies at different angles and the haze parameter (H), this latter being defined as the ratio between the diffuse transmitted light T_{dif} and the total transmitted light T_{tot} (diffuse + specular transmitted light)[35,38,40] (Eq.2.43)

$$H_T(\lambda) = \frac{T_{dif}(\lambda)}{T_{tot}(\lambda)} \qquad 2.43$$

In order to estimate the haze, the diffuse light is measured by trapping the specular transmitted beam, so that a sphere detector will measure only the scattered intensity. For total transmittance, instead, both specular and diffuse components are capture by the sphere detector. Therefore, the haze parameter is thus an estimation of the capability of a sample to scatter the light at a given wavelength.

2.4. Concluding remarks

It is clear that optical and electrical properties are strongly interrelated in a transparent conducting oxide and both should be at their possible best. It follows that comparison between different material cannot be done by taking into consideration only one or the other, but it is necessary to account for both of them simultaneously. Moreover, in order to fully assess the properties of a material it is important that the evaluation is independent of the film thickness.

For this reason it is a common practice to define the figure of merit, F, a quantity that takes into account the optical and electrical properties of a material despite of the thickness. There several ways to define the Figure of merit, but the one which looked most appropriate and therefore it is widely used in the present thesis is reported in Eq. 2.44[33,41].

$$F = -\left[\frac{1}{R_{sh}\ln(T+R)}\right] \approx -\left[\frac{1}{R_{sh}\ln(T)}\right] \qquad 2.44$$

The tools to measure the reflectance became available only in a later stage of the present studies, therefore an approximated value for the figure of merit which takes into account only the transmission was used extensively.

(1) Antonio Facchinetti, T. J. M. *Transparent electronics From synthesis to application*; Wiley, 2010.

(2) Hosono, H.; Kamiya, T.; Hirano, M. *Bulletin of the Chemical Society of Japan* **2006**, *79*, 1-24.

(3) Hosono, H.; Kikuchi, N.; Ueda, N.; Kawazoe, H. *Journal of Non-Crystalline Solids* **1996**, *198*, 165-169.

(4) Medvedeva, J. E.; Hettiarachchi, C. L. *Physical Review B*, **2010,** *81*, 125116.

(5) Toshio Kamiya, M. K. *MRS Bulletin* **2008**, *33*, 1061-1066.

(6) Pisarkiewicz, T.; Zakrzewska, K.; Leja, E. *Thin Solid Films* **1989**, *174, Part 1*, 217-223.

(7) Cardona, P. Y. Y. M. *Funamental of Semiconductors Physics and material properties*; Springer, 1999.

(8) Anderson, J.; Chris, G. V. d. W. *Reports on Progress in Physics* **2009**, *72*, 126501.

(9) Sze, S. M. *Semiconductor Devices Physics and Technology*; John Wiley & son, 2002.

(10) Edwards, P. P.; Porch, A.; Jones, M. O.; Morgan, D. V.; Perks, R. M. *Dalton Transactions* **2004**, 2995-3002.

(11) Mott, N. F. *Philosophical Magazine* **1961**, *6*, 287-309.

(12) Chen, M.; Pei, Z. L.; Wang, X.; Yu, Y. H.; Liu, X. H.; Sun, C.; Wen, L. S. *Journal of Physics D: Applied Physics* **2000**, *33*, 2538-2548.

(13) Ellmer, K.; Mientus, R. *Thin Solid Films* **2008**, *516*, 5829-5835.

(14) Ingram, B. J.; Bertoni, M. I.; Poeppelmeier, K. R.; Mason, T. O. *Thin Solid Films* **2005**, *486*, 86-93.

(15) Ellmer, K.; Mientus, R. *Thin Solid Films* **2008**, *516*, 4620-4627.

(16) Thangaraju, B. *Thin Solid Films* **2002**, *402*, 71-78.

(17) Bellingham, J. R.; Phillips, W. A.; Adkins, C. J. *Journal of Materials Science Letters* **1992**, *11*, 263-265.

(18) Coutts, T. J.; Young, D. L.; Li, X. *MRS Proceedings* **2000**, *623*, 199-209.

(19) Conwell, E.; Weisskopf, V. F. *Physical Review* **1950**, *77*, 388-390.

(20) Dingle, R. B. *Philosophical Magazine* **1955**, *46*, 831-840.

(21) Brooks, H. *Physical Review* **1951**, *83*, 879.

(22) Ramaiah, K. S.; Raja, V. S. *Applied Surface Science* **2006**, *253*, 1451-1458.

(23) D. Ginley, H. H., D.C. Paine *Handbook of transparent conductors*; Springer: New York, 2010.

(24) Seto, J. Y. W. *Journal of Applied Physics* **1975**, *46*, 5247-5254.

(25) Putley, E. H. *The Hall effect and related phenomena*; Butterworths: London, 1960.

(26) Fox, M. *Optical properties of solids*; Oxford Univeristy Press: Oxford, 2010.

(27) Coutts, T. J.; Young, D. L.; Li, X. *MRS bulletin* **2000**, *25*, 58-65.

(28) Walsh, A.; Da Silva, J. L. F.; Wei, S.-H. *Physical Review B* **2008**, *78*, 075211.

(29) Lu, J. G.; Fujita, S.; Kawaharamura, T.; Nishinaka, H.; Kamada, Y.; Ohshima, T.; Ye, Z. Z.; Zeng, Y. J.; Zhang, Y. Z.; Zhu, L. P.; He, H. P.; Zhao, B. H. *Journal of Applied Physics* **2007**, *101*, 083705-7.

(30) Sans, J. A.; Sanchez-Royo, J. F.; Segura, A.; Tobias, G.; Canadell, E. *Physical Review B* **2009**, *79*, 195105.

(31) Sernelius, B. E.; Berggren, K. F.; Jin, Z. C.; Hamberg, I.; Granqvist, C. G. *Physical Review B* **1988**, *37*, 10244-10248.

(32) Granqvist, C. G. *Solar Energy Materials and Solar Cells* **2007**, *91*, 1529-1598.

(33) Exarhos, G. J.; Zhou, X.-D. *Thin Solid Films* **2007**, *515*, 7025-7052.

(34) Haug, F.-J.; Biron, R.; Kratzer, G.; Leresche, F.; Besuchet, J.; Ballif, C.; Dissel, M.; Kretschmer, S.; Soppe, W.; Lippens, P.; Leitner, K. *Progress in Photovoltaics: Research and Applications* **2011**, *20*, 727-734.

(35) Campa, A.; Krc, J.; Malmstrom, J.; Edoff, M.; Smole, F.; Topic, M. *Thin Solid Films* **2007**, *515*, 5968-5972.

(36) Jäger, K.; Isabella, O.; Zhao, L.; Zeman, M. *physica status solidi (c)* **2010**, *7*, 945-948.

(37) Krc, J.; Brecl, K.; Smole, F.; Topic, M. *Solar Energy Materials and Solar Cells* **2006**, *90*, 3339-3344.

(38) Krc, J.; Zeman, M.; Smole, F.; Topic, M. *Journal of Applied Physics* **2002**, *92*, 749-755.

(39) Krc, J.; Zeman, M.; Smole, F.; Topic, M. *Thin Solid Films* **2004**, *451-452*, 298-302.

(40) Ruske, F.; Jacobs, C.; Sittinger, V.; Szyszka, B.; Werner, W. *Thin Solid Films* **2007**, *515*, 8695-8698.

(41) Gordon, R. G. *MRS bulletin* **2000**, *25*, 52-57.

Chapter 3

Experimental apparatus

3.1. Introduction

Transparent conducting oxide are nowadays a commercial reality, produced in large quantities mainly by chemical vapour deposition (CVD), sputtering or spray pyrolysis. These techniques are also used on a laboratory scale, along with others techniques, such as pulsed laser deposition (PLD) or atomic layer deposition (ALD), less suited for a large scale application. In this thesis, two different techniques were adopted: spray pyrolysis and pulsed laser deposition. Details of both of them will be given in the following paragraphs.

In addressing the effect of deposition conditions and in assessing the properties of the deposited layer, it was necessary to widely characterised the materials. Characterization of electrical, optical, morphological, compositional and structural properties was carried out by using a variety of technologies, whose main feature will be outline in the following sections.

3.2. Deposition methods

For this work both a chemical and a physical deposition method were used. Both techniques present advantages and disadvantages, which will be discussed in details in the following section. The overall idea behind this choice was that spray pyrolysis allows rapid throughput of material and high flexibility in changing material composition and deposition conditions, thus being suitable for rapid screening of materials and material composition. However this flexibility implies a compromise in regards to the quality of the material produce. Therefore, once a particular material was identified, production of high quality layers was possible by using pulse laser deposition.

3.2.1. Spray pyrolysis

Spray pyrolysis is a chemical deposition technique, used industrially for large scale application. It is a vacuum-free, cheap and fast deposition method, quite versatile, with the drawback of producing polycrystalline films, which often suffer from poor crystallographic and morphological properties in comparison with those deposited by more sophisticated methods such as ALD, CVD, sputtering or PLD.

The spray-pyrolytic process consists of nebulizing a solution, containing the precursor salts, and its transport towards a hot substrate by means of a gas stream.[1-3] Within the hot zone above the substrate, the precursors undergo a pyrolytic decomposition, i.e. a thermal decomposition in the presence of oxygen[4]. As a consequence a thin layer of metal oxide is deposited onto the substrate. Key parameters of this process are: the atomization technique, aerosol transport (carrier gas, pressure, distance and reactor geometry), substrate temperature and material, and the chemical composition of the solution[1,5]. The set-up used in the present thesis is reported in Figure 3.1 together with the process scheme.

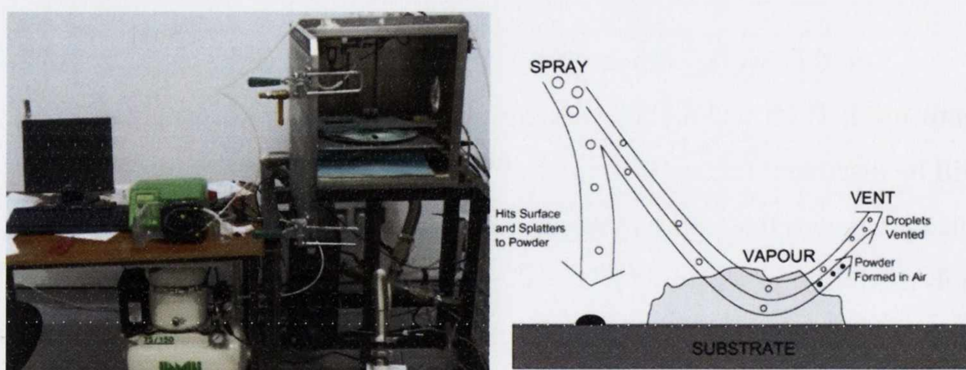

Figure 3.1 On the left: the spray-pyrolysis deposition apparatus; on the right the schematic representation of the pyrolysis process. The effect of the droplet size distribution is highlight. Taken from ref. 1.

Regarding the atomization process, many efforts have been devoted to optimize it, and as a result, different types of nozzles are commercially available nowadays.[6-8] The crucial point is to get a homogeneous droplet size distribution as well as a small value for the mean particle size since

better film quality is achievable in this case[1,9]. The reason for this is that, for small particle size, the solvent fully evaporates during the transport towards the substrate leading to a vapour-solid reaction for the precursors. If the particle size is too big with respect to the nozzle-substrate distance, the solvent does not have enough time to evaporate and droplets of liquid impinge upon the surface followed by a liquid-solid reaction. On the other end, if the solvent is too volatile or if very fine small droplets are created, those evaporate fully before they reach the surface and powders are formed and conglobated into the film. Thus small droplets size and homogenous size distribution are preferable. The distance between the nozzle and the substrate can be adjusted accordingly to fine tuning the discussed balance.

The carrier gas determines the oxidizing potency of the atmosphere in which the pyrolytic reaction takes place, hence influencing the cation oxidation number in the final product and allows fine-tuning of the native defects in the film (oxygen vacancies or excess oxygen)[5,10]. Moreover, pressure in the nozzle determines the rate at which the droplets reach the surface, thus influencing both the growth rate and the cooling rate of the surface. In the case of the blast nozzle, the pressure and gas type also determines the droplet size distribution. Hence it has a more direct influence in the final film properties.

The temperature of the substrate influences many different process parameters: aerosol transport towards the substrate, solvent evaporation, possibility of droplets impacting the surface, the dynamics of their spreading and, most importantly, the precursor decomposition pathway[1,11]. Therefore, the surface temperature plays a major role in defining morphology and composition of the deposited film. In fact, by varying the temperature it is possible to change from regimes in which the precursor salts do not decompose to regimes associated with different oxidizing states possible for the precursor[12]. The importance of the substrate material is mainly related to its heat capacity. Materials with a low heat capacity and conductivity are cooled much faster by the spray than those that have large onesdetermining the effective growth temperatures[13,14]. Glass slides (Fisher brand, thickness 0.8-1mm) are commonly used as substrate but in order to reduce the thermal gradient, coverslips (Roth, thickness 0.17 mm) were used for the deposition

of p-type TCOs. Although some reports deal with the effect of the chemical precursors on the properties of the deposited films[15-17], this topic has been discussed to a lesser extent.

Only few general guidelines have been established. In particular it is known thatsolvents with lower density and surface tension (such as thealcohol-based ones) enable creating droplets of smaller size. Moreover solvents with lower boiling point vaporize easily, and this can have a major consequence for achieving real pyrolytic decomposition[6,9]. Furthermore, a co-solvent can be added inorder to tune the oxidizing potency of the atmosphere wherethe reaction takes place[12]. Highly soluble precursors are preferred, and volatile molecules are required as co-product ofthe pyrolytic decomposition[2,15].

Taking into consideration the general rules reported above, a home made system was built up. Depositions are carried out in a confined environment, employing an air atomizer nozzle (PNR Air assisted ultrasonic atomizer, model MAD 0331 B1BA) placed at a distance of 29 cm from the deposition substrate (this was the maximum distance achievable). This type of nozzle presents the advantage of being quite robust, chemical resistant and easy to clean or substitute, although its performances in terms of particle size and their size distribution are quite poor. Air, nitrogen, oxygen or a mixture of them, were used as carrier gas and a mass flow controller (Vögtlin, model red-y) allowed a fine regulation of it. The oxygen concentration inside the chamber was monitored using an oxygen sensor (Sensor technics, model XYA1) placed at a distance of 35 cm away from the nozzle, in order to control the oxidation power of the environment where the reaction takes place. During the deposition, the substrate was kept at a constant temperature through a heater (Watlow model CER-1-01-00007) controlled by a closed loop PID system in order to get a fast response to any temperature variation. For the liquid delivery a peristaltic pump (Watson Marlow Pumps Peristaltic 520S) was used. Marprene pipes were used to carry the solution, and in order to avoid contaminations, different sets of pipes were used for different materials.

3.2.2. Pulsed laser deposition (PLD)

In order to deposit high quality thin film, pulsed laser deposition (PLD) was used as technique. The decision to use this physical vapour deposition technique over other possibilities was made in light of its great flexibility and due to the facility of depositing ternary and quaternary compound without any need for sophisticated vacuum hardware components[18,19]. These are also the reason why this technique is widely used for the deposition of multicomponent compounds, in particular oxides materials[19-21]. A scheme of the apparatus and a real image of the apparatus used are reported in Figure 3.2

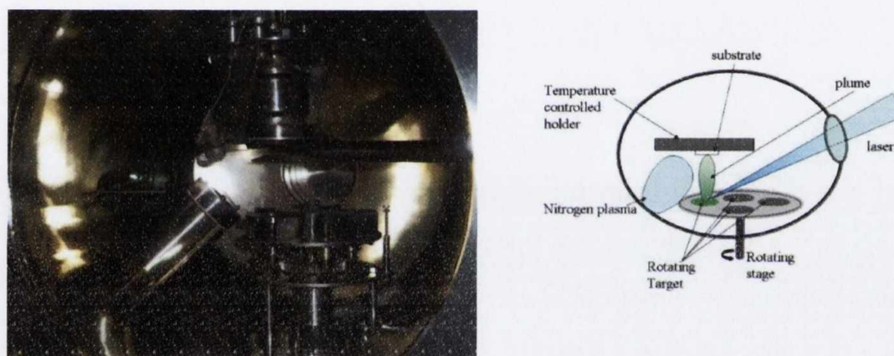

Figure 3.2 The PLD deposition chamber and a schematic view of the process.

Conceptually PLD is a very simple technique. A high power laser (in this case a KrF excimer laser, λ = 248 nm) is used as an energy source to vaporize the precursor materials of the target and thus to deposit a thin layer of material on top of an appropriate substrate. A set of optical components is used to focus the laser beam over the target surface. During the interaction of the laser with the solid target several complex physical processes occur. Understanding this interaction mechanism is a matter of research even nowadays, and several models have been proposed. However this is beyond the scope of the present dissertation and therefore only a general brief view will be given. In principal the entire process can be schematically represented in two steps: initially the laser photons are absorbed by the target material and as a result, a molten layer is forms on top of surface.

Following the vaporization processes occurs creating a recoil pressure on the liquid layer which contributes to expel the molten material[18,19,22]. This is a very simplified scheme. In reality the ablation process is much more complex and it depends on several parameters including the laser characteristics and the optical, topological and thermodynamic properties of the target. Going into more details, during the absorption process the electromagnetic energy is converted into electronic excitation and following into thermal, chemical and maybe even mechanical energy, which will lead to the evaporation and ablation process. The atoms and the particles that evaporate form the so called "plume", a mixture of highly energetic species including atoms, molecules, electrons, ions clusters and particles with average size in the micrometre range and molten globules. Immediately after the evaporation, the plume rapidly expands into the vacuum creating a nozzle jet directed towards an appropriate substrate. It is worth noting that there is a minimum energy, defined as "*ablation threshold*", which is required to set off the evaporation process itself[18]. The threshold value depends both on the material and the laser characteristics, corresponding to laser energy fluencies usually between 0.1 and 1 J/cm^2. In order to get films with good properties, i.e. smooth and stoichiometric epilayers, lasers operating in the ultraviolet range, short pulse width (~30 ns) and laser fluency just above the ablation threshold are preferred[18].

This techniquehas several advantages compared to other physical vapour deposition technique. Firstly, the evaporation power source and the vacuum hardware component are decoupled, giving an extra degree of flexibility and the possibility of choosing among different deposition conditions, spanning from high vacuum to highly reactive environment[21,23]. In principle oxygen or nitrogen plasma sources can be used to create highly reactive environment, however in the present apparatus, although it was present, the plasma source was out of order for the time of use of the chamber. Another advantage is given by the possibility of inserting several elements in the same target. In this way, simultaneous deposition of elements can be done starting from a single source, without the difficulties of dealing with co-evaporation processes. In fact, congruent evaporation is possible due to the fast and strong heating of the target (temperature up to

5000K within few ns), which leads to simultaneous evaporation of all the different species present in the target regardless of their particular binding energy. In this way the stoichiometry of the target is preserved during the ablation[23]. Therefore, if the sticking coefficient of the different elements on the substrate is not too different, stoichiometric transfer from the target to the deposited films can be achieved[19-23]. Moreover, compared to other deposition techniques, relative high deposition rates can be achieved[18].

Of course there are also some disadvantages. The principal problem is that the high focused nature of the plume makes difficult to scale up the PLD method, therefore only small areas, usually of about 1 cm^2, can be deposited by using this technique. Furthermore smoothness of the film is quite often compromised by the presence of blobs on the surface due to the formation of particulates during the deposition process. Another disadvantage is the necessity of polishing the target after every film deposition due to the extensive erosion. Finally care has to be taken in cleaning the window and the walls of the chamber to remove the residue of deposited material as this can represent a possible source of contamination[18].

For the deposition, different target substrates were prepared. Solid state reactions were used for the purpose. Detailed description of this process will be given in the experimental section. For the deposition laser fluencies of 0.1-0.5 J/cm^2 were used. Different repetition rate of 5 or 10 Hz were used. Al_2O_3 was used as the substrate for a temperature range spanning from 400 to 650 °C. Oxygen back-pressure was used in order to compensate for the loss of oxygen in the deposited film with respect to the target material. Pressures up to 100 μbar were used.

3.3. Characterization

For the characterization of transparent conducting oxides, both optical and electrical properties need to be determined. A complementary set of analysis such as crystal structure, composition, morphology and thickness determination were necessary to fully understand the physical

properties of the materials produced. Thus a variety of techniques have been employed for the characterization, which will be only briefly outlined in this section.

3.3.1. Electrical characterization

Electrical characterization was carried out by measuring both the conductivity and the Hall coefficient.

For the conductivity measurements both linear configuration and Van der Paw configuration were adopted.

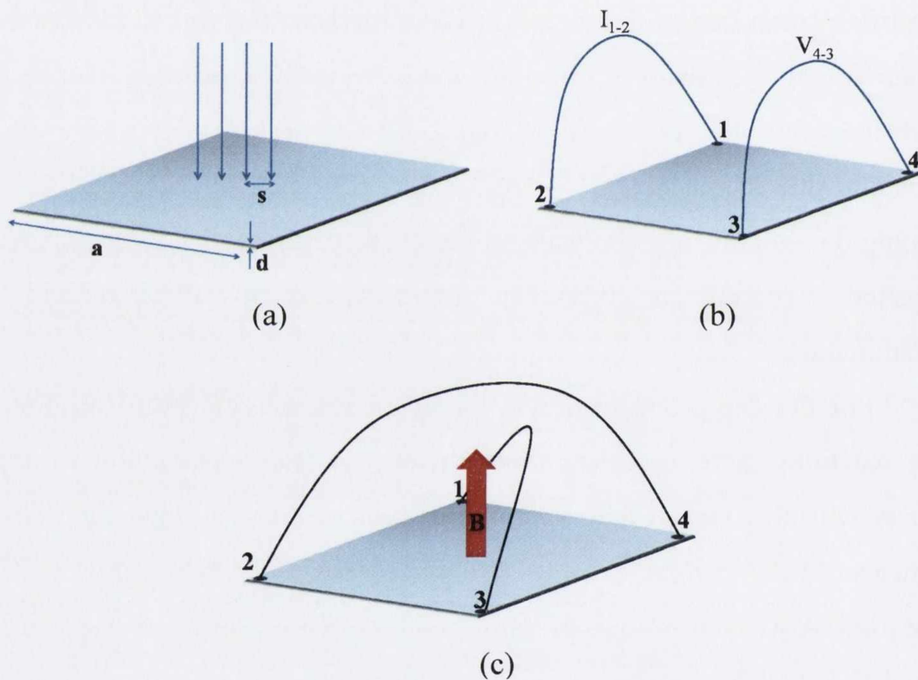

Figure 3.3 Schematic representations of (a) the linear configuration set-up, (b) the Van der Pauw geometry used for resistance measurements,(c) the Van der Pauw geometry used for Hall measurements.

In the linear configuration (Fig. 3.3a) a small constant current is passed through the two outer probes and the voltage is measure between the inner two. The linear configuration works under the assumption that the film thickness d is much smaller than the sample size (d«a). Furthermore the probing distance (s) is much smaller than the sample size (a), which allows

taking the correction factor CF equal to π/ln2[24]. Gold capped springs were used as contact probe with a distance of 2.5 mm.

In the Van der Pauw geometry (Fig. 3.3b)care was taken in placing the contacts at the outer corners of square samples, as wrong placement can produce misleading results[25-27]. Contacts were made by using colloidal silver glue. In this configuration the current was passed through contacts 1-2 and the voltage is measured between contact 4 and 3, thus the resistance $R_{12,43}$ can be determined. In order to verify the quality of the contact, the measurements were repeated by reversing the polarity ($R_{21,34}$) and swapping the contacts ($R_{34,21}$ and $R_{43,12}$). In this case R_A could be determined as in Eq. 3.1.

$$R_A = (R_{21,34} + R_{12,43} + R_{34,21} + R_{43,12})/4 \qquad 3.1$$

Then the current is applied between contact 2 and 3 and the voltage was measure through contact 1 and 4. By repeating the same procedure as above, R_B according to the Eq. 3.2

$$R_B = (R_{23,14} + R_{32,41} + R_{14,23} + R_{41,32})/4 \qquad 3.2$$

This set of resistance values is precious information in order to assess the quality of the contact layout and the homogeneity of the sample and the difference in the resistance was allowed to reach a maximum of 10% for any given sample. Following this, the sheet resistance R_{sh} can be determined numericallyaccording to the Van der Pauw equation (Eq. 3.3)

$$\exp(-\pi R_A / R_{SH}) + \exp(-\pi R_B / R_{SH}) = 1 \qquad 3.3$$

The core of the Hall measurements consists in determining the Hall voltage V_H. For this purpose the sample is placed in a constant magnetic field while a current is forced through the reaming contacts (for example 2 and 4). The voltage is then measured across opposite pair of contacts (for example 1 and 3). Measurements were repeated at reversed currents, swapped contacts, and opposite directions of the magnetic field. At each point the voltage was measured and the Hall voltage was calculated by averaging over the full set of data. In order to enhance the statistic, more than one value of magnetic field was used. In this way it was possible to evaluate the presence of any problem with the measurement (homogeneity of the sample, troubles with the contacts, limit in the resolution of the

system) by looking at the scatter in the data and the Hall resistivities measured at zero field. Once the Hall voltage (V_H) was determined it was possible to calculate the Hall coefficient (R_H), Hall mobility (μ) and carrier concentration (n) (Eq. 3.4-3.6)

$$R_H = \frac{V_H d}{B I} \quad 3.4$$

$$\mu = \frac{|R_H|}{\rho} = \frac{|V_H|}{B I R_{SH}} \quad 3.5$$

$$n = \frac{1}{e R_H} \quad 3.6$$

Where d is the thickness, B and I are the applied magnetic field and bias, R_{SH} is the sheet resistance, e the elementary charge. The sign of the Hall voltage depends on the type of carrier and it will be negative for electrons and positive for holes.

3.3.2. Optical properties

Optical properties were characterized by UV-Visible spectroscopy and spectroscopic ellipsometry. UV-Visible spectroscopy was performed on 2 different spectrophotometers. At the beginning of these studies only the Cary 50 UV-Vis-NIR-spectrophotometer was available. This is equipped with a Xenon lamp and can do transmission measurements over a range from 200 up to 1100 nm. Recently the Perkin Elmer 650 lamba spectrophotometer became available. This instrument operates in the wavelength range from 200 nm to 850 nm, and is equipped with a deuterium and a tungsten lamp. Integrated transmission, specular transmission, scattered transmission and specular reflection measurements can be performed with this instrument. The value of the total transmitted and scattered light can then be used to determine the haze of the sample. The spectrophotometric data were used in order to determine the transparency (via the absorption coefficient) of different material and the relative band-gap, by plotting $(\alpha E)^n$ vs E with n chosen to make the data linear near E_g. It is worth noting that this latter method works well for sharp transition, while

for broad transition it is rather inaccurate: the linearity is subjective and different values of n can lead to comparable linearity. Moreover for a given n the range of data to fit can make a considerable difference on the value of the intercept[28].

Determination of the refractive index was done by means of the variable angle spectroscopic ellipsometry (SOPRA GESP 5 Variable Angle spectroscopic ellipsometer) in the energy range from 1.5 to 5 eV.

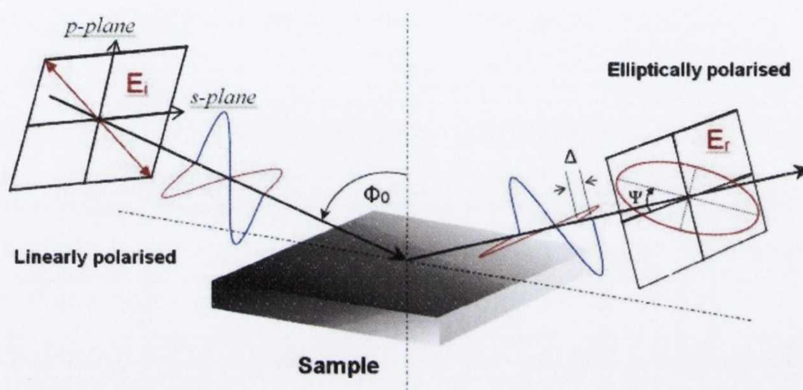

Figure 3.4 A schematic view of the optical process that is used for spectroscopic ellipsometry: a monochromatic linearly polarized light is elliptically polarized upon reflection with intensity difference (tanψ) and phase difference (Δ). Scheme to the courtesy of Mr. C. Smith

In spectroscopic ellipsometry, a monochromatic, linearly polarized electromagnetic plane wave travels throughout a medium (M0) and is reflected by another material (M1) under non-normal incidence (Figure 3.4). Upon reflection, the light is elliptical polarized. This means that, while the parallel and perpendicular vector components of the electric field of the incident light are in phase, the reflected components show a phase difference (Δ) and an intensity difference ($\tan\psi$). Both quantities are related to the optical properties of the material that caused the reflection (M1), and in particular to the ratio of the Fresnel reflection coefficients parallel r_p and perpendicular r_s to the plane of incidence respectively (Eq. 3.7)

$$\rho_e \frac{r_p}{r_s} = \tan\psi \exp(i\Delta) \quad 3.7$$

Making use of the Snell's law, it is possible to correlate the complex refractive index of the incident medium (N_0) and the reflecting material (N_1) in terms of ϕ and ρ as in Eq. 3.8.

$$\frac{N_1}{N_0} = \sin(\phi)\left[1 + \left(\frac{1-\rho}{1+\rho}\right)(\tan\phi)^2\right]^{1/2} \quad 3.8$$

In this case, the incident medium is air, therefore its refractive index (N_0) is known, while the ellipsometric ratio ρ_e is determined by measuring the values of the ellipsometric parameters cos(Δ) and tan(Ψ) in the energy range of interest and at different values of incident angles ϕ. This analytical expression is only valid for a single interface between a medium M1 and M0. For multilayer the ellipsometry data carry information about the pseudo-dielectric function of the material, in other words they are a convolution of the optical response of each layer inserted in the stack. For thin films the measured cos(Δ), tan(Ψ) values are also influenced by the interface roughness, film thickness and optical properties of the film and substrate. Multiple angles measurements are required in order to decouple the correlation between the refractive index (n) and the thickness of the sample (*d*). The complex dielectric function ε of the thin film is determined by fitting the experimental results with a multilayer model, in our case consisting of air, surface roughness, TCO and glass.

Lorentian oscillators or bulk critical points were used to build up a physical model able to represent the dielectric function of the material and they were used to fit the experimental data until conversion. For selected samples values of thickness were compared with those determined by cross sectional scanning electron microscopy (SEM) or x-ray reflectivity (XRR). Comparison with the transmission data was carried out in order to assess the validity of the dielectric function derived from the ellipsometric model.

3.3.3. Compositional analysis

The elemental composition of the deposited material was analysed by x-ray photoelectron spectroscopy (XPS) by using a using an Omicron MultiprobeXP system (Al X-ray source, E125 Analyser).

The basic principle of operation for the system is the ejection of an electron upon photo ionization by means of x-ray (or ultra violet light in UPS). In first order it is assumed that the electron is emitted without undergoing any dissipation process and therefore the kinetic energy it travels with is characteristic and reproducible. Indeed, the kinetic energy of the electron is thequantity that is experimentally measured, by means of a channeltron, while the sample, properly grounded, will undergo a series of relaxation process in order to dissipate the excess charge left behind. Since the x-ray excitation energy is known, the binding energy can be calculated in first approximation as the difference between the excitation energy and kinetic energy, provided that the work function for the instrument is known (Eq. 3.9, Figure 3.5)

$$E_{BE} = h\nu - E_{KE} - \phi_{spec} \quad 3.9$$

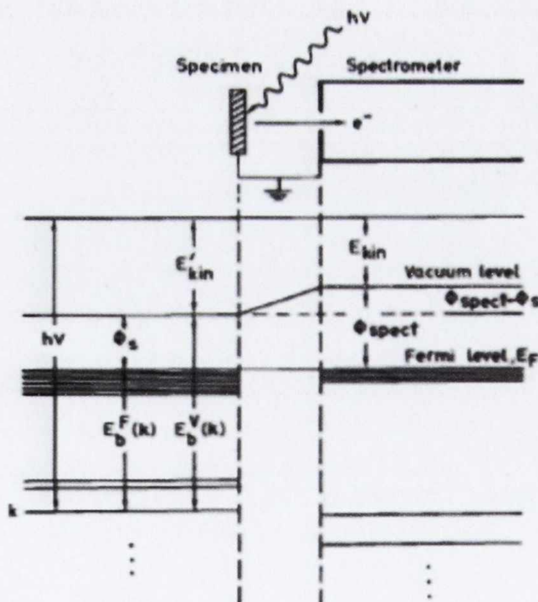

Figure 3.5 Schematic view of a photoelectron experiment. It is important to notice that sample and spectrophotometer must be in electrical contact in order for the Fermi levels to align[29].

For an Al source, $h\nu$=1486 eV. Each element give rise to a characteristic set of peak in the XPS spectrum whose position is determine by the binding energy of the orbital level probed while the area of the peak is determined by its scattering cross-section and by the actual amount of that particular element on the surface of the sample. Due to bonding formation, the electronic density of an atom may be changed. In this case a particular electron can suffer and increased or reduced screening of the nuclear attraction by means of the other electrons. As a result, the position of a peak can be shifted to higher or lower binding energy (*chemical shift*). In this case information about the chemical surroundings of an atom can be obtained within the resolution of the system. This depends on the entrance and exit slit, as well as the pass energy, integration time and step width, which can be adjusted in order to bring the resolution up to 0.6 eV. Since XPS is a surface sensitive technique (only the first few nanometers will be probed), samples were subject to cleaning prior measurements. This includes ultrasonic cleaning in high purity organic solvent (isopropanol, acetone, methanol), chemical cleaning in diluted HCl or HNO_3 solutions (pH=1) or in-situ using Ar ion sputtering at a pressure of 5×10^{-6}-1×10^{-5} mbar, beam energy in the range of 0.3-0.8 kV and an ion target current of 1.4-12 μA using an Omicron ISE 5 cold cathode ion sputter source. Experimental data were analysed by using the CasaXPS software.

3.3.4. Morphology

Morphology of the samples was analysed by atomic force microscope (AFM) and scanning electron microscope (SEM)

3.3.4.1 Atomic Force Microscope (AFM)

AFM was performed by using a NT-MDT SPM Solver PRO NT-MDT apparatus with a tip NSC35/AIBS or an Asylum MFP-3D™ Stand

Alone AFM apparatus and using single crystal silicon tip in non-contact mode. The scanning parameters such as scanning speed as well as PID setting for the piezo were adjusted depending on samples roughness. Topography analysis was performed by using the Gwyddion software and the value of the root mean square roughness could be determined.

3.3.4.2 Scanning electron microscope (SEM)

SEM imagines were obtained by using a Zeiss Ultra Plus - Scanning Electron Microscope, equipped with an in-lens detector. Both top view and cross-sectional images were taken. Voltage, astigmatism and focusing were adjusted in order to improve the resolution of the image.

3.3.5. Structural analysis

The crystallographic structure of the sample was investigated by means of x-ray diffraction. A number of different types of information can be gathered by means of this technique such as lattice parameters, epitaxiality of the film, dimension of the coherent diffraction domains, etc. Depending on the nature of the sample (powders, polycrystalline films and epitaxial films) different geometries have been employed: symmetric scans, grazing incident configuration, high resolution configuration. Despite the details of the geometry adopted for the scan, the basic underlying principal is the same, i.e. the measurement of the lattice spacing via the Bragg law (Eq. 3.10)

$$\lambda = 2d\sin\vartheta \qquad 3.10$$

However, different configurations allow accessibility to different details of the crystallographic properties, as outlined below. For this purpose the Bruker D8 Discover was used. On the source side this is equipped with a Cu tube, Gobel mirror and a monochromator. Depending on the type of measurements, different detectors can be used: for powders and high

resolution measurements a position sensitive detector (PSD) was used, while for grazing incidence diffraction Soller slits and a scintillation counter detector were used (Figure 3.6)

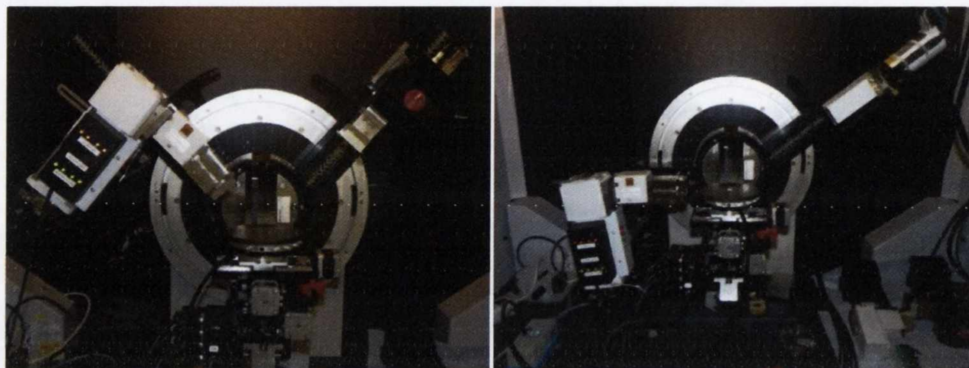

Figure 3.6 The Bruker D8 discover diffractometer in two different configurations: on the left the powders and high resolution configuration with the PSD detector; on the right the grazing incidence configuration with the Soller slits and scintillation counter detector.

3.3.5.1 Powders X-ray diffraction in parallel beam geometry

The simplest diffraction measurement that can be performed is the symmetric $\theta/2\theta$ scans. This configuration was adopted for powders and polycrystalline films and allows the determination of the crystallographic phase, its structure and lattice parameters.

In order to perform the measurements, powder samples were compressed into pellets or accommodated in the appropriate holder. In this case the sample was aligned in the x,y,z direction in order to be centred with respect to the incident beam and corrected for angular tilting (χ)

Analysis of the XRD patterns was done by using the MAUD software employing the Rietveld method[30]. Real physical quantity characteristics of the crystal such as crystal structure parameters, dimension of the coherent diffraction domains, microstrain and texture, Debye-Waller factor are used in the fitting procedure and their value can thus be determined by analysing the XRD patterns.

The principal of this method is to minimize the residual function (weighted sum of squares WWSEq. 3.11) by a non-linear least squares algorithm[30].

$$WSS = \sum_i \frac{1}{\sqrt{I_i^{\exp}}} (I_i^{\exp} - I_i^{calc})^2 \qquad 3.11$$

Where $I_i^{\exp}$ is the intensity of the experimental XRD patterned while the calculated intensity I_i^{calc} (Eq. 3.12)

$$I_i^{calc} = S_F \sum_{k=1}^{N\ peaks} L_k |F_k|^2 S(2\vartheta_i - 2\vartheta_k) P_k A + bkg_i \qquad 3.12$$

In a spectrum having N peaks (where N depends on the symmetry and space group), the intensity of a 2θ position *i*, will be determine by background value bkg_i and by the present and intensity of peaks at that value. The background function is described by a polynomial of second order. The kth peak can be described by its position $2\vartheta_k$, by the diffraction intensity and by a line broadening (or profile shape function $S(2\vartheta_i - 2\vartheta_k)$).

The position $2\vartheta_k$ will be calculated according to the Bragg law using the d-spacing of the *hkl* reflection and using a reciprocal space mapping (Eq. 3.13 - 3.14)[30].

$$d_{hkl} = \frac{V_C}{\sqrt{s_{11}h^2 + s_{22}k^2 + s_{33}l^2 + 2s_{12}hl + 2s_{13}hl + 2s_{23}kl}} \qquad 3.13$$

$$S = \begin{pmatrix} a^{*2} & a^* b^* \cos\gamma^* & a^* c^* \cos\beta^* \\ a^* b^* \cos\gamma^* & b^{*2} & b^* \cos\alpha^* \\ a^* c^* \cos\beta^* & b^* c^* \cos\alpha^* & c^{*2} \end{pmatrix} \qquad 3.14$$

The intensity will be given by the incident beam intensity S_F, the Lorentz-Polarization factor L_k, the structure factor F_k, the presence of texture P_k and the absorption factor A. The structure factor carries the information about multiplicity of the reflection, m_k, the cell structure, the Debye-Waller temperature factor (B_n) and is defined as in Eq. 3.15

$$|F_k|^2 = m_k \left| \sum_{n=1}^{N} f_n e^{-B_n \frac{sen^2 \vartheta}{\lambda^2}} (e^{2\pi i(hx_n + ky_n + lz_n)}) \right|^2 \quad 3.15$$

Where N is the number of atoms, x_n, y_n, z_n are the coordinates of the nth atoms and f_n is atomic scattering factor of the nth atom and h, k, l are the Miller indices.

In any sample where texturing was present, the March-Dollase formula was used (Eq. 3.16)

$$P_{k,j} = \frac{1}{m_k} \sum_{n=1}^{m_k} \left(P_{MD}^2 \cos^2 \alpha_n + \frac{\sin^2 \alpha_n}{P_{MD}} \right)^{-\frac{3}{2}} \quad 3.16$$

Where the sum runs over all equivalent hkl reflection (m_k) P_{MD} is March Dollase parameter and α_n is the angle between the preferred orientation vector and the crystallographic plane hkl[30].

The broadening of a peak is determined by two contributions: the sample broadening which is taken into account via the profile shape function $S(2\vartheta_i - 2\vartheta_k)$ and the instrumental broadening. These two contributions are treated separately. For the instrumental broadening a Cagliotti-like formula is used. The instrumental broadening was determined for each different configuration of the diffractometer (different slits and detector type can in principle affect it) by using a single crystal Si sample. In this case, due to the large diffraction domains and low impurity levels, it can be assumed that the peak broadening is completely determined by the instrumental resolution. Once the parameters for the instrumental broadening have been determined by iterativeoptimization of the parameters used in the Cagliotti formula, their values isin a separate file and the used for the analysis of samples.

3.3.5.2 Grazing incidence X-ray diffraction (GIXD)

X-ray radiation has a large penetration depth into any matter, making the analysis of thin films quite difficult because of the small diffracting

volume, which results in low diffracted intensity in comparison to the substrate and background signal. In particular the parallel beam geometry is only partially suitable for the study of polycrystalline thin films grown on glass due to the high peak to background ratio, and therefore to the large contribution of the substrate to the signal. Grazing incidence configuration is a method to overcome this limitation. By applying a small angle of incidence (1°) of the incident x-ray beam, the penetration depth is strongly reduced (couple of order of magnitude) and the path length of the X-rays through the film is enhanced, thus maximizing the response from the thin layers. Moreover the penetration depth is kept constant over the entire spectra range, thus enabling a good signal to noise even at high angle of diffraction. In a polycrystalline material the crystallite will be randomly oriented in such a way that some of them will satisfy the Bragg condition (Figure 3.7).The diffracted beam can then be paralleled in the Soller slit attachment. The grazing incident angle (ω_{gi}) in this study has been kept fixed in order to probe always the same amount of material throughout the entire 2θ range. The drawback in this case is that no highly oriented film can be measured with the present diffractometer and long integration time is required.

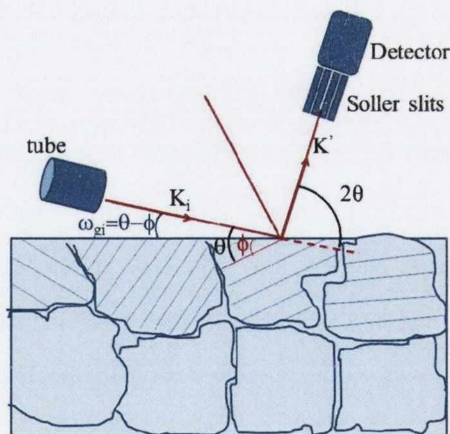

Figure 3.7 Schematic view of the grazing incidence diffraction configuration for analysis of polycrystalline films

3.3.5.3 High resolution x-ray diffraction (HRXRD)

High resolution x-ray diffraction is a powerful tool to study the properties of epitaxial films. A good amount of information can be gathered such as structural parameters, epitaxial relationship for hetero-epitaxial grown films, Poisson ratio for strained films, presence of mosaic effects.

In the present thesis, this study was applied to Cr_2O_3 grown on sapphire. The presence of stain in the grown film is determined by the difference in the lattice mismatch (Δ_l) between the substrate lattice parameters (a_s) and the epitaxial film lattice parameter (a_f)[31] (Eq. 3.17).

$$\Delta_l = \frac{a_f - a_s}{a_f} \quad 3.17$$

The strained energy induced by the lattice mismatch builds up to a threshold value above which the epitaxial films lattice constants tend to relax to their bulk values. This threshold thickness is said to be the critical thickness (t_c) and its value can be determined according to the Eq. 3.18 [31].

$$t_c \approx \frac{a_f}{2\Delta_l} \quad 3.18$$

In the present thesis, HRXRD analyses were performed on chromium oxide film grown on sapphire. Due to the lattice mismatch the critical thickness was expected to be of about 5 nm. Since the minimum thickness value desired was 20 nm, the films were expected to be fully relaxed. For this reason, the HRXRD aimed only to determine the epitaxial relationship between films and substrate. To this end, both in plane and out of plane XRD pattern were collected.

For the out of plane pattern, samples were aligned with respect to the substrate. The sapphire (006) reflex was used. Correction for sample tilting (α) and for the inter-planar angle was achieved by iterative optimization of the χ and ω scanning parameters. Patterns were collected over an appropriate angular range.

For the in plane scan, a substrate reflex corresponding to a plane non parallelto the surface plane was chosen for the alignment. In this case also the ψ anglewas optimized in order to be in Bragg condition for the particular plane of choice. Moreover in order to verify what was the epitaxial relationship and if there was any in-plane rotation, the presence of the same reflex from the epitaxial film was recorded. A ψ–scan was then performed to verify the symmetry of the diffraction plane (Figure 3.8).

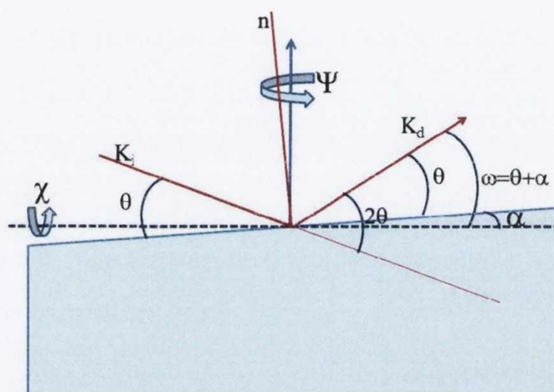

Figure 3.8. Scheme of the diffraction geometry for high resolution measurements of epitaxial films deposited on single crystal sapphire.

3.3.6. Thickness determination

As described above, optical measurements were often employed in order to determine the thickness. Nevertheless, many times, an independent method to evaluate it was required. To this end, X-ray reflectivity represents a powerful tool to get precise and quick results. However the major limitation is that only thickness lower than 100 nm can be probed and smooth samples are required. These criteria were met most of the time for PLD grown samples, while they were not fulfilled for those samples grown by spray pyrolysis. In this latter case, cross sectional scanning electron microscopy was performed. Details of these two methods are given below.

3.3.6.1 X-ray reflectivity (XRR)

The interaction of x-ray with matter gives rise to other two important optical phenomena, reflection and refraction governed by Fresnel equations and Snell law respectively. Together, they can be used to determine the thickness of thin layers.

The basic principle of X-ray reflectivity is to measure the intensity of a reflected x-ray beam near a glancing incidence configuration. The reflection at the surface and interface of the film is due to the difference in electron densities in different layers which corresponds to different reflectivity index.

Since only specular X-ray reflectivity was performed, the incident angle (θ_i) is equal to the reflected angle and the scan is performed over a 2θ range less than 6 degrees (Figure 3.9).

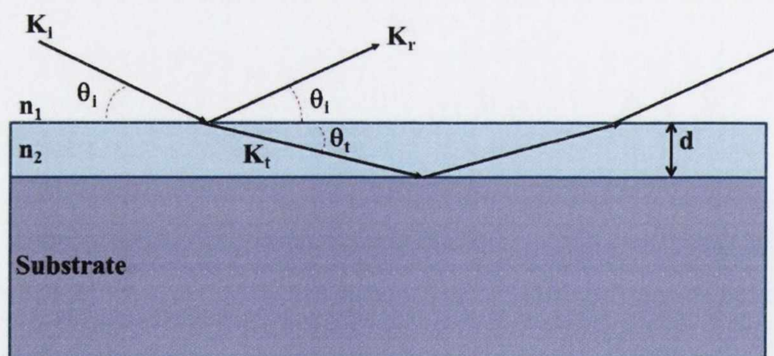

Figure 3.9. Scheme of the x-ray reflection process at the top and the bottom of a thin film.

The refractive index of a medium in the x-ray range can be written as in Eq. 3.19.

$$n = 1 - \delta - i\beta \qquad 3.19$$

Where δ represents the dispersion term and β the absorption term as in Eq. 3.20.

$$\delta = \frac{r_0 \lambda^2}{2\pi} n_e \qquad 3.20$$

Where r_0 is the Bohr radius, λ the x-ray wavelength and n_e the electron density given by Eq. 3.21.

$$n_e = Z \frac{N_A}{A} \rho_d \qquad 3.21$$

Being N_A the Avogadro numbers, A the atomic weight ρ_d the density and Z the number of electrons per atom. This latter is usually replaced with the complex atom form factor f (Eq. 3.22).

$$f = f_0 + f' + if'' = Z + f' + if'' \qquad 3.22$$

Where f' and if'' are due to dispersion and absorption (Eq. 3.23 – 3.24)

$$\delta = (Z + f') \frac{N_A}{A} \rho_d \frac{r_0 \lambda^2}{2\pi} \qquad 3.23$$

$$\beta = \frac{r_0 \lambda^2}{2\pi} f'' \frac{N_A}{A} \rho_d \qquad 3.24$$

δ and β are small positive quantities, thusthe refractive index is slightly smaller than 1 in this region and transmitted waves will be refracted. Thus Snell law can be applied (Eq. 3.25).

$$n_1 \cos(\vartheta_i) = n_2 \cos(\vartheta_t) \qquad 3.25$$

At a critical angle θ_C, X-rays will undergo a total internal reflection going from a medium of high refractive index to one of low refractive index. By assuming that no absorption takes place (β=0) and in the case of n_1 being air, it can be proven that the critical angle is dependent on δ and therefore proportional to the density of the material (Eq. 3.26)

$$\vartheta_C = \sqrt{2\delta} \propto \sqrt{\rho_d} \qquad 3.26$$

This proves why no XRR can be measured if there is no density difference.

For incident angles higher than the critical angle, X-rays will penetrate in the film, and reflection will occur at the bottom and at the top of the layer. The interference between the x-ray reflected at these interfaces will results in interference fringes (Kiessig fringes). The spacing between

this interference fringes is proportional to thickness of the layer according to Eq. 3.27

$$d \approx \frac{\lambda}{2} \frac{1}{\vartheta_{,m+1} - \vartheta_m} \tag{3.27}$$

The analysis of the XRR data was performed by using the Laptos software. In this package the Fresnel reflectivity is calculated by using the recursive Parratt's formalism.

The procedure described so far is correct only for abrupt ideal interface. In reality real material have some level of surface roughness that gives rise to diffuse reflection. The theoretical treatment of this latter is allowed in the Laptos package provided that the amount is limited to few nanometres.

Overall the simulation allows the determination of the thickness, roughness and density of each single layer inserted into the stack.

3.3.6.2 Crosse sectional Scanning Electron Microscopy (SEM)

Sample prepared by spray pyrolysis and sample deposited by PLD in non-optimum conditions are too rough to be analysed by XRR. In this case cross sectional SEM was performed. The only difference with respect to the description given above is about the sample preparation. In this case, a thin slab of material was mounted vertically, given only a little bit of inclination for avoiding in depth view. Samples were then fixed using silver paint. In-lens detector was used for the imaging at the characteristic acceleration energy of 2kV.

(1) Perednis, D.; Gauckler, L. J. *Journal of Electroceramics* **2005**, *14*, 103-111.

(2) Roger, C.; Corbitt, T.; Xu, C.; Zeng, D.; Powell, Q.; Chandler, C. D.; Nyman, M.; Hampden-Smith, M. J.; Kodas, T. T. *Nanostructured Materials* **1994**, *4*, 529-535.

(3) Sears, W. M.; Gee, M. A. *Thin Solid Films* **1988**, *165*, 265-277.

(4) Schwartz, R. W.; Schneller, T.; Waser, R. *Comptes Rendus Chimie* **2004**, *7*, 433-461.

(5) Blandenet, G.; Court, M.; Lagarde, Y. *Thin Solid Films* **1981**, *77*, 81-90.

(6) Patil, P. S. *Materials Chemistry and Physics* **1999**, *59*, 185-198.

(7) Neagu, R.; Perednis, D.; Princivalle, A. s.; Djurado, E. *Chemistry of Materials* **2005**, *17*, 902-910.

(8) Heine, M. C.; Pratsinis, S. E. *Industrial & Engineering Chemistry Research* **2005**, *44*, 6222-6232.

(9) Wang, M.; Kim, E. J.; Shin, E. W.; Chung, J. S.; Hahn, S. H.; Park, C. *The Journal of Physical Chemistry C* **2008**, *112*, 1920-1924.

(10) Ocampo, E.; Arce, R.; Koropecki, R. R.; Buitrago, R. H. *Solar Energy Materials and Solar Cells* **1995**, *36*, 327-337.

(11) Bouzidi, A.; Benramdane, N.; Tabet-Derraz, H.; Mathieu, C.; Khelifa, B.; Desfeux, R. *Materials Science and Engineering B* **2003**, *97*, 5-8.

(12) K. F. Huo, Z. H., J. J. Fu, H. Xu, X. Z. Wang, Y. Chen, Y. N. Lü, B. H. Liu, J. Ding. *Journal of Materials Research* **2003**, *18*, 1641-1645.

(13) Muecke, U. P.; Luechinger, N.; Schlagenhauf, L.; Gauckler, L. J. *Thin Solid Films* **2009**, *517*, 1522-1529.

(14) Muecke, U. P.; Messing, G. L.; Gauckler, L. J. *Thin Solid Films* **2009**, *517*, 1515-1521.

(15) Chen, C. Y.; Tseng, T. K.; Tsai, S. C.; Lin, C. K.; Lin, H. M. *Ceramics International* **2008**, *34*, 409-416.

(16) Hernandez-Fenollosa, M. A.; Lopez, M. C.; Donderis, V.; Gonzalez, M.; Mari, B.; Ramos-Barrado, J. R. *Thin Solid Films* **2008**, *516*, 1622-1625.

(17) Bacaksiz, E.; Parlak, M.; Tomakin, M.; Ozcelik, A.; Karakiz, M.; Altunbas, M. *Journal of Alloys and Compounds* **2008**, *466*, 447-450.

(18) Herman, M. A.; Richter, W.; Sitter, H. *Epitaxy Physical Principles and Technical Implementation*; Springer: Berlin, 2004.

(19) Christen, H. M.; Eres, G. *Journal of Physics: Condensed Matter* **2008**, *20*, 264005.

(20) Habermeier, H. U. *Applied Surface Science* **1993**, *69*, 204-211.

(21) Afonso, C. N.; Gonzalo, J. *Nuclear Instruments and Methods in Physics Research Section B: Beam Interactions with Materials and Atoms* **1996**, *116*, 404-409.

(22) Boyd, I. W. *Ceramics International* **1996**, *22*, 429-434.

(23) Kramer, B.; Krebs, H.-U.; Weisheit, M.; Faupel, J.; Suske, E.; Scharf, T.; Fuhse, C.; Stormer, M.; Sturm, K.; Seibt, M.; Kijewski, H.; Nelke, D.; Panchenko, E.; Buback, M. In *Advances in Solid State Physics*; **2003,** 43, 505-518.

(24) Rymaszewski, R. *Journal of Physics E: Scientific Instruments* **1969**, *2*, 170-174.

(25) Ohgaki, T.; Ohashi, N.; Sugimura, S.; Ryoken, H.; Sakaguchi, I.; Adachi, Y.; Haneda, H. *Journal of materials research* **2008**, *23*, 2293-2295.

(26) Bierwagen, O.; Ive, T.; Van de Walle, C. G.; Speck, J. S. *Applied Physics Letters* **2008**, *93*, 242108-3.

(27) Krtschil, A.; Look, D. C.; Fang, Z. Q.; Dadgar, A.; Diez, A.; Krost, A. *Physica B: Condensed Matter* **2006**, *376-377*, 703-706.

(28) Antonio Facchinetti, T. J. M. *Transparent electronics From synthesis to application*; Wiley, 2010.

(29) C.R. Brudle; Baker, A. D. *Electron Spectroscopy: Theory, Tecnique and Applications*; Academic press: London, 1978; Vol. 2.

(30) http://www.ing.unitn.it/~maud/.

(31) Sze, S. M. *Semiconductor Devices Physics and Technology*; John Wiley & son, 2002.

Chapter 4

n-type TCOs

4.1. State of the art

All the commercially employed TCOs are n-type and among this In_2O_3:Sn, SnO_2:F, ZnO:Al are the most widely used. The success of these oxides lays on their outstanding physical properties, in particular large band gaps, great flexibility in impurity doping leading to highly tunable and controllable carrier concentration while maintaining good electron mobility[1]. As outlined in Chap. 2 there are intrinsic limits on theproperties that a TCO can achieve and for the most commonly reported TCOs (AZO, FTO, ITO) this target has been achieved[2-4].At the same time the increasing demand for TCOs with improved performance strongly stimulated the search for new materials[5-8]. Although conventional TCOs have been studied for the last 20 years, attention has not drop. There are two reasons for that. From the fundamental point of view there are still unanswered question, the prominent one being about the conductive mechanism[9,10]. In these oxides, n-type conductivity is the result of both unintentional doping, whose causes are still under debate[9,11], and appropriate substitutional doping with aliovalent ions[12]. The former is readily achieved by tuning the oxygen content during the deposition process, however the latter is preferable in order to achieve a better control over the optical and electrical properties[12]. Better understanding of both is required in order to design new and improved materials. Second, record conductivity and transparency has been achieved on a laboratory scale. The challenge in this case is more technological, i.e. transfer of high quality material into a cost-effective industrial production process[13]. Moreover, as the requirement for improvement of devices performance increases, the pathway to achieve this is often based on material engineering especially at the interfaces. In this case, the possibility of tuningmaterial properties such as band-gap[14,15] and work-function[16-18], refractive index[19], fine-tuning of mobility and carrier concentration[20], morphology[3] or even etching characteristics[16,20,21] is required for either new or commonly employed TCOs to match devices requirements.

4.2. Zinc oxide and Aluminum Zinc Oxide (AZO)

Zinc oxide is one of the most commonly used TCO in solar cells. Due to its abundance, low price and non-toxicity, it is considered an ideal replacement for the scarce and expensive indium oxide. Moreover its outstanding physical properties such as the large exciton binding energy (60 meV) and good electrical conductivity and wide band gap (~3.4 eV) make it a good candidate for implementation in opto-electronic devices such as solar cells[22,23], OLEDS[24], LEDs[25] and TFTs[9]. Some of these properties such as luminescence, although interesting, are beyond the scope of the present thesis and therefore will be excluded from this overview. The literature production on ZnO is quite wide including book[26], several reviews[9,27-31] and thousands of articles, therefore only the aspects which were of primary importance for the present study will be revised.

ZnO can have three different crystallographic structures, zinc blende, rocksalt or wurtzite, the latter being the most stable under ambient condition[9]. In this structure Zn is tetrahedrally coordinated by 4 oxygen atoms and oxygen atoms are tetrahedrally coordinated by 4 zinc atoms. The structure consists of an hexagonal close packing of oxygen atoms with the zinc atoms filling half of the tetrahedral holes[16,32]. The wurtzite structure has a hexagonal unit cell with lattice parameters a=3.2489Å and c=5.2049Åand belongs to the space group $P6_3mc$.[9] Band structure calculations show that ZnO is a direct gap semiconductor, with both conduction band minimum and valence band maximum occurring at the Γ point[27].

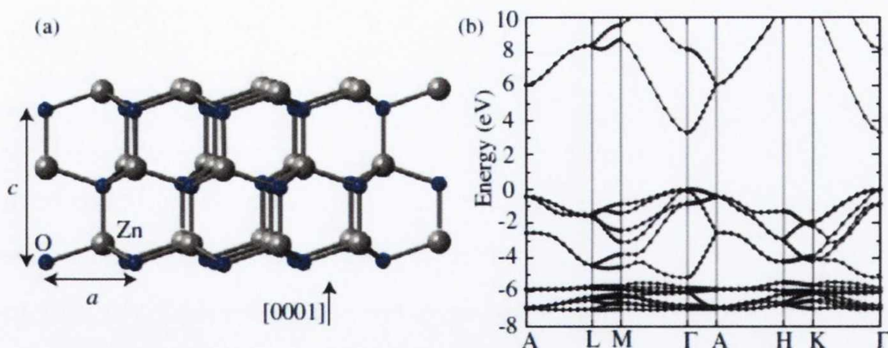

Figure 4.1 Crystal structure and band structure calculation of ZnO. Taken from 27.

In its stoichiometric form it is insulating, however, native defects make it an n-type semiconductor under most of the growth condition. The origin of this unintentional doping is still a matter of debate. Historically, it was attributed to oxygen vacanciesand Zn interstitials[9,11,27,33-35], however recent studies showed that these defects are respectively lying too deep to make any reasonable contribution to the conductivity or have a high energy formation so their concentration should be low[11,27,34]. The presence of hydrogen impurities have been proposed in order to account for the spontaneous conductivity[27,36,37], however further studies showed that conductivity persist even when hydrogen was not present or had been removed[11,38]. Conductivity can be further improved by substitution doping on the cation. It was demonstrated that B, Al, Ga and In and can act as effective doping elements. In the present thesis only Al doping (Al:ZnO, AZO) will be taken into consideration. Recently several attempts to produce p-type ZnO were reported, however there are strong limitation in the reproducibility and stability[9,27,28,30,39-44].

From the optical point of view, ZnO has a direct band gap of 3.37 eV and a refractive index of 2.008[29] One of the major feature of ZnO is that both the band gap and its refractive index can be modified to meet desired properties (anti-reflecting properties or control of the band lined up by band-gap engineering[14,15,27])

On industrial scale, ZnO is produced mainly by plasma enhanced chemical vapor deposition (PECVD) or magnetron sputtering[12], however

several other techniques (PLD[14,45,46], CVD[15], or SP[47]) are routinely employed on small scale for its deposition.

It is understood that processing conditions have a large effect on determining the TCO properties[12]. In this regard an extensive study has been carried out on deposition of ZnO and Al:ZnO by spray pyrolysis. The purpose of the studies was not to achieve the record conductivity but to understand the effect of the chemicals in obtaining the desired physical properties. Since most of the chemicals involved are also used in CVD, results are not confined to the spray pyrolysis technique but are more general.

4.2.1. Effect of the chemical precursors on the properties of deposited film

In this chapter the results from the optimization of deposition parameters for ZnO and Al:ZnO will be presented.

Decomposition temperature for each precursor was varied from 573 to 723 K, with steps of 50K. For the sake of simplicity the temperatures reported are the ones referring to the heater set point. However, in order to measure the thermal gradient across the glass slide and cooling power due to the air stream and the spray solvents, a type K thermocouple (nickel-chromium) was placed in test experiments within 1 mm above the glass surface, in a region where the reaction is expected to happen. For the actual sample growth this was removed to have an unobstructed sample surface.

For the synthesis, all the chemicals were purchased from Sigma-Aldrich and used without any further purification. The solvents employed were methanol, ethanol, both HPLC-grade, and deionised water. For selected samples, a mixture of them was used. For the ZnO synthesis, $Zn(CH_3CO_2)_2{\cdot}2H_2O$, $Zn(NO_3)_2{\cdot}6H_2O$, and $ZnCl_2$ were used as Zn source. In all cases a 0.2 M solution was used.

The following precursor solutions have been used for sample growth: zinc acetate was employed both with water, methanol and a mixture of ethanol/methanol equal to 70/30. The use of this has been necessary in order to speed up the dissolving process. Moreover in order to test the influence of water as solvent, mixtures with ratios of CH_3OH/H_2O equal to 75/25, 50/50, 25/75 have been tested as well.

The $ZnCl_2$ precursor was employed either with water, methanol and ethanol, as well as in a mixture of H_2O/CH_3CH_2OH. The $Zn(NO_3)_2{\cdot}6H_2O$ precursor was used just in full methanol, based on the results for the other precursors. In this case extra care needed to be taken in the preparation of the solution in order to avoid the possible auto-ignition of the solution itself.

For all samples the liquid flow rate was fixed to 2.66 ml min^{-1}, the gas flow was 14 l min^{-1}. The best decomposition temperature was 623 K for the acetate and nitrate precursors while for the chloride the decomposition temperature was 673 K.

Doping has been carried out employing $Mg(CH_3CO_2)_2{\cdot}4H_2O$ and $MgCl_2{\cdot}6H_2O$ as magnesium source, $AlCl_3{\cdot}9H_2O$ and $Al(NO_3)_3{\cdot}9H_2O$ and $Al[OCH(CH_3)_2]_3$ for aluminum. For the dissolution of the aluminum isopropoxide, a mixture of 70% isopropanol and 30% methanol has been used. The optimum concentration ratio of these doping agents was [Mg]/[Zn] = 10% and [Al]/[Zn] = 4% (solution concentration). These values have been chosen taking into consideration the data reported in literature[48-55] and the results of the screening procedure carried out over a larger range of Al/Zn and Mg/Zn ratios. Due to the small fraction of doping agent present, all other parameters were kept as reported above for the undoped ZnO.

4.2.2. Role of solvent

The role of solvent has been tested employing both zinc acetate and zinc chloride as precursors. Using the organic precursor, the ZnO layer was obtained employing water, methanol or a mixture of them. Several films have been grown changing the solvent compositions (ratio between water and methanol) as follows: 100/0, 75/25, 50/50, 25/75, 0/100. All the other

parameters were kept constant. Despite the different solvent composition, from the crystallographic point of view, all the samples consist of just one phase, zincite (PDF number 01-074-0534), with hexagonal structure. No traces of unreacted precursors have been found (acetate: PDF-033-1464, chloride: PDF-01-072-1285). The refinement carried out with MAUD indicates that the cell parameters are: a =3.246Å, c =5.2058 Å. The sample grown in pure methanol and the one with a solvent composition containing 25% of water show dominantly (002) oriented crystals, while for all the others, a good fit can be obtained only assuming that the sample is composed of different micro-crystallites, some of which have a (002) and others have (100) preferred orientation.

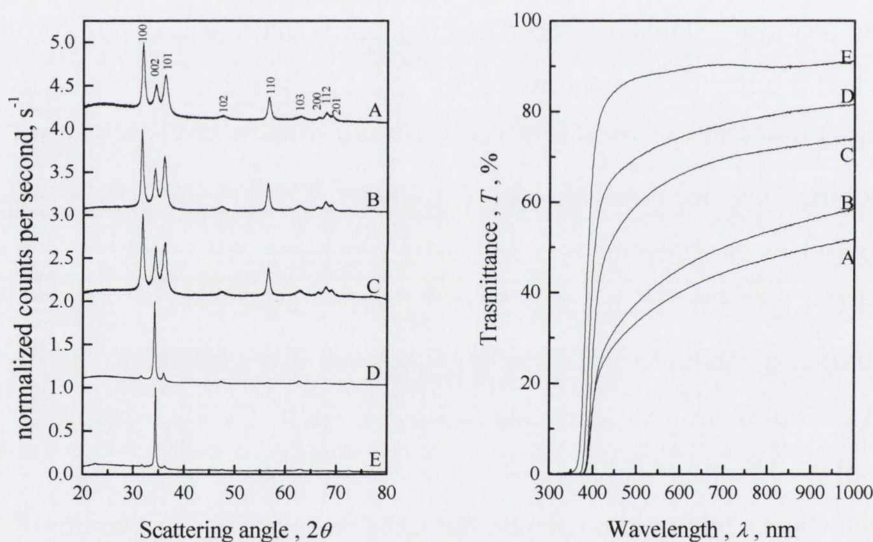

Figure 4.2 Effect of the solvent composition on the crystallographic (a) and optical (b) properties of ZnO: (A) 100%water, (B) 75%water - 25% methanol, (C) 50% water-50% methanol, (D) 25% water – 75% methanol, (E) 100% methanol.

The presence of the salt was not interfering with the preferential growth of (002) oriented films when methanol was used as solvent. In fact SEM top view of films grown by using water shows random facets, while for film grown by using methanol hexagonal structures are clearly showed (Figure 4.3).

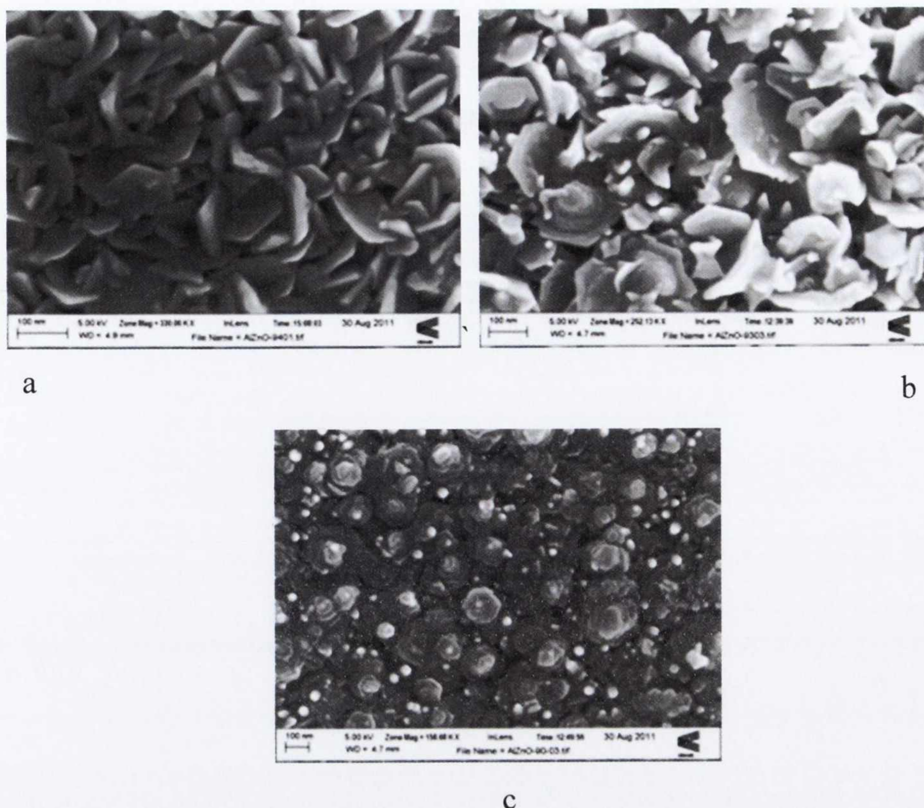

Figure 4.3 SEM top view of ZnO:Al (Zn:Al=98.5:1.5)in three different solvents; (a) water, (b) a mixture (50:50) of water and methanol, (c) methanol.

Only the methanol grown films are smooth enough to observe typical Fabry-Perot oscillations. For high water content, the absence of such oscillations is due to the diffuse scattering of light, which prevents the formation of a regular pattern of constructive and destructive interference. Surface roughness is related to the physiochemical properties of the solvents themselves, as it will be illustrated later in the chapter, to the thickness of the samples and to the growth rate, which, in turn, is a function of liquid delivery rate, precursors' concentration, nozzle position with respect to the substrate, deposition temperature. Moreover, for a given temperature, good thermal contact between the heater and the substrate has a strong effect as well. All these parameters have been optimized to keep roughness values as low as possible, and thus, been able to use the Fabry-Perot oscillations to determine the thickness. Whenever present, the spacing in energy between two maxima of interference represents the ΔE value of equation 2.23 (Figure 4.4), while the refractive index value was taken from literature. For those samples where no Fabry-Perot oscillations were visible, other methods

such as weight of the glass slide, or, even better, cross-sectional SEM were used.

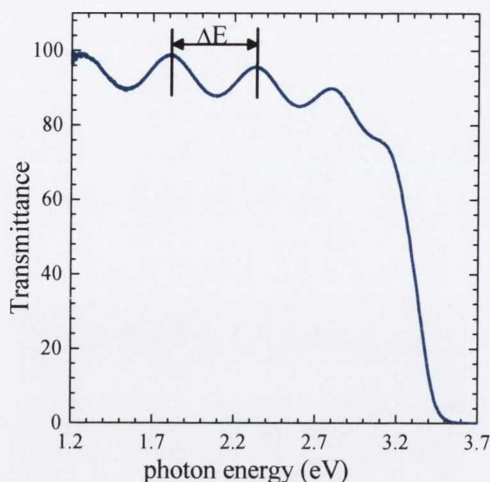

Figure 4.5 An example of Fabry-Perot oscillations for a sample with a thickness of 615 nm.

The relationship between the morphology of the sample and the solvent composition is straightforward. Smooth, good quality layers can be obtained just by using methanol as solvent while the surface roughness rises with increasing water content. The morphology of the film has a direct influence on the optical properties of the coating (Figure 4.2b). Increasing water content leads to a decrease in the transparency of the film. It is worth noting that also the growth rate increases with the water content. This has already been observed in literature in the case of the SnO_2[56]. Nevertheless the above mentioned decrease in transmission is not caused by the thickness of the sample, but it is a consequence of the scattering losses at the rough surface. In order to verify this, samples with a comparable thickness have been grown employing a mixture of 50/50% water/methanol and 100% methanol. For this purpose, the growth time has been shortened to account for the higher growth rate of the water-based solution in comparison with the pure methanol one. Usually the growth time was adjusted to get film thickness in the order of 400-500 nm, however, during these studies, films with thickness value spanning from less than 100 nm up to 1 μm were deposited. For layers of similar thickness, those grown with water are always rougher and hence show a lower transmission. Optical band gap values as determined by linear extrapolation of the transmission data are

found to be unaffected by the choice of solvent and was found to be 3.35 ±0.05 eV.

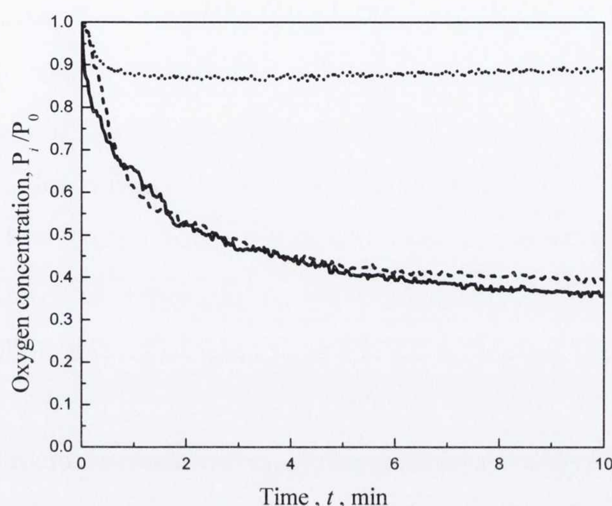

Figure 4.6 Oxygen concentration as a function of time for spraying of water (dotted line), methanol (solid) and a mixture of water/ethanol (30/70, dashed). The significant drop in the case of the organic solvents is caused by the oxygen consumption due to the burning process.

In order to understand the major cause for the roughness, some basic parameters have been monitored during the growth. As stated before, the droplet size and the temperature of the surface play a crucial role for the growth of a good layer. With respect to the particle size, it is easy to understand that solvent with a low density create droplets with lower size, which don't impinge onto the surface. In this case the vaporization of the solvent happens just above the surface leading to a heterogeneous reaction. Therefore, it can be argued that, for this particular type of nozzle, the lower density solvent creates droplets with smaller size and more homogeneous distribution, improving the performance of the process. Nevertheless, this is not the only role played by the solvent. In order to confirm this, three samples were grown using pure water, pure methanol and a mixture ethanol/methanol (70/30). For each sample the oxygen concentration in the pyrolysis chamber has been monitored during the growth. The relative decrease in the oxygen concentration suggests that the solvent burns during the process (Figure 4.6). In fact the oxygen concentration drops down for all

of the three solvents used but, in the case of the organic solvent the decrease is much larger. In the water case the decrease is due to the change in chemical composition of the atmosphere inside the chamber as water vapors replaces air, while for the organic solvent the change is either due to the combustion products (mainly water and CO_2, even if the presence of the co-product cannot be excluded), due to unreacted solvent and due to the oxygen consumption caused by the burning of the solvent. As the solvent burns mostly in the vicinity of the surface, the exothermic burning will provide additional heating to the salt decomposition. In order to confirm this hypothesis, the power supplied by the heater in order to keep its temperature constant, was analyzed. To keep the heater at 423K during the deposition in the case of water, 63 W was needed, while in the case of methanol less power was required (50 W). As the temperature within the heater is a function of cooling power of the sprayed solution and the thermal conductivity of the substrate, these results already show the importance of an active temperature control, as the reduction in surface temperature is partly compensated by the adjustment in heater power, leading to more reproducible surface temperatures. However, even with this active compensation, different solvent have shown different cooling rates which influence, to different extent, the actual surface temperature. To quantify these, a thermocouple has been attached to the glass slide surface and the heater has been set to a constant power value able to keep it at a similar temperature. In this way the effect of the closed loop system has been cancelled. Due to its position, the temperature monitored is relative to the layer of air just above the glass surface (within 1 mm), where the reaction is supposed to happen. The cooling power due to the air stream itself, the water spray and due to two organic solvents has been measured. The data revealed that the temperature above the glass slide is 651 K when the heater reading is 615 K. Due to the cooling caused by the air stream, the glass slide temperature drops down to 591 K. When the water is sprayed, the surface temperature decreases further to 573 K, while for methanol the temperature doesn't vary with respect the value measured for the air stream. In this case no precursor salt has been added to the solvent and therefore the properties measured are related just to the solvent used and hence universally

applicable to any other pyrolysis growth process. It can be seen that the largest drop of surface temperature of ~60 K is caused by the air stream. Absolute values of this decrease are highly dependent on the heat capacity of the heater, and also the air pressure. For piezo-electric nebulizers this drop should be less significant due to the lower gas flow.

Water has shown a greater cooling rate due to its evaporation (18 degrees), while the organic solvent burns, hence compensating the cooling. In fact considering the enthalpy evaporation process for both the solvent ($\Delta_{ev}H(H_2O)$ = 40 kJ/mol, $\Delta_{ev}H(CH_3OH)$ = 35 kJ/mol) and the respective sprayed moles (0.15 for water and 0.067 for methanol), the drop in temperature for methanol should be roughly half of the water one. In other words, assuming a drop in temperature of 18 degrees for water, the expected value for methanol should be 8 degrees. The fact that no temperature drop was observed can be explained if we accept that the methanol burns in the process thus releasing energy. If the heater temperature is controlled by a closed loop system, the drop caused by the air blow or water sprayed is lower compared to the open loop (50 K vs 60 K for air and 15 vs 18 for water). The reason is that the heat loss due to air/water is partially compensated by increased power of the heater. Within the error of our measurement no difference in either oxygen concentration or surface temperature has been found between methanol and ethanol. This can be explained only if the burning of the ethanol is incomplete. In fact the standard enthalpy of combustion of ethanol and the relative oxygen consumption are higher than for methanol. Nevertheless, the calculation of the overall quantity of oxygen inside the chamber shows that this is not enough to completely burn the solvent sprayed.

Although direct temperature measurements have been performed only with pure solvents, our indirect measurements (required heater power and oxygen consumption), carried out during deposition, show that these effects are generically applicable for solutions including different precursor salts. In fact, when the same tests have been repeated for the chloride precursor, higher power consumption and lower oxygen depletion have been observed for water than for the organic solvent. Again, no significant differences in heater power and oxygen concentration between methanol and ethanol

solutions have been observed. The general nature of this behavior can be explained as the low quantity of salt present in the solution (~0.2M) does not significantly alter the solvent burning process. However, absolute values may differ due to different spray rates, temperature or even initial conditions of the growth atmosphere.

To conclude, the higher growth rate observed for water grown films cannot fully explain the difference in the observed roughness of the films. In particular, some of the circular rings characteristic of water grown films, like those clearly visible in Figure 4.9, can only be explained by the difference in the physiochemical properties of the two solvents.

Some of these remarks are due to the use of water in combination with an air blast nozzle, and thus they can be minimized or even completely overcome by using a different type of nozzle. Other results are strictly linked to the physicochemical properties of the solvents and they will not by using different type of nozzle. In particular, smoother samples can be obtained by using water if an ultrasonic nozzle is used rather than an air blast. In order to test this concept, a nebulizer identical to those used for medical treatments, was tested. Visible smoother films could be obtained, however, such a rudimental set-up was immediately abandoned due to the many disadvantages it presents: difficulties in mounting it in the existing spray pyrolysis chamber, no possibility of refilling the solution reservoir and small reservoir capacity, no possibility of direct control of the pressure to the nozzle (which had to be manually controlled), chemical compatibility with only some of the precursors used, and, finally, only small size samples could be deposited. Commercial solution of this type of nozzle are available, however, ultrasonic nozzles are much more expensive and have a narrow range of chemical compatibilities, which make them less suitable for a screening procedure, as it was the final aim of this PhD studies.

4.2.3. Role of the precursors salts

As stated before, smooth, good quality layer can be obtained by using zinc acetate in methanol. In contrast, using zinc chloride led to rough

discontinued layers, either in combination with organic solvents, water or a mixture of them. We relate this to different co-products that are formed during the pyrolytic decomposition of the two different precursors.

If zinc acetate is used, the pyrolytic decomposition leads to the formation of zinc oxide according to the following reaction:

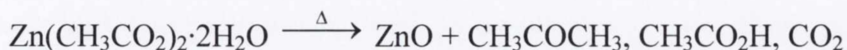

$$Zn(CH_3CO_2)_2{\cdot}2H_2O \xrightarrow{\Delta} ZnO + CH_3COCH_3, CH_3CO_2H, CO_2$$

The thermal decomposition of this precursor has been studied in literature using the thermal gravimetric analysis (TG) coupled to the differential thermal analysis (DTA)[57]. The results show that the organic chain undergoes a series of reactions that ends up with the production of volatile molecule, such as acetone, acetic acid and carbon dioxide), while the zinc ions react with the oxygen present in the atmosphere or in the water to form the correspondent oxide. This is deposited as a thin film onto the glass slide. The chloride decomposition instead, leads to the formation of HCl as co-product according to the following reaction:

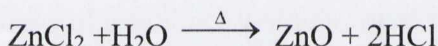

$$ZnCl_2 + H_2O \xrightarrow{\Delta} ZnO + 2HCl$$

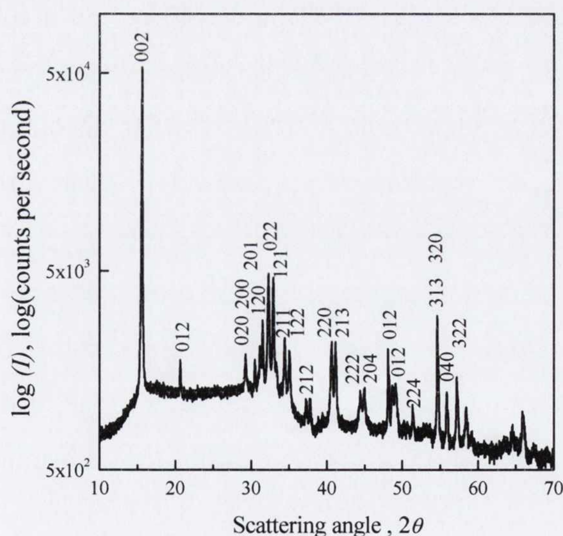

Figure 4.7 XRD patterns of the sample grown by employing a mixture of ethanol/water (70/30) as solvent and zinc chloride as precursor. The peaks are relative to the phase ZnClOH

The poor surface morphology of the films grown using $ZnCl_2$ can thus be attributed to the presence of HCl, which induced a chemical etching of the surface, leading to a rough, not closed film. This explanation is

supported by the detection of the zinc chloride hydroxide phase, (ZnClOH, PDF n 01-072-0525, Figure 4.7) in the sample grown employing a mixture of ethanol-water solution at 623 K. According to the TG-DTA studies reported in literature[58], the decomposition of this oxy-chloride is a complex process that involves different pathways and intermediates, that ends with the formation of the hydrochloric acid and zinc oxide. Therefore it can be concluded that the decomposition of the precursor actually occurs, but, the intimate contact between the acid and the oxide leads to the degradation of the latter one.

The same reason can be advocated to explain the roughness of the film obtained by using zinc nitrate as precursor (PDF-25-1231). In this case the overall reaction is:

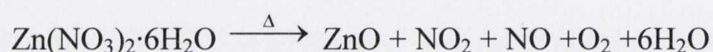

$$Zn(NO_3)_2{\cdot}6H_2O \xrightarrow{\Delta} ZnO + NO_2 + NO + O_2 + 6H_2O$$

Nevertheless, the TG-DTA studies reported in literature[59,60], established that the thermal decomposition of the $Zn(NO_3)_2{\cdot}6H_2O$ is again a complex process, for which different pathways are available. In particular the decomposition of the nitrate fraction can occur directly with the formation of the nitrogen oxides species (NO_2 and NO) or can involve the formation of many different hydroxide species as intermediates, leading to the formation of nitric acid as intermediate and its further decomposition. According to other authors, the decomposition pathway of these species is temperature dependent, and for intermediate values, the formation of HNO_3 has been confirmed. At higher temperatures, the direct decomposition represents the main reaction. So, even if the temperature for the decomposition of this compound has been set in the latter range, it is worth noting that while the precursors are carried towards the substrate, they experience a thermal gradient which may lead to the formation of the corresponding acid. Thus, it can be argued that the same basic explanation carried out to justify the chemical behavior of the chloride precursor, can be extended also to the nitrate one. In other words, the formation of a strong acid as intermediate or final product of the pyrolytic reaction leads to the degradation of the film which thus results in a high roughness. We have shown here, that for ZnO growth this etching process is limiting the quality

of pyrolysis grown films. Although the acid formation is a generic problem when chlorides and nitrates are used, the actual impact for a given oxide can be quite different as it depends on the stability of the oxide with respect to HCl and HNO_3. The etching process can have a significant impact not only to the morphology but also the growth rate itself and even texturing, if there are different etching rates for different crystallographic faces[61].

In order to confirm the general nature of the problem of acid formation for the ZnO growth, a doping study of the films has been done employing different precursors as the cation source. If this is a generic problem, poorer films are expected whenever inorganic salts were used as doping agent. In fact, in the case of significant Mg doping (10%), no closed film can be obtained if chloride salts have been used as zinc and magnesium source, while closed films have been obtained if zinc acetate was used. In this case, doping has been made both with chloride and acetate as magnesium source. Even the relatively small amount of $MgCl_2$ leads already to a degradation of film quality and a higher transparency is obtained for the organic precursor (Figure 4.8a). The rougher sample due to the etching process from HCl formed with the $MgCl_2$ precursor has a lower UV transmission due to the enhanced scattering losses.

The same approach has been adopted for the Al doping. In this case the nitrate, the chloride and an organic precursor have been tested. As in the previous case, when the chloride or nitrate precursors were used, the film was rough and less transparent. If the organic precursor was used, smooth and highly transparent films were obtained (Figure 4.8b).

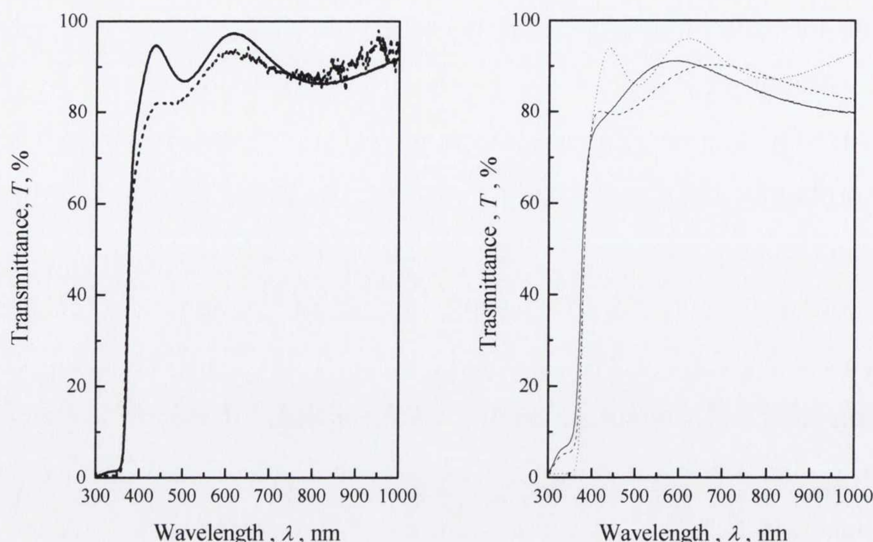

Figure 4.8On the left (a) the specular optical transmission of ZnO:Mg samples grown by using different Mg precursors: (solid curve) magnesium acetate, (dotted) magnesium chloride. On the right (b) the specular transmission for ZnO:Al grown employing aluminium isopropoxide (dotted curve) aluminium nitrate (dashed curve) and aluminium chloride (solid)

Acids formation from inorganic salts in the reactive atmosphere increases surface roughness and hence decreases transmission. However they also have important consequences also on the electrical properties. For this study, Al isopropoxide was later replaced by another organic precursor, Aluminum acetyl acetonate $Al(acac)_3$. This choice was made because, despite of the fact that Al isopropoxide was a good precursor for obtaining good optical properties, however it was difficult to dissolve, making the entire deposition process quite complicated. The effect of different solvents, i.e. water and methanol, on the electrical properties was tested as well by using the same Al salts, $AlCl_3$.

Al precursor (2%)	Solvent	ρ (Ωcm)
$Al(acac)_3$	Methanol	$5\cdot10^{-2}$
$AlCl_3$	Methanol	$1\cdot10^{-1}$
$AlCl_3$	Water	2.5
$Al(NO_3)_3$	Water	4

Table 1 Effect of different precursors and solvent on the electrical properties of ZnO:Al as deposited (without post-annealing treatments).

Different concentrations (0-5%) and different deposition temperatures (653-753K) were screened. The optimum Al concentration for getting the highest conductivity was found to be 1.5-2% and deposition temperatures of 693-723K. Below this range, the grow rate was very poor, while above this range, degradation of the electrical properties was observed. Overall the best electrical properties were found for $Al(acac)_3$ in methanol. Again the solvent showed an effect on the electrical properties as for $AlCl_3$ an increase in the electrical resistivity was observed when water was used as solvent. This was attributed to an increase in the number of grain boundaries. In fact, when cross sectional SEM images (Figure 4.9) are compared, for those grown by using water, smaller grain structures are visible. This is a generalized problem of using water as solvent for the growth of material with the air-blast nozzle.

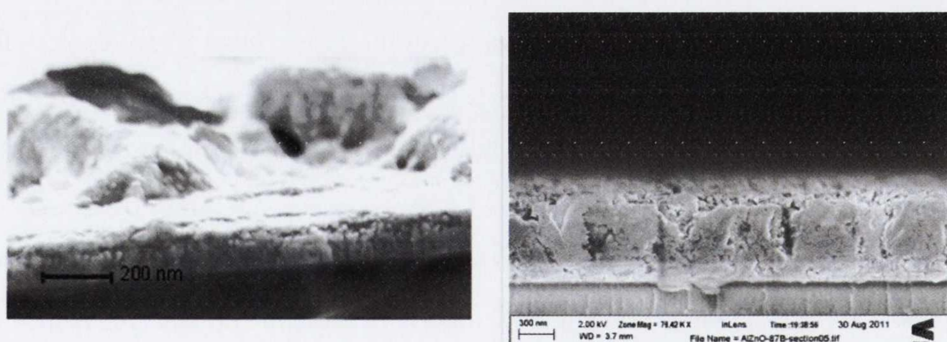

Figure 4.9 SEM cross sections of ZnO:Al sample grown by using water as a solvent(left) or methanol (right). The in-depth view shows the presence of rings due to the evaporation of water droplets which are not present for methanol grown films.

In comparison with respect to chloride precursors, samples grown by using nitride showed a higher resistivity. This was attributed to the suppression of oxygen vacancies due to the formation of oxygen reactive species during the decomposition of the nitrate moiety (Table 1). The resistivities of samples grown by using zinc acetate as Zn precursor and either chloride or acetate as Al precursor as a function of thickness are reported in Figure 4.10 for both as deposited and post-annealed. Resistivity values were calculated after determine both the sheet resistance and the thickness of the sample. For the former, 4 point probes measurements in linear configuration were used. This method, in fact, is quick and non-destructive, does not required patterning of the samples, and since spring loaded contacts were used, does not leave any residue of the material forming the contact itself. This means that a large number of samples can be screened without damaging, leaving them perfectly usable for further characterizations. From the resistivity values, only a small dependence on the film thickness can be noticed. This means that other parameters, such as a good post-annealing treatment or good thermal contact during deposition play a more prominent role with respect to the thickness of the films itself. Hall measurements were performed only on a small set of sample, the reason for this being that the samples needed to be cut in an appropriate size and shape, silver glue was used to make the contact and the back of the samples needed to be glued to the apparatus in order to performed the measurements. After all this processes, samples were most likely useless for any further characterization. Nonetheless, for those samples analyzed, only a small dependence of the Hall mobility and carrier concentration as a function of thickness was observed. Short post annealing treatment in nitrogen atmosphere helped to improve the electrical properties of ZnO:Al. This was performed at 673K and during the treatment the sheet resistance of the sample was monitored in order to stop it as soon as the minimum conductivity was reached. In this way a minimum resistivity $7\times10^{-3}\Omega$cm was obtained. This value is lower than what is normally obtained for ZnO:Al grown by RF sputtering ($1\text{x}10^{-4}\Omega$cm) but comparable with the record for spray pyrolysis grown films $3\text{x}10^{-3}\Omega$cm.[47]

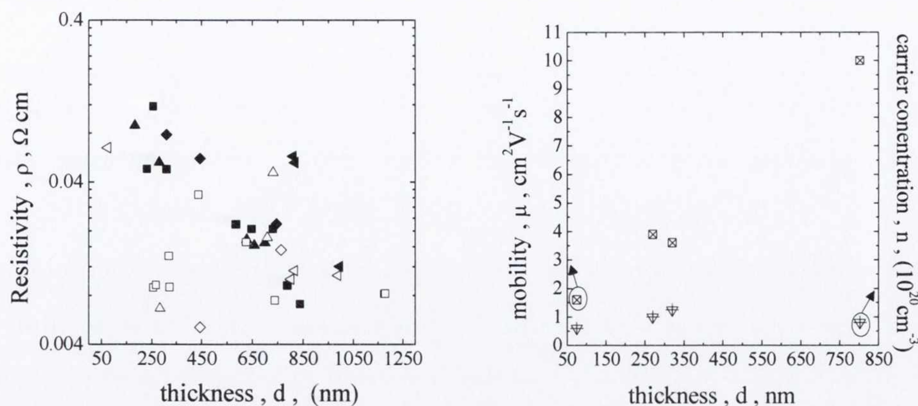

Figure 4.10 On the left: resistivity values for a large set of samples as a function of the layer thickness. Full symbols are for as deposited samples while open symbols are for post-annealed samples. Different shapes are representative of the different Al precursors and Al concentrations used: ◀Chloride (2%), ▲$Al(acac)_3$ (2%), ■$Al(acac)_3$ (1.5%), ♦$Al(acac)_3$(1%). On the right, the mobility and carrier concentration as a function of thickness. All samples are grown by using $Al(acac)_3$ as precursors except for the samples with a thickness of 75 nm for which chloride was used as Al source

4.2.4. Conclusion

A systematic study on the influences of different solvents and precursor salts on the performance of the spray pyrolytic deposited ZnO and ZnO:Al has been presented. In particular the role of the solvent has been correlated to the optical properties of the layers deposited. A correlation between the physical and chemical properties of the solvent, the type of nozzle used and the structural, morphological, optical and electrical properties of the layer has been established. Summarizing, when relative simple air blast nozzles are used, a low density, volatile solvent is required in order to get smaller droplets size and favor the evaporation of the solvent itself. Moreover, the burning of the organic solvent during the deposition has been demonstrated. It has been established that this process can actually compensate the cooling power of the liquid in itself, affecting one of the

most important parameters of the entire process: the actual temperature at which the reaction occurs.

The role of the precursor salt has been systematically investigated with three different types of precursor, namely the nitrate, the chloride and 2 organic one (isopropoxide and acetylacetonate for Al, acetate for Mg and Zn). For all the three cations, the best results have been achieved employing the organic salt. The reason for this can be ascribed to the decomposition of the organic moiety which leads to the formation of volatile, inert products. Instead, the anion moiety decomposition can lead to the formation of strong acids as intermediate or final products, and higher film roughness has been observed. This has been attributed to the chemical etching that these acid species induce. The roughness so created, determines a degradation of the optical properties of the compound. Secondly, the choice of doping precursor salt and solvent can influence the type of carrier responsible for the electrical properties (via the formation of different defect complexes), their concentration (due to differences precursor decomposition rate) and possibly variations in the grain boundary microstructure (different overall morphology).

In order to boost the conductivity, a post-annealing treatment is required. So far, this was performed in nitrogen atmosphere at 700 K for short time. In the future, however, other conditions will be tested: improving the reducing potency of the annealing atmosphere, by using for example pure hydrogen or forming gas, could be beneficial for improving the electrical properties.

4.3. Modification of standard ZnO for usage as internal anti-reflecting layer: introduction

Single absorber thin film solar cells have a rather simple layered structure consisting usually of a front glass substrate, a TCO front contact, the active p-n or p-i-n junction and a metallic back contact. Such simple cell design leads to reflective losses at the interfaces in particular the air/glass, the glass/TCO and the TCO/absorber interface, simply due to refractive index mismatch.

The total loss due to these interfaces has been estimated to be 15-20% at normal incident light, 20-25% at 30° incident light and 30-40% at 60° incident light. For the air/glass interface solutions do exist and are commercially available[62]. They consist of either patterning of the front glass or cover it with a dielectric medium mostly composed by SiO_2 nano-clusters. For solar cells application only the second is meaningful. For the internal interfaces however, solutions have been considered only recently[63].

In simple terms, the advantage of using anti-reflecting coatings in a solar cell is to increase the amount of photons reaching the absorbing layer. In order to do that a material with a suitable refractive index and an appropriate thickness must be chosen. The refractive index of the anti-reflecting layer is related to that of the 2 medium via equation 4.1 for a given wavelength.

$$n_{AR} = \sqrt{n_{glass} n_{TCO}} \qquad 4.1$$

For example, for the glass/TCO interface at 600 nm, n_{glass}~ 1.5 and n_{TCO}~ 1.95. This means that an ideal anti-reflecting layer should have a refractive index of 1.71 at this wavelength.

The refractive index of TCOs is most likely featureless, while those of absorbing materials have strong dispersions. Hence it is unlikely that a real material can act as an anti-reflecting layer on the entire spectral region of interest for the work of a solar cell. However, it can be appropriate to try to

maximize the improvement in the region where the absorber is most efficient, the spectra irradiance of the sun is at maximum and the thermalization loss is at minimum. These three contributions have been included in the calculation performed by Dr. Karsten Fleischer via the so called "weighting function". To this end the thickness and the dielectric function can be tuned in order to bring the maximum of the Fabry-Perot oscillations at those wavelengths where the best compromise for the three above conditions is achieved. The appropriate thickness is chosen by centering one of the maximum in transmission (minimum in reflection) around this optimum wavelength. Since both the rays reflected at the top and at the bottom of the layer will suffer a 180° phase difference with respect to the impinging ray, in order to get a minimum in reflectivity, the path difference between the two reflected rays must be equal to $\lambda/2n$. Since the radius reflected at the bottom of the AR layer travels a distance which is equal to twice of the thickness *d*, it follows that a minimum in reflection occurs when equation 4.2 is satisfied.

$$2d = \lambda / 2n \qquad 4.2$$

In order to estimate the impact of such improvement, Dr. Karsten Fleischer calculated the efficiency gain of a modified solar cell with respect to a standard a-SiH solar cell, taking the values of quantum efficiency and band gap as reported in reference64. The ideal properties of anti-reflecting coating, i.e. thickness and dielectric function, were determined. With the present studies, I attempt to deposit materials suitable to meet such requirements. Some ideal candidates, such as spinel $MgAl_2O_4$, were not suitable for deposition, as the temperature required is above those achievable with the deposition set up used.

The most promising candidate is represented by heavily aluminate zinc oxide. For this purpose the aluminum content was increased beyond what normally used for classical AZO, up to a solution ratio of Al:Zn equals to 70:30.

4.3.1. Characterization of heavily aluminate ZnO to be used as internal anti-reflecting coating.

Samples were grown by spray-pyrolysis using zinc acetate and aluminum acetylacetonate as precursors. The solution concentration was varied from 0.1 up to 0.2 M (total molarity Zn+Al). The aluminum ratio of the hypothetical material $Zn_{1-x}Al_xO_y$ in solution was varied (x=10, 15, 20, 30, 40, 50 and 70). Growth time was varied in order to get different layer thickness for higher accuracy in dielectric function determination. Samples were subjected to structural and optical characterization. In particular UV-Visible spectroscopy and spectroscopy ellipsometry were performed. According to the XRD, the structural properties of ZnO become progressively altered by the presence of increasing quantity of aluminum up to the point when a pseudo-amorphous structure is formed (Figure 4.11).

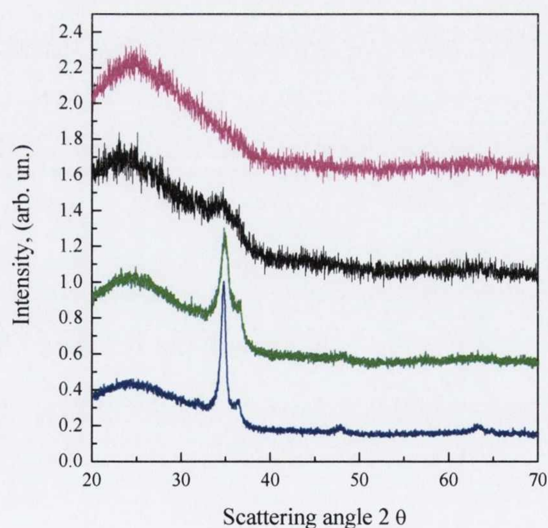

Figure 4.11. XRD patterns of $Zn_{1-x}Al_xO_y$:(—) x=15, (—) x=20, (—)x=30, (—)x=50. As the content of Al increases, the crystallinity of the film decreases.

The dielectric function of the material has been determined by spectroscopic ellipsometry at three different angles of incidence (55°, 60°

and 65°). The ellipsometric data were fitted by Dr. Fleischer by using a 1D bulk critical point as model function, able to take into account the strong excitonic peak, for films with low Al concentration, while for films with high Al concentration a simple oscillator was used to represent the band-gap (Figure 4.12). Overall 5 different parameters were used: the constant dielectric background ε_{∞}, the oscillator strength A, the broadening Γ, the position and the film thickness. Several films with different thickness have been examined. The error bars in the graph are representative of the scattering between the determined dielectric function over several samples. In order to verify the validity of the model, the transmission data were compared as well.

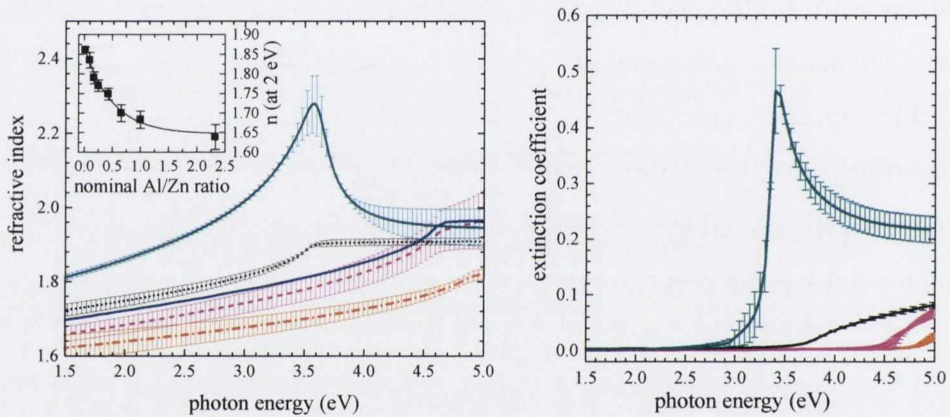

Figure 4.12 Change in the refractive index and extinction coefficient with increasing Al concentration: (—) ZnO, (—)$Zn_{70}Al_{30}O_y$, (—)$Zn_{50}Al_{50}O_y$, (—)$Zn_{70}Al_{30}O_y$. The blue line in the refractive index plot is representative of the refractive index of an ideal anti-reflecting coating.

The UV-visible spectroscopic data and the ellipsometric data show that as the aluminum content is increased, the refractive index lowers down and band-gap opens up Figure 4.12 and Figure 4.13a.

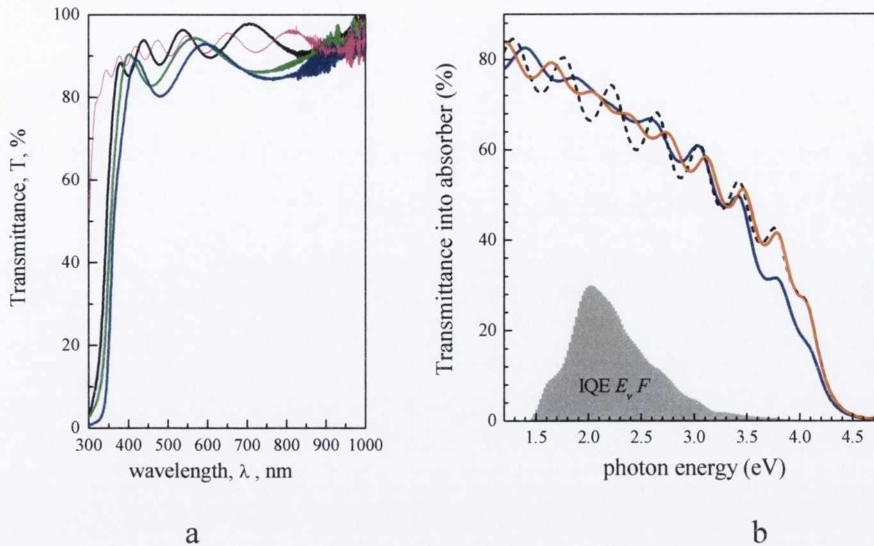

Figure 4.13(a) UV-Visible transmission measurements of $Zn_{1-x}Al_xO_y$ with increasing Al content: (—)x=0.15,(—)x=20,(—)x=30,(—)x=50. It is worth noting that the increase in transmission cannot be attributed to lower thickness. (b) A schematic representation of the way to enhance the efficiency of the cell by using reducing the loss due to reflection: the grey area represents the efficiency of the absorber as calculated by using the weighting function, (– –) transmittance of a glass/TCO stack, (—) transmittance of a glass/ideal AR/TCO stack,(—)glass/real AR/TCO stack.

In Figure 4.13b the method to improve the cell efficiency is schematically represented. In the stack used for the calculation, the thickness oscillations have a minimum right where the absorber efficiency, as calculated via the weighting function, is the highest. By inserting an anti-reflecting coating, that minimum in transmission is converted into a maximum around the region of maximum efficiency and thus an enhancement of 2.3% in the light transmitted into the absorber can be achieved. If the quantum efficiency of the absorber (a-Si:H) is taken into account this translates directly into a relative gain efficiency of 1.9% (for example if the efficiency of the cell is 10%, with the anti-reflecting layer an efficiency of 10.2 % is expected). For the real materials taken into consideration, the optimum was found to be on a ratio Al:Zn of 0.67 ($Zn_{0.6}Al_{0.4}O_y$), for which a relative increase of 1.7% is expected. It is worth noting that the simulated transmittance of such material is quite close to the

ideal case. For lower content of aluminum, the refractive index is too high, while for higher Al content the refractive index is too low.

Next steps will be represented by inserting this material into real solar cells. This will be done under the grant scheme of the Ulysses Project 2012 in collaboration with the University of Nantes.

4.4. Tin oxide and Fluorinated Tin Oxide (FTO)

SnO_2 is an important wide band gap semiconductor and the second most widely use n-type TCOs. It is of great interest in corrosive environmental applications due to its high stability. This includes application such as batteries, low e-windows, gas sensors and solar cells[3].

It crystallizes in a rutile structure where the tin is in an octahedral coordination by means of the 6 oxygen atoms and each oxygen is coordinated by three tin atoms[16]. This structure can be regarded as a hexagonal close packing by the oxygen anions where the cations occupy half of the octahedral holes[16]. The tetragonal unit cell ($P4_2/mnm$) has crystallographic parameters a=4.738 Å and c = 3.188Å[65] (Figure 4.14).

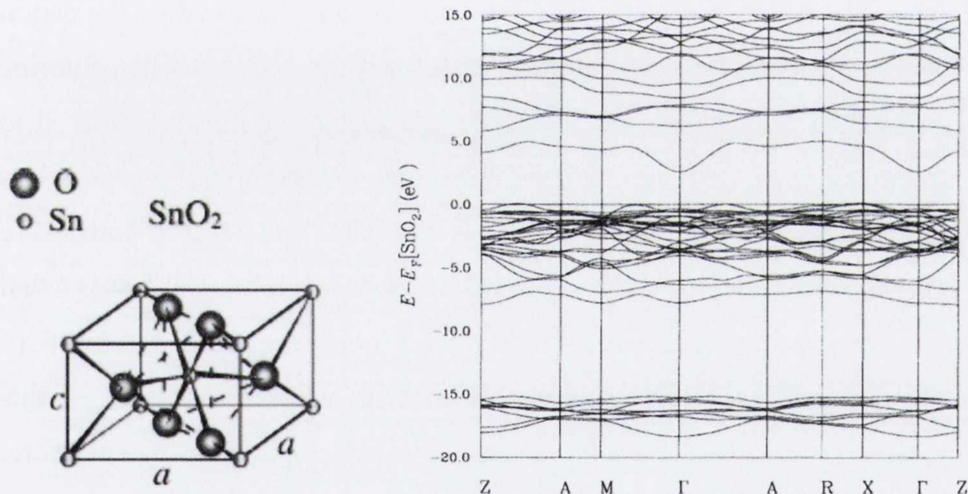

Figure 4.14. Crystal structure and band structure calculation of SnO_2. Taken respectively from 66 and 67.

According to the band structure calculation, direct optical band gap occurs at the Γ point, with an experimental value usually around 3.6-3.9eV[67] (Figure 4.14). The conduction band minimum comes from the highly disperse Sn 5s states giving rise to a high electron mobility. The valence band maximum instead comprises of O 2p states and some Sn 5d, with a low dispersion of the valence band maximum. This explains why SnO_2 is a poor p-type conductor while is a very good n-type conductor[3].

Indeed, tin oxide is a transparent conductive oxide even in its undoped state. The conductivity is most likely attributed to an intrinsic non-stoichiometry, created by the presence of oxygen vacancies (V_o) and interstitial tin (Sn_i) inside the structure, which are easily tolerated due to the multivalence of tin[68,69]. Spontaneous acceptor-like intrinsic defects, like interstitial oxygen or tin vacancies are absent, therefore the electrons released by theV_o or Sn_i are not compensated. However, in order to further improve the conductivity, tin oxide is generally doped, either with Sb or F [70-72] as substitutes for tin and oxygen respectively. Fluorine is normally preferred to antimony because, at high doping concentration, a reduction in the mobility and lower transparency has been observed for Sb doped films[71-73]. The decrease in mobility and conductivity for cation doping with respect to an equivalent anion doping can be explained by taking into consideration that the conduction band in oxides is derived mainly from metal orbital. Thus a strong perturbation in the conduction band is produced by the cation dopant, enhancing the scattering of the electrons. In contrast when fluorine is substituted for oxygen, the electronic perturbation is mostly confined to the filled valence band, and thus the impact on the scattering process is less pronounced[74]. For these reasons FTO is a widely used TCO in both CdTe and amorphous silicon based solar cells[75]. The best commercial FTO (Ashai U-type) shows a transparency of 80% in the visible range and a resistivity of $1.4 \cdot 10^{-5}$ Ωcm[76]. Although extensively used in research laboratories, this product is not yet ready for a large scale industrial application [76]. Therefore, deposition of FTO is still being studied in order to achieve good quality and low cost. To date, most of the production of FTO is done by inexpensive spray-pyrolysis on glass, achieving a good compromise between cost and performance[12]. On a laboratory scale, SnO_2-based films are grown with a wide range of deposition techniques such as sputtering, sol–gel, and various chemical vapor deposition (CVD) techniques [12,77].

It is well known that widespread use of solar cells will only be possible if abundant, non-toxic materials are used and if a fast, inexpensive and scalable technique is available for the deposition. Usage of toxic compound in a production line increases the cost considerable because of the need of additional encapsulation, safety measurements and recycling

plan in order to protect both the workers and the environment[74]. For a long time $CBrF_3$ has been used as F source for CVD. However this is a greenhouse gas which has been gradually phased out from the market[78]. Thus an alternative fluorine source is needed. For this reason either HF or NH_4F have been often reported as F source in spray pyrolysis and other CVD techniques [71,72,79]. However both of them are classified as toxic. For this reason, an attempt to address this issue was made by testing an alternative fluorine source, i.e. benzenesulfonyl fluoride. At the time the experiments were performed, this material was classified as non-toxic. Recently this classification has been modified and nowadays it is classified as toxic, nonetheless it has been proved to effectively act as F-dopant.

4.4.1. An alternative fluorine precursor for the synthesis of FTO: benzenesulfonyl fluoride.

Two different precursors have been used as tin sources (dibutyltin diacetate (DBTDA) and tin chloride pentahydrate ($SnCl_4{\cdot}5H_2O$). Ammonium fluoride (NH_4F) and benzenesulfonyl fluoride (BSF) were used as fluorine source. For both fluorine precursors, different Sn:Fsolution ratios (at.%) were investigated, namely 50:50, 67:37, 80:20, 91:9. The best decomposition temperature was found in range 723-753K.

For DBTDA and $SnCl_4{\cdot}5H_2O$ a 0.1M solution has been prepared using methanol or ethanol as solvent. It was experimentally verified that film quality was not affected by the choice of either one of the two solvents. Methanol is less expensive, however ethanol is not toxic. The deposition temperature was screened over a range spreading from 693K to 773K in steps of 10K for each precursor. The best performing samples have been grown using $SnCl_4{\cdot}5H_2O$ at 753K. When DBTDA was used, the nozzle was allowed to scan laterally in order to improve the homogeneity of the deposition. The scanning amplitude was restricted to ± 0.02 m. Moreover

when $SnCl_4 \cdot 5H_2O$ was used as a Sn source, discontinuous growth provided better samples: in this case, every 2 minutes, the spraying was switched off and the sample was annealed for 2 minutes. However the overall time of spraying, and thus the amount of material used for the deposition, was the same as in the continuous growths. Deposition time was set to 10 minutes. Due to different precursors used as tin source, thickness values range from 500 to 700 nm, with higher growth rate for tin chloride. The thickness of each sample was measured optically after the growth.

Microscope glass slides (Fisher brand, thickness 0.8-1 mm) or cover slips (Roth, thickness 0.17 mm) were used as substrates. The actual composition of each sample was investigated by X-ray photoelectron spectroscopy (XPS). Samples have been cleaned in-situ using 5 min of Ar ion sputtering at 3×10^{-4} Pa, 1.5 kV beam energy and an ion target current of 6μA using an Omicron ISE 5 cold cathode ion sputter source. Experimental data were analyzed using the CasaXPS software.

Optical properties were investigated by UV-Visible spectrophotometry and Tauc plot was used to determine the band gap. Spectroscopic ellipsometry (SE) was used to determine the thickness of the samples. Data were collected in the energy range from 1.5 to 5 eV, at three different angles of incidence (55°, 60°, 65°). Multiple angle measurements are required in order to decouple the correlation between the refractive index (n) and the thickness of the sample (*d*). Experimental data were fitted by Dr. Karsten Fleischer, using a multilayer model consisting of air, a rough surface area, the thin film and glass. The line-shape of the dielectric function of the film was reconstructed using a three dimensional critical point[80]. The parameters associated with it (amplitude of the critical point, the threshold energy, the broadening and the excitonic phase angle) as well as the thickness of the sample were introduced as variables, whose values were optimized via an iterative fitting procedure with respect to the raw ellipsometric data at multiple angles. To further confirm the validity of the data acquired in this way, transmission measurements were analyzed, using database refractive indices for FTO. The thickness values determined via the ellipsometric model and via spectrophotometry coincide within the experimental error of ±20 nm

Electrical properties were investigated in standard 4 point probe square geometry. Due to the previously mentioned differences in the growth rates for different precursors, film thickness varied between samples. Therefore resistivity values will be determined using the optically determined thickness value of each sample. Selected samples were also subjected to Hall measurements in order to determine both mobility and bulk carrier density. Colloidal silver paint was used to provide ohmic contacts. The same system was used to investigate the dependence of the sheet resistance on temperature in a range from 70 to 300 K, allowing the determination of the activation energy for the carriers. For completeness, all the optical and electrical properties of in house grown samples were compared to those of 2 reference samples: a commercial sample obtained from Solaronix (REF-1) and a spray pyrolysis sample grown independently by another group (REF-2)

4.4.2. Results and Discussion

Optical properties of undoped and fluorine-doped tin oxide were investigated by spectroscopic ellipsometry and UV-Visible transmission data. The best films were obtained at high temperature (723K) only if good thermal contact was achieved between the sample and the heating elements. For undoped tin oxide low temperature (around 653K) lead to brown discoloration on the glass slide, with lower transparency and lower band gap (3.70 eV for samples grown at 653 K versus 3.8 eV for those grown at 723K) (Figure 4.15)

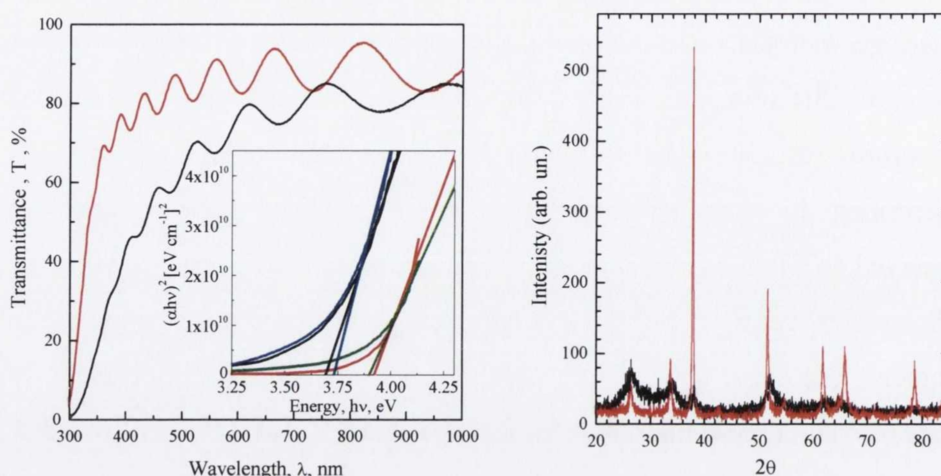

Figure 4.15 UV-visible transmission measurements and XRD patters of SnO_2samples as a function of temperature and precursors: (—) DBTDA and 753K, (—) DBTDA and 653K. In the inset the band gap was determined via a Tauc plot: (—) $SnCl_4$ and 753K, (—) DBTDA and 753K.

Even at high temperature, good thermal contact was required to obtain good quality films. For example, the build-up of material as a result of several depositions leads to worse thermal contact. As a consequence inhomogeneity within the same glass slide arose with the appearance of brown discoloration on the region with poor thermal contact. Moreover differences in specular transmission could be found even for samples grown using the same fluorine source, due to different scattering loss (haze). Haze turns out to be caused by the roughness at the surface, whose value depends on both the precursor used as tin source and deposition temperature. In particular chloride introduces more roughness with respect to DBTDA. These problems were lately overcome by depositing on cover slips rather than glass slides. Tauc plot was used to determine the band gap values over a large range of samples. A large deviation was found for virtually identical deposition conditions. This is mainly due temperature fluctuation during the deposition.

For FTO, the commercial sample (REF-1), the sample provided by an independent group (REF-2) and in-house grown samples were analysed by SE and UV-Visible spectroscopy. In the first set of samples, NH_4F was used as fluorine source and either $SnCl_4$ or DBTDA as tin source. The line-shape of the dielectric function was found to be consistent for all the samples

analysed, in other words, no difference was found in the dielectric function of REF-1 and REF-2 samples with respect to those grown in-house, and neither between the samples grown by using chloride with respect to those grown by using DBTDA. Band gap values were determined as the onset position of the 3D bulk critical point. For all fluorine doped films, values were consistently higher than those determined for the undoped SnO_2. This was attributed to the Bursten-Moss effect, which however was more pronounced for the sample REF-1 (a commercial sample, Eg = 4.3± 0.1) than for the NH_4F samples (4.0 ± 0.06). These values are systematically slightly higher than those estimated by the Tauc (3.8±0.1 for the NH_4F samples, 3.9 ±0.1 for REF 1) by 0.2-0.3 eV. Despite the consistent overestimation of SE determined band gaps over a large set of samples, the trend has always been consistent and therefore, for the second set of samples grown by using BSF as fluorine source and, again, either the chloride or the DBTDA as tin source, band gap values were determined by the Tauc plot method.

Best performing FTO films were obtained at a deposition temperature higher than 673K. At lower temperature (below 673K) no improvement in the electrical properties was observed leading to the conclusion that either the fluorine precursors do not decompose at this temperature or that fluorine is not actively incorporated. Best room temperature resistivities for samples grown using NH_4F as fluorine source were found to be $1.4 \cdot 10^{-3}$ Ωcm and $1.6 \cdot 10^{-3}$ Ωcm with $SnCl_4 \cdot 5H_2O$ and DBTDA as Sn precursor respectively. These values are below those of REF-1 ($5 \cdot 10^{-4}$ Ωcm) and REF-2 ($6 \cdot 10^{-4}$ Ωcm) but in accordance to other spray pyrolysis grown FTO films [81,82].

In the main experiment, the alternative fluorine source (BSF) was tested. In this case a screening of different temperature and ratio Sn:F has been carried out, but, again, only representative samples will be presented. Taking into consideration the resistivity, the best condition for the deposition was found to be 753K with a Sn:F ratio of 50:50. In this condition a minimum resistivity of 4.3 10^{-3} Ωcm has been found using $SnCl_4 \cdot 5H_2O$ as tin source. Compared to the undoped sample grown under the same conditions, this corresponds to an improvement of 50% in the conductance.

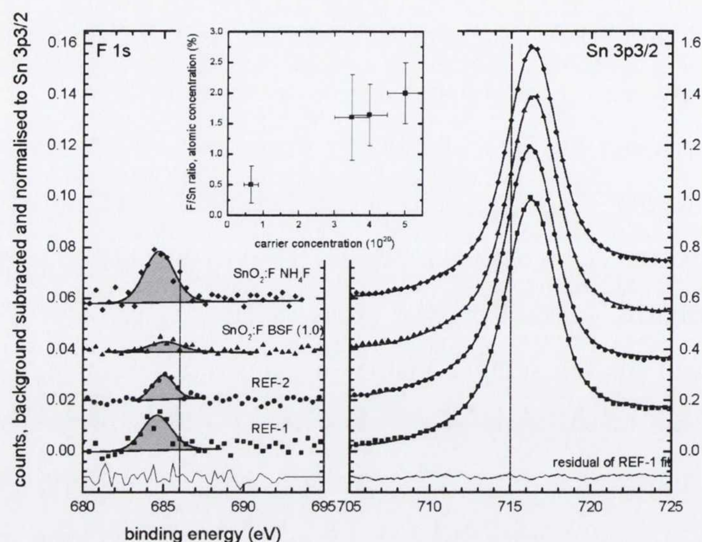

Figure 4.16 XPS spectra of fluorinated tin oxide samples. On the left the F 1s peak is shown, while on the right the Sn 3p3/2. For the fluorine peak the background has been subtracted and the intensity has been normalized to the Sn3p3/2 peak. The inset shows the correlation between the measured carrier concentration and the F/Sn ratio derived from the XPS analysis.

The actual incorporation of fluorine was confirmed by XPS. As shown in Figure 4.16, for all samples it is possible to identify the F 1s peak at the characteristic binding energy around 685 eV [83].

At this time no quantitative analysis of the F incorporation is possible for various reasons. Due to the surface sensitivity of the XPS measurements the presence of F in as-grown samples is not a sufficient indication of fluorine incorporation. There is the possibility that the surface is contaminated by precursor solution residue, which contains fluorine. Therefore Argon ion sputtering of 1.5kV Ar ions for 5 min has been employed to remove residual carbon and other potential contaminants from the precursor solution.

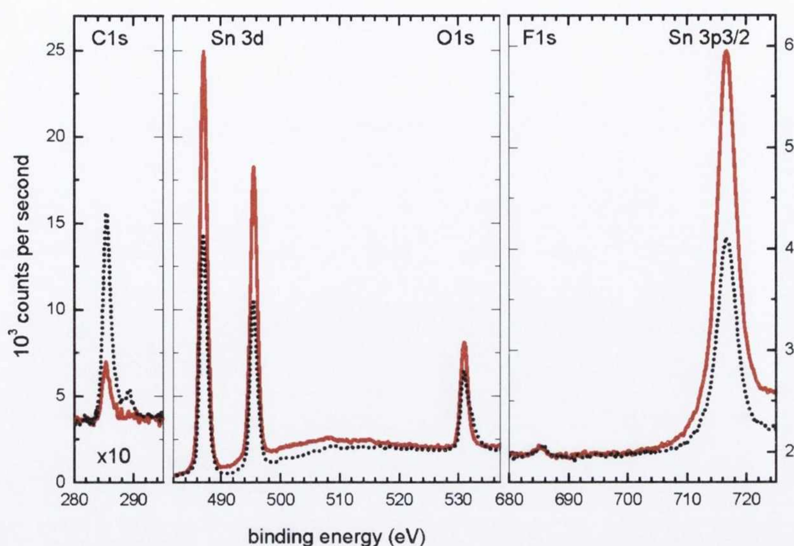

Figure 4.17 XPS spectra of sample REF-1 showing the effect of Ar cleaning: (black dot) the sample before cleaning, (red line) the sample after cleaning.

Unfortunately the Ar sputtering treatment changes the surface composition and roughness as lighter elements such as O and F are preferentially removed. Figure 4.17 shows the effect of the cleaning cycles on the relative intensities of the Sn 3d, O 1s and F 1s core levels for sample REF-1 with the highest F concentration and lowest initial carbon contamination of all investigated samples. It is evident, that the cleaning does change the measured Sn/F and Sn/O ratios indicating a change in the stoichiometry of the surface area of the oxide, or the removal of precursor residuals. Nevertheless after sputtering the presence of F has been confirmed for both fluorine precursors and measured Sn/F ratios scale with the carrier concentration of the samples (inset Figure 4.16). This indicates that the measured fluorine after sputtering originates from incorporated fluorine, even if the measured absolute values of the F/Sn ratios are not indicative of the real fluorine content in the SnO_2 matrix. It is also worth noting, that measurement times were limited, as extensive exposure of all samples to the Al Kα-rays (>1h) lead to a steady decline in the detected fluorine signal.

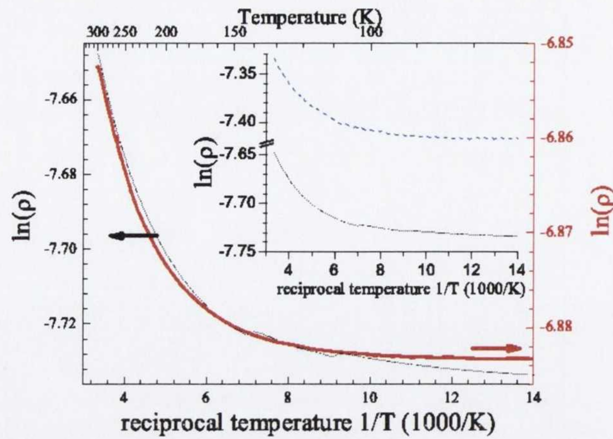

Figure 4.18Arrhenius plot of the resistivity versus reciprocal temperature for samples showing a typical metallic behaviour: (red line) FTO deposited by using NH_4F, (black dot) REF-1, (blue dashed) REF-2. As the resistivity of the FTO-NH_4F is higher, different range of scale are used.

Resistance measurement have been carried out over a set of samples grown under the same conditions but with different nominal Sn:F ratio. While all the other samples show a characteristic metallic behavior in the resistance vs. temperature plot, the samples grown using BSF show a metallic behavior at high temperature while at lower temperatures the resistance increases again, as expected for semiconductors (Figure 4.18 and Figure 4.19). This suggests that more than one type of carrier contributes to the overall conductance and there is still a large contribution of these intrinsic carriers to the measured total conductance. The temperature, at which this transition occurs (here defined as a change in slope), is a function of BSF concentration (Figure 4.19). When the nominal atomic ratio Sn:F is 1, incorporation is good enough to lead to a metallic behavior almost in the whole range of temperatures. As the nominal concentration of fluorine decreases, the transition temperature shifts to higher values.

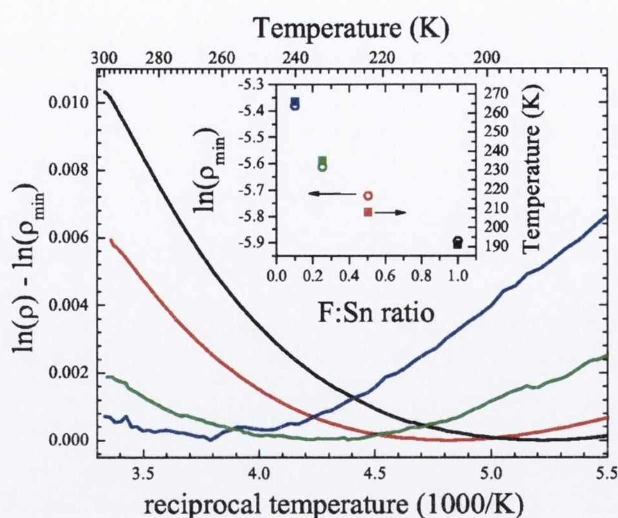

Figure 4.19 Resistivity vs reciprocal temperature for a set of samples grown using BSF as fluorine source and varying Sn:F ratio in solution: (— 91:9, — 80:20, — 67:33, — 50:50). An offset equal to $ln(\rho_{min})$ was subtracted to emphasize the change from a behaviour dominated by the metal like carriers to a semiconducting one. The inset shows the dependence of the temperature of transition from metallic to semiconductor behaviour (■) and absolute resistivity (○) on the nominal F:Sn ratios.

Samples grown using the alternative precursors show a lower carrier concentration compared to all the other samples. However, the mobility of the carriers is comparable to those found for REF-1 and REF-2 and it is much higher than in samples grown using NH_4F as precursor (Table 2). At present it is not clear, whether the lower carrier concentration in BSF grown films is related to a lower efficiency in the decomposition process of BSF itself or if this is due to a lower incorporation rate of the fluorine atoms or alternative fluorine could be partly passivated by compensating defects introduced by C, S, or H also present in the precursor. However as the measured fluorine concentration scales well with measured carrier concentration (inset Figure 4.16), a lower incorporation rate is more likely.

Several scattering mechanisms might influence the mobility of the carriers [72,73,84] as reported in section 2.1. It is worth noting that all equations (Eq. 2.12 - 2.17) are valid under the assumption that a single type of carrier is present. This is not the case for the fluorinated tin oxide. In fact, as previously reported, the undoped samples are already conductive and therefore more than one type of defects can be the source of conductivity in

doped samples. For this reason only the temperature dependence of the Hall mobility will be considered in order to define the mechanism.

Sample	carrier concentration (cm^{-3})	Hall mobility ($cm^2V^{-1}s^{-1}$)	Growth temperature (K)	Sn precursor
SnO_2:F BSF (0.5)	$5(\pm1)\cdot10^{+19}$	28 ± 3	753	$SnCl_4$
SnO_2:F BSF (1.0)	$6.6(\pm1)\cdot10^{+19}$	31 ± 3	753	$SnCl_4$
SnO_2:F NH_4F	$4(\pm1)\cdot10^{+20}$	12 ± 3	753	$SnCl_4$
REF-2	$3.5 \pm (0.5)\cdot10^{+20}$	32 ± 2		
REF-1	$5(\pm1)\cdot10^{+20}$	30 ± 3		

Table 2 Room temperature electrical properties and growth condition for representative samples used for XPS analysis.

For samples grown using BSF, REF-1 and REF-2 samples, the principal scattering mechanism is due to acoustical phonons in the temperature range of 300-150K and ionized impurities for temperature lower than 150K. This conclusion has been drawn by taking into consideration the dependence of the mobility as a function of temperature (Figure 4.20).

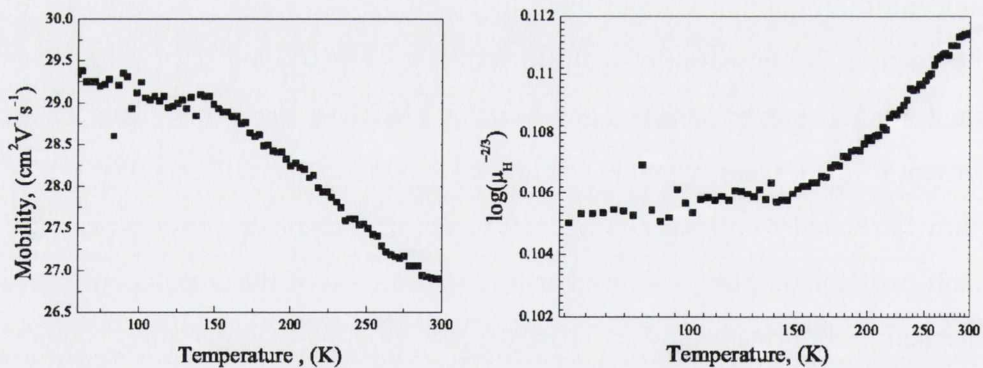

Figure 4.20 On the right:an example of Hall mobility vs temperature data for REF-1. The line shape of the curve is representative for all samples investigated, although absolute values vary. On the left: power dependence of the mobility values upon temperature shows that in the range between 300 and 150 K, the mobility $\mu^{-2/3}$ varies linearly with temperature. Below 150 K mobility becomes independent of temperature.

A linear dependence of mobility vs. $T^{-3/2}$ is present down to a temperature of 200K (Figure 4.20, equation (2.15)). Therefore it can be argued that the principal scattering mechanism in this temperature range is

due to phonons. From 200 K to 70K, the mobility becomes independent of the temperature, meaning that phonons are frozen in and ionized impurities represent the principle scattering mechanism in this region (Figure 4.20, equation (2.12)). Either way, both mechanisms are intrinsic to the material itself and cannot be suppressed. This means that the only way to improve the material conductivity is by increasing the carrier concentration. Samples grown employing NH_4F show a much lower mobility compared to BSF grown samples but the overall shape of the curve is consistent with the previous picture (see also Table 2). This means that again phonons play an important role up to 200 K while below this temperature, ionized impurities become relevant. In this case, in order to account for the lower mobility, other mechanisms such as grain boundary or scattering at crystallographic defects have to be considered.

4.4.3. Conclusion

An alternative precursor has been tested as fluorine source for the synthesis of SnO_2:F by spray pyrolysis. Its performance has been compared to a commonly used source, NH_4F, to a commercial sample and to a sample grown by spray pyrolysis by an independent group. Incorporation of fluorine has been indirectly shown by the improvement in conductivity and directly by identification of the fluorine 1s core level in XPS measurements.

Tin oxide produced using BSF has higher resistivity than those obtained by using NH_4F. The reason for this is likely to be a lower decomposition or incorporation efficiency of BSF which results in a lower carrier concentration in the samples. Instead, the Hall mobility of samples using BSF is comparable to those of the commercial and independent laboratory samples, indicating that the typical low mobility found for spray pyrolysis grown, untreated FTO is caused by the use of NH_4F, and not the deposition technique itself. For all investigated FTO samples phonon scattering represents the principal scattering mechanism in the region between 300 K and 200 K, while at lower temperature, scattering by ionized impurities dominates. When NH_4F was used, instead, scattering due to grain

boundaries and crystallographic defects also contributes to limiting the mobility.

The two samples used as reference show better electrical properties (R_{sh}=8-10 Ω/□) than those grown in house (minimum R_{sh}=30-40 Ω/□) while comparable optical properties could be achieved. Several reason could be responsible for these, in particular the large droplet distribution and a severe cooling of the surface due to the type of nozzle used, a nozzle to substrate distance too short, purity of the salt. Therefore the limit of the present setup are acknowledge, in light of the fact that the setup was built with the aim of allowing easy and fast screening of materials rather than high performance materials. However it was crucial to evaluate the upper limit of the performance achievable with it in order to properly assess the quality of the new materials produced, as will be illustrated in the following chapter.

(1) Toshio Kamiya, M. K. *MRS Bulletin* **2008**, *33*, 1061-1066.

(2) Chen, M.; Pei, Z. L.; Wang, X.; Yu, Y. H.; Liu, X. H.; Sun, C.; Wen, L. S. *Journal of Physics D: Applied Physics* **2000**, *33*, 2538-2548.

(3) D. Ginley, H. H., D.C. Paine *Handbook of transparent conductors*; Springer: New York, 2010.

(4) Bellingham, J. R.; Phillips, W. A.; Adkins, C. J. *Journal of Materials Science Letters* **1992**, *11*, 263-265.

(5) Ginley, D. S.; Bright, C. *MRS bulletin* **2000**, *25*, 15-18.

(6) Ginley, D.; Coutts, T.; Perkins, J.; Young, D.; Li, X.; Parilla, P.; Stauber, R.; Readey, D.; Duncan, C. *MRS symposium proceedings* **2001**, *668*, H2.7.1-H2.7.15.

(7) A. J. Freeman, K. R. P., T. O. Mason, R. P. H. Chang and T. J. Marks *MRS Bulletin* **2000**, *25*, 45-51.

(8) Minami, T. *MRS bulletin* **2000**, *25*, 38-44

(9) Ozgur, U.; Alivov, Y. I.; Liu, C.; Teke, A.; Reshchikov, M. A.; Dogan, S.; Avrutin, V.; Cho, S. J.; Morkoc, H. *Journal of Applied Physics* **2005**, *98*, 041301-103.

(10) Ellmer, K. *Journal of Physics D: Applied Physics* **2001**, *34*, 3097.

(11) Lany, S.; Zunger, A. *Physical Review Letters* **2007**, *98*, 045501.

(12) Antonio Facchinetti, T. J. M. *Transparent electronics From synthesis to application*; Wiley, 2010.

(13) T.J. Coutts, J. D. P., D.S. Ginley, T.O. Mason In *195th Meeting of the Electrochemical Society* Seattle, Washington, 1999.

(14) Matsubara, K.; Tampo, H.; Shibata, H.; Yamada, A.; Fons, P.; Iwata, K.; Niki, S. *Applied Physics Letters* **2004**, *85*, 1374-1376.

(15) Lu, J. G.; Fujita, S.; Kawaharamura, T.; Nishinaka, H.; Kamada, Y.; Ohshima, T. *Applied Physics Letters* **2006**, *89*, 262107.

(16) Hoel, C. A.; Mason, T. O.; Gaillard, J.-F. o.; Poeppelmeier, K. R. *Chemistry of Materials* **2010**, *22*, 3569-3579.

(17) Cui, J.; Wang, A.; Edleman, N. L.; Ni, J.; Lee, P.; Armstrong, N. R.; Marks, T. J. *Advanced Materials* **2001**, *13*, 1476-1480.

(18) Minami, T.; Miyata, T.; Yamamoto, T. *Surface and Coatings Technology* **1998**, *108-109*, 583-587.

(19) Fleischer, K.; Arca, E.; Shvets, I. V. In *Proceedings of 25th European Photovoltaic Solar Energy Conference* Valencia, 2010, p 389.

(20) Minami, T. *Semiconductor Science and Technology* **2005**, *20*, S35-S44.

(21) Szyszka, B.; Sittinger, V.; Jiang, X.; Hong, R. J.; Werner, W.; Pflug, A.; Ruske, M.; Lopp, A. *Thin Solid Films* **2003**, *442*, 179-183.

(22) Gupta, A.; Compaan, A. D. *Applied Physics Letters* **2004**, *85*, 684-686.

(23) Perrenoud, J.; Kranz, L.; Buecheler, S.; Pianezzi, F.; Tiwari, A. N. *Thin Solid Films* **2011**, *519*, 7444-7448.

(24) Jiang, X.; Wong, F. L.; Fung, M. K.; Lee, S. T. *Applied Physics Letters* **2003**, *83*, 1875-1877.

(25) Hosono, H.; Kamiya, T.; Hirano, M. *Bulletin of the Chemical Society of Japan* **2006**, *79*, 1-24.

(26) Klaus Ellmer, A. K., Bernd Rech *Transparent Conductive Zinc Oxide: Basics and Applications in Thin Film Solar Cells* Springer 2010.

(27) Anderson, J.; Chris, G. V. d. W. *Reports on Progress in Physics* **2009**, *72*, 126501.

(28) McCluskey, M. D.; Jokela, S. J. *Journal of Applied Physics* **2009**, *106*, 071101-13.

(29) Norton, D. P.; Heo, Y. W.; Ivill, M. P.; Ip, K.; Pearton, S. J.; Chisholm, M. F.; Steiner, T. *Materials Today* **2004**, *7*, 34-40.

(30) Look, D. C.; Claflin, B.; Alivov, Y. I.; Park, S. J. *physica status solidi (a)* **2004**, *201*, 2203-2212.

(31) Pearton, S. J.; Norton, D. P.; Ip, K.; Heo, Y. W.; Steiner, T. *Progress in Materials Science* **2005**, *50*, 293-340.

(32) Abrahams, S. C.; Bernstein, J. L. *Acta Crystallographica Section B* **1969**, *25*, 1233-1236.

(33) Look, D. C.; Hemsky, J. W.; Sizelove, J. R. *Physical Review Letters* **1999**, *82*, 2552-2555.

(34) Anderson, J.; Chris, G. V. d. W. *Applied Physics Letters* **2005**, *87*, 122102.

(35) Harrison, S. E. *Physical Review* **1954**, *93*, 52-62.

(36) Van de Walle, C. G. *Physical Review Letters* **2000**, *85*, 1012-1015.

(37) Ruske, F.; Sittinger, V.; Werner, W.; Szyszka, B.; van Osten, K. U.; Dietrich, K.; Rix, R. *Surface and Coatings Technology* **2005**, *200*, 236-240.

(38) Look, D. C.; Farlow, G. C.; Reunchan, P.; Limpijumnong, S.; Zhang, S. B.; Nordlund, K. *Physical Review Letters* **2005**, *95*, 225502.

(39) Lyons, J. L.; Janotti, A.; Van de Walle, C. G. *Applied Physics Letters* **2009**, *95*, 252105-3.

(40) Yamamoto, T.; Katayama-Yoshida, H. *Journal of Crystal Growth* **2000**, *214*, 552-555.

(41) Bian, J. M.; Li, X. M.; Gao, X. D.; Yu, W. D.; Chen, L. D. *Applied Physics Letters* **2004**, *84*, 541-543.

(42) Bian, J. M.; Li, X. M.; Zhang, C. Y.; Yu, W. D.; Gao, X. D. *Applied Physics Letters* **2004**, *85*, 4070-4072.

(43) Barnes, T. M.; Olson, K.; Wolden, C. A. *Applied Physics Letters* **2005**, *86*, 112112-3.

(44) Look, D. C.; Claflin, B. *physica status solidi (b)* **2004**, *241*, 624-630.

(45) Sans, J. A.; Sanchez-Royo, J. F.; Segura, A.; Tobias, G.; Canadell, E. *Physical Review B* **2009**, *79*, 195105.

(46) Singh, A. V.; Mehra, R. M.; Buthrath, N.; Wakahara, A.; Yoshida, A. *Journal of Applied Physics* **2001**, *90*, 5661-5665.

(47) Crossay, A.; Buecheler, S.; Kranz, L.; Perrenoud, J.; Fella, C. M.; Romanyuk, Y. E.; Tiwari, A. N. *Solar Energy Materials and Solar Cells* **2012**.

(48) Zhang, X.; Li, X. M.; Chen, T. L.; Zhang, C. Y.; Yu, W. D. *Applied Physics Letters* **2005**, *87*, 092101-3.

(49) Zhang, X.; Li, X. M.; Chen, T. L.; Bian, J. M.; Zhang, C. Y. *Thin Solid Films* **2005**, *492*, 248-252.

(50) Yoshino, K.; Oyama, S.; Yoneta, M. *Journal of Materials Science: Materials in Electronics* **2008**, *19*, 203-209.

(51) De Merchant, J.; Cocivera, M. *Chemistry of Materials* **1995**, *7*, 1742-1749.

(52) Lee, J.-H.; Park, B.-O. *Materials Science and Engineering: B* **2004**, *106*, 242-245.

(53) Mohammad, M. T.; Hashim, A. A.; Al-Maamory, M. H. *Materials Chemistry and Physics* **2006**, *99*, 382-387.

(54) Seeber, W. T.; Abou-Helal, M. O.; Barth, S.; Beil, D.; Hoche, T.; Afify, H. H.; Demian, S. E. *Materials Science in Semiconductor Processing* **1999**, *2*, 45-55.

(55) Hu, J.; Gordon, R. G. *Journal of Applied Physics* **1992**, *71*, 880-890.

(56) Vasu, V.; Subrahmanyam, A. *Thin Solid Films* **1990**, *193-194, Part 2*, 973-980.

(57) Lin, C.-C.; Li, Y.-Y. *Materials Chemistry and Physics* **2009**, *113*, 334-337.

(58) Garcia-Martinez, O.; Vila, E.; Vidales, J. L. M. d.; Rojas, R. M.; Petrov, K. *Journal of Materials Science* **1994**, *29*, 5429-5434.

(59) Maneva, M.; Petrov, N. *Journal of Thermal Analysis and Calorimetry* **1989**, *35*, 2297-2303.

(60) Biswick, T.; Jones, W.; Pacula, A.; Serwicka, E.; Podobinski, J. *Journal of Solid State Chemistry* **2007**, *180*, 1171-1179.

(61) Smith, A. s.; Rodriguez-Clemente, R. *Thin Solid Films* **1999**, *345*, 192-196.

(62) Kursawe, M.; Anselmann, R.; Hilarius, V.; Pfaff, G. *Journal of Sol-Gel Science and Technology* **2005**, *33*, 71-74.

(63) S. Klein, S. W., S. Buschbaum, K. Schwanitz, T. Stolley, D. Severin, P. Obermeyer, M. Kress, E. Sommer, T. Marschner, M. Martini, S. Noll-Baumann, J. Haack, U. Schmidt, A. Straub, K. Ahmed, K. Schuegraf In *25th European Photovoltaic Solar Energy Conference* 2010, p 2708–2712.

(64) Liu, H.; Jiao, L.; Semoushkina, S.; Wronski, C. R. *Journal of Non-Crystalline Solids* **1996**, *198, Part 2*, 1168-1171.

(65) Baur, W. H.; Khan, A. A. *Acta Crystallographica Section B* **1971**, *27*, 2133-2139.

(66) Meyer, M.; Onida, G.; Palummo, M.; Reining, L. *Physical Review B* **2001**, *64*, 045119.

(67) Mishra, K. C.; Johnson, K. H.; Schmidt, P. C. *Physical Review B* **1995**, *51*, 13972-13976.

(68) Singh, A. K.; Janotti, A.; Scheffler, M.; Van de Walle, C. G. *Physical Review Letters* **2008**, *101*, 55502.

(69) Kilic, C.; Zunger, A. *Physical Review Letters* **2002**, *88*, 095501.

(70) Sun, J.; Lu, A. X.; Wang, L. P.; Hu, Y.; Wan, Q. *Nanotechnology* **2009**, *20*, 335204.

(71) Elangovan, E.; Singh, M. P.; Ramamurthi, K. *Materials Science and Engineering B-Solid State Materials for Advanced Technology* **2004**, *113*, 143-148.

(72) Ramaiah, K. S.; Raja, V. S. *Applied Surface Science* **2006**, *253*, 1451-1458.

(73) Thangaraju, B. *Thin Solid Films* **2002**, *402*, 71-78.

(74) Gordon, R. G. *MRS bulletin* **2000**, *25*, 52-57.

(75) Sheel, D. W.; Yates, H. M.; Evans, P.; Dagkaldiran, U.; Gordijn, A.; Finger, F.; Remes, Z.; Vanecek, M. *Thin Solid Films* **2009**, *517*, 3061-3065.

(76) Loffler, J. PhD Universiteit Utrecht, 2005.

(77) Granqvist, C. G. *Solar Energy Materials and Solar Cells* **2007**, *91*, 1529-1598.

(78) Xiaonan Li, M. B., Joel Pankow, Sally E. Asher, Helio Moutinho, and; Gessert, T. *Mater. Res. Soc. Symp. Proc* **2007**, *1012*.

(79) Zhou, Z. B.; Cui, R. Q.; Hadi, G. M.; Li, W. Y.; Ding, Z. M. *Journal of Materials Science-Materials in Electronics* **2001**, *12*, 417-421.

(80) Lautenschlager, P.; Garriga, M.; Cardona, M. *Physical Review B* **1987**, *36*, 4813-4820.

(81) Martinez, A. I.; Huerta, L.; de Leon, J. M. O. R.; Acosta, D.; Malik, O.; Aguilar, M. *Journal of Physics D-Applied Physics* **2006**, *39*, 5091-5096.

(82) Oshima, M.; Yoshino, K. *Journal of Electronic Materials* **2010**, *39*, 819-822.

(83) Briggs, D. *Handbook of X-ray and ultraviolet photoelectron spectroscopy*; Heyden: London, 1977.

(84) Elangovan, E.; Singh, M. P.; Ramamurthi, K. *Materials Science and Engineering B-Solid State Materials for Advanced Technology* **2004**, *113*, 143.

Chapter 5

p-type TCOs

5.1. p-type TCOs: state of the art

The very first p-type transparent semiconducting oxide was NiO, reported in 1993 by Sato[1]. However, it was only in 1997, when a systematic paradigm to deposit p-type TCOs was presented by Kawazoe and co-workers. They introduced the concept of modifying the valence band of oxides to achieve simultaneous p-type conductivity and transparency, proving, indeed, this concept by depositing a thin film of $CuAlO_2$[2]. Since then, other p-type TCOs have been deposited, nonetheless their performance is too poor for any possible implementation into commercial devices. However interest in these materials is quite high, since a substantial improvement on their properties can open up the possibility fornext generation fully transparent electronic devices.

Challenges for improving p-type transparent materials are rather different than those for n-type. p-type TCOs can be realized by introducing dopants or defect complexes able to introduce empty levels slightly above the valence band. In this condition electron promotion from the valence band to the empty acceptor state creates mobile holes. Traditionally, this has been realized by using a native p-type semiconductor, such as delafossite oxides ($CuMO_2$M= Al, In, Ga, Sc, Fe, Co, Rh or lanthanide) or by reversing the native n-type conductivity of wide band gap semiconductor, such as ZnO[3,4].

Production and reproducibility of p-type ZnO is still a matter of controversy in the scientific community, especially because for ZnO no bipolar behaviour is expected according to theoretical calculation. Therefore, reversing the type of carrier will imply the formation of compensating defects. For this reason, in this thesis focus has been put on the second class of material.

Few p-type TCOs or wide band gap semiconductors have been reported so far: some oxides with delafossite structure, $SrCu_2O_2$, some spinel structures such as $ZnRhO_4$, layered chalcogenide LaCuOCh, (Ch=S, Se, Te) and SnO are the most relevant materials. Most of the data reported

in literature deals with the delafossite structure[5-9] with the record conductivity for oxides reported for CuCrO:Mg[10]. These oxides performancesare still much worse than those of conventional n-type TCOs in terms of both optical and electrical properties: maximum transparency is around 70% in the visible range while conductivity is in the range of 10^{-2}-10^{1} S/cm, that's to say several order of magnitude lower than the conductivity of conventional n-type TCOs (10^{4} S/cm)[6-8], while better properties were achieved in chalcogenides[11-13]. Limits to the conductivity are mostly due to low holes mobility, which turns out to be a consequence of the band structure of most of transparent oxides. In fact the mobility is inversely proportional to the effective mass of the carrier which in turn is inversely proportional to the curvature of the valence band. For transitional metal oxide the valence band is formed by highly directional oxygen p or metal d orbitals. The spatial overlap between these orbitals is small and therefore the valence band appears narrow (flat) and less disperse in comparison with the conduction band of conventional n-type TCOs (Figure 5.1).

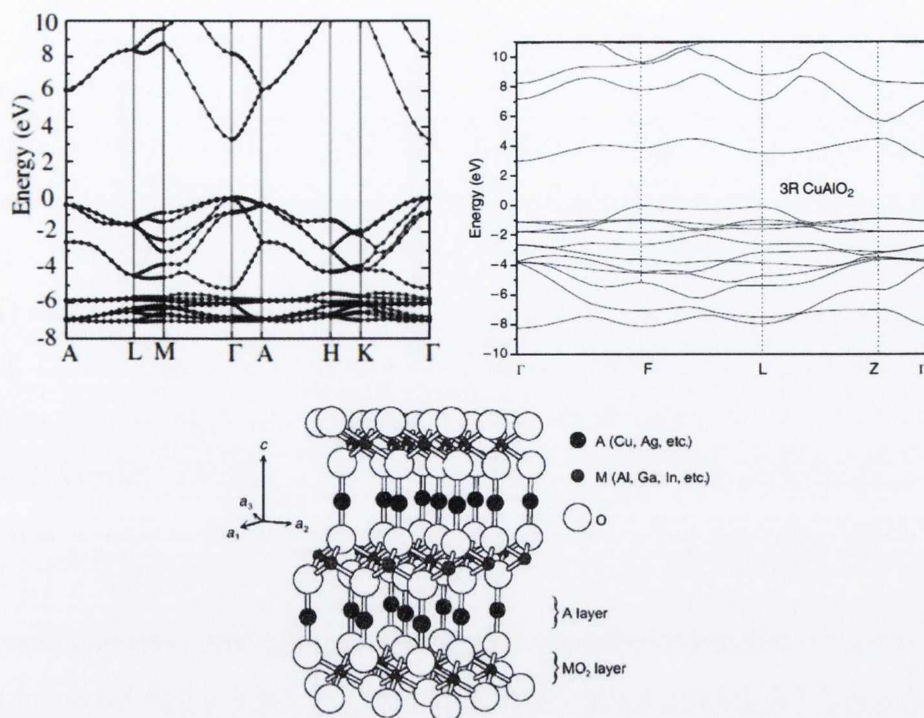

Figure 5.1 A comparison between the band structures calculated for ZnO (ref [14]) and $CuAlO_2$(ref. 15). Notice the difference between the dispersion of the bottom of the conduction band for ZnO in comparison to the top of the valence band for $CuAlO_2$. The band structure and a schematic view of a delafossite structure is reported (ref 16).

As a consequence also the conduction mechanism for the carriers is different. While conventional n-type TCO are generally band conductors, p-type TCOs are usually polaron conductors[17]. This mechanism is associated with the presence of a localized charged state formed at a cation site and its movement through the material. This state is usually rather localized due to the Coulombic interaction between the hole and a crystal site which *traps* it. In particular, for the delafossite structure this is a consequence of the high electronegativity of the oxygen 2p-state. As a consequence, once a positive hole is introduced, it behaves like a deep acceptor level, i.e. it remains almost localized on a single oxygen atom rather than migrate within the crystal lattice, even under applied field[18]. If this self-trapping energy is low enough and a sufficient quantity of energy is provided, this charge can hop from one site to the next. It is worth noting that this mechanism doesn't involve any physical movement of cation, but rather an electron movement through the valence band, with a simultaneously temporary change in the

cation oxidation state. Therefore this charge hopping process is more likely for cations that exhibit strong covalent interaction with the oxygen anions. As a result, there are several conditions that must be fulfilled in order for the polaron mechanism to occur: a suitable crystal lattice with a covalence rather than ionic nature of bonding, cations with multiple oxidation state available and a relative low value of hopping activation energy[19]. The success of delafossite AMO_2 (where A is a monovalent cation and M is a trivalent cation) as p-type TCOs is based on the careful choice of the cations A and M according to the chemical modulation of the valence band (CMVB) approach and in the choice of the appropriate crystal structure (Figure 5.1) [16]. Delafossites have a hexagonal layered structure where layers of A cation and of MO_2 groups are stacked alternatively, perpendicular to the *c* axis. The features of the A cation determine the distance between the layer, due to the strong repulsion between the d electrons of the A cation and the 2p electrons of the oxygen ions. For a cation with all the d states occupied (i.e. a d^{10} configuration) and small coordination number, it can be presumed that the closed shell electrons (d^{10}) lie roughly at the same energy levels of the 2p electrons of the oxygen. If this condition is fulfilled, chemical bonds with considerable covalency are formed. The resulting antibonding levels become the highest occupied states, i.e. the valence band edge. Moreover the tetrahedral coordination of the oxide ions induces a sp^3 conformation of this ion, and therefore, all the 8 electrons of the oxygen atom are distributed in 4 σ bonds with the coordinating cations thus reducing the non-bonding nature of the oxide lone pairs. These two structural properties reduce the localization of the valence band edge, in other words they promote the formation of an extended valence band structure where holes can migrate more easily. Despite this favourable condition, the main limitation of delafossites materials is still the low hole mobility ($<1 cm^2V^{-1}s^{-1}$) which makes them useless for application in transparent TFTs[17]. Thus their use as highly transparent and conductive material will be limited, while their development will likely to be focused on fundamental studies of opto-electronic properties, defect and transport issues or for those applications where polaron conductivity is useful[17].

The limitations reported for delafossites material pushed the interested and the research beyond this type of structure. For this reason, new non-delafossites oxides have been synthesized. Among this $SrCu_2O_2$[20], NiO[1,21], some spinel structures such as $ZnRh_2O_4$[22-26] and SnO[27-30] are the most common.

$SrCu_2O_2$ has similar properties compared to delafossites materials, in terms of band gap (3.3 eV) and hole mobility (μ=0.46 $cm^2V^{-1}s^{-1}$). Diodes have been grown by using such material[17,31].

NiO has properties comparable to those of delafossites material (μ<1 $cm^2V^{-1}s^{-1}$, transparency in the visible range of 40÷80% depending on the conductivity)[1,17,21].

ZnM_2O_4(M= Co, Rh, Ir) has again a very low mobility. Its most outstanding propertyis the fact that $ZnRh_2O_4$ is the only amorphous p-type oxide reported so far. Amorphous p-n junctions showing rectifying behaviour have been fabricated by using this material[17,25]. However there are two main limitation: Rh is a precious metal and the band gap is determined by the ligand field splitting of the d orbitals of the metal. In this case it is important to strengthen the crystal field to open up the band gap which, at present, is too small (2.1-2.7 eV) for any application in transparent TFTs.

In the case of p-type SnO, the localization of the oxygen 2p orbitals is partially lifted by the contribution of spatially spread $5s^2$ tin orbitals to the top of the valence band[28,29]. The origin of the p-type conductivity has been attributed to the presence of tin vacancies and oxygen interstial, the former mechanism being the dominant one. Once these defects are fully ionized, they produce a band deformation close to the top of the valence band maximum with the formation of acceptor like states[29]. The advantages of this material are the good electrical properties (reported room temperature Hall mobility ranging from 2.4 to 4.8 $cm^2V^{-1}s^{-1}$)[28,29] and the reported possibility of bipolarity, while the main limitation is the narrow region of suitable growth conditions[28,29]. Moreover its stability is still a matter of debate. Despite the fact that stability of the material and relative properties has been reported for samples stored in a vacuum desiccator for a period of

6 years[27], it is known that SnO is thermodynamically instable at temperature above 543K in air[30,32].

A lot of work still needs to be done to understand and improve the existing p-type TCO, at the same time new materials are required to overcome their limitations.

In this work, an attempt has been made to design new materials and a new strategic approach, based on a simultaneous cation and anion doping. The exploitability of the co-doping approach and its applicability to different oxides is still a matter of study. Despite the fact that Cr_2O_3 might not be an ideal candidate,due to its very low native conductivity, this latter approach worked quite efficiently. The results obtained will be presented.

5.2. Dopability of p-type TCOs

Doping of wide band gap semiconductors to obtain p-type conductivity without compromising the transparency is not a trivial process. Even when, from a theoretical point of view, desired properties can be obtained by doping a host oxide with a defined element, obtaining the same results from an experimental point of view might be more difficult due to the influence of the deposition parameters in the material synthesis which may result in a fine and complex balance between defect formation and compensating defects.

Recently Zunger[33] has summarized some doping principles which can help the design of an appropriate deposition strategy. If one considers the formation enthalpy of a dopant D with a charge state q_D in a host crystal H (eq 5.1), the 3 main contributions will be:

(i) the introduction of compensatingdefects, in other words the spontaneous formation of hole killer defects due to the lowering of the Fermi level upon p-type doping,

(ii) the effects of adjusting the chemical potential of different elements

(iii) the local bond effects of the dopant on the lattice

$$\Delta H^{(D,q_D)}(\mu, E_F) = q_D E_F + n_D(\mu_D - \mu_H) + \Delta E_b \qquad 5.1$$

In eq. 5.1, μ_D and μ_H are the chemical potential of the dopants and host respectively, E_F the electrochemical potential (Fermi energy), n_D the number of dopants, E the total energy and ΔE_b the excess energy of the local chemical bonds around the dopant defined as:

$$\Delta E_b = E(host + defect) - E(host) \qquad 5.2$$

Regarding point (i), equation (5.1) shows that if a donor is formed, it donates electrons that will contribute to the free carrier reservoir whose energy is E_F. In this way the formation energy of the donor increases linearly with E_F. Similarly, the presence of acceptors will remove electrons from the reservoir and thus the acceptor formation energy decreases linearly with E_F. These trends are reported in Figure 5.2.

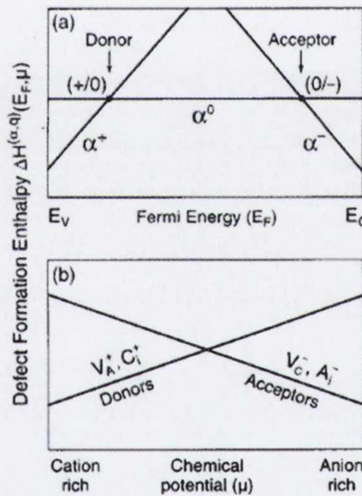

Figure 5.2Schematic depiction of: (a) the dependence of the formation energy of a defect α (with a value of q_D which can be +,0 or -) on the Fermi energy; (b)the formation enthalpy of some intrinsic defect (anion vacancy V_A^+, cation interstitial C_i^+, cation vacancy Vc^-, anion interstitial A_i^-) on the chemical potential (taken from ref. 33)

This implies that when a material is doped n-type, the Fermi level will rise to such a point that acceptors defects will form spontaneously. A symmetric discussion applies to p-type dopants, where the donors' defects behave as hole killers are mainly anion vacancy or cation interstitial. The value of E_F

at which this occurs is defined as pinning energy. The position of the valence band maximum (VBM) for p-type and conduction band minimum (CBM) for n-type with respect to the energy pinning level is crucial: in order to achieve p-type conductivity, the valence band maximum should be close to the vacuum level (small ionization potential)[15]. For example, the reason why ZnO is so difficult to dope p-type is due to its deep valance band. In this particular case the p-type pinning level is considerably above the valence band maximum. Thus the downwards movement of E_F due to p-type doping will encounter the pinning level before encountering the VBM. At this point hole killers such as zinc interstitial or oxygen vacancies will be formed before achieving any significant p-type doping.

There are a few ways to circumvent this problem. One way is to insert an element which induces an up-wards shift of the valence band. This, for example, is the case of valence band modulation proposed by Hosono and co-workers. A second possibility is to design deposition conditions such that formation of hole killers (anion vacancy and cation interstitial) is inhibited. For example the presence of H during Mg-doping of GaN and the following annealing out was the recipe for the success of p-type GaN. Similarly the use of NO and NO_2 as N sources can facilitate the deposition of p-type ZnO by creating internal oxygen precipitation which eliminates oxygen vacancies[33].

Regarding the chemical potential effect (point ii), it can be seen from Eq. 5.1 that the formation enthalpy of intrinsic defects (for example anion vacancy) depends upon the anion and cation chemical potential. For example, anion substitution as in p-type ZnO:N will be easier if the growth conditions are adjusted to have host cation (Zn) rich conditions, because the solubility of anion substituting dopants is higher under host anion poor conditions. In the same condition, though, also the enthalpy of formation of anion vacancy (a compensating defect) is favoured, because defects that donate host anionsto the reservoir are easier to form if the reservoir has a low anion chemical potential (anion poor). A similar discussion can be done for doping on the cation site. From this consideration, it is already clear that

p-type doping in oxides is best achieved in oxygen rich, cation poor growth conditions.

Once the desired defect is introduced, it might not be stable over time. The reason for this is that the energy of the new bond arrangement is less favourable than that of the original host (ΔE_b>0). This is reflected in the (*iii*) condition. In some cases this can be overcome by co-doping or cluster doping with appropriate elements (for example Al in the case of ZnO:N) able to form very strong bonds with the dopant without destabilizing the host structure. In this way the dopants are stabilized (ΔE_b <0) and their solubility is enhanced.

5.2.1. Deposition of new and alternative material: a strategic overview

Rather than trying to reverse the conductivity of native n-type semiconductor, I tried to improve both optical and electrical properties of a native p-type material. Such a challenge can be difficult to achieve by doping with a single element, therefore the possibility of using anion and cation co-doping was preferred. This is actually not a new idea itself, as in many cases it was applied to ZnO[34-38], and it was suggested as a possible avenue to be explored for the design of p-type TCOs[39].

First of all, a suitable candidate material needs to be chosen. From now on, this oxide will be referred to as the host matrix, as it represents the host structure on which doping was performed. In my case it was found that chromium oxide, Cr_2O_3, can accomplish this role. In fact, Cr_2O_3 is a wide band gap insulator in its stoichiometric form with possibility of native p-type conductivity. The latter can be enhanced by doping with Mg[40,41]. However, Cr_2O_3 has some limitations, in particular, it has transitions in the visible range due to the presence of semi filled d-states. The question then becomes how to tune the optical properties in order to improve the

transparency. In the case of solution chemistry, tuning of the optical properties of transitional metal complex can be performed by varying the strength of the crystal field created by the ligand atoms. It is well known that the N-coordinating ligands create a stronger crystal field than O-coordinating. CrN in itself is thermodynamically stable, and exhibits quite different properties than Cr_2O_3, since CrN is semiconductor with a band gap of 0.7 eV[42]. In between these two extremes, chromium oxy-nitrideswith different oxygen content can be grown[43-46]. The results reported in these latter studies will be compared to those obtained for the in house grown films.

5.3. Cr_2O_3: crystal structure and band structure

Chromium sesquioxide, (Cr_2O_3), known also as chromia (mineral name Eskolaite), is an antiferromagnetic wide band gap insulator (Eg=3.4 eV). It is the most stable oxide that chromium can form and it is well known as a refractory material and for its mechanical properties, being one of the hardest oxides[47].

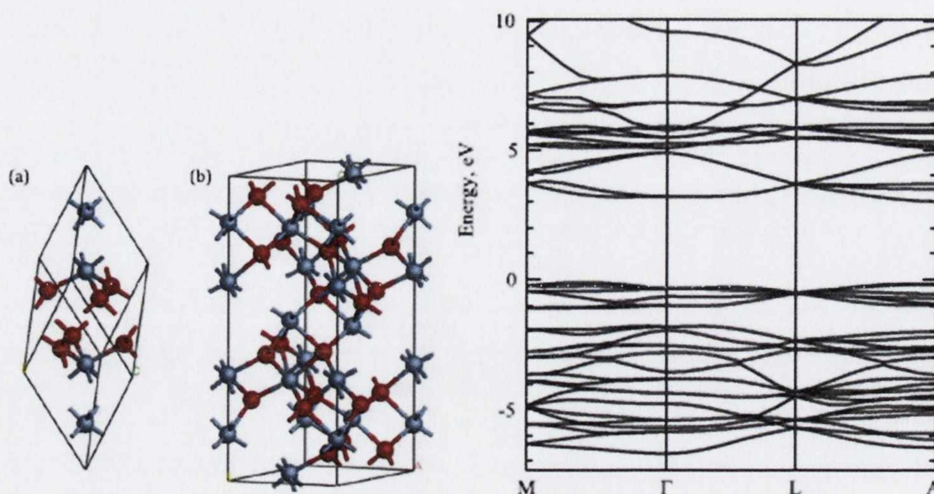

Figure 5.3. On the left, the crystal structure of Cr_2O_3:(a) the rhombohedral primitive cell and (b) the hexagonal representation; Cr atoms are represented in blue, O atoms in red. On the right: the band structure calculation of Cr_2O_3. (taken from ref. 48)

It crystallizes in the corundum structure with hexagonal closed packed layers of oxygen atoms and two thirds of the octahedral sites filled with Cr atoms[49,50] (Figure 5.3b). Each octahedron shares one face and three edges with neighboring occupied octahedral, with the metal cation slightly displaced from the geometric center of the octahedron[51,52]. Both this latter effect and the fact that one third of the octahedrons are empty are advocated as causes of a slight difference in the O-O distance[51-53]. The primitive cell is rhombohedral (space group R-3c) with crystal parameters a=4.9587Å and c=13.5942Å (Figure 5.3a).

Due to the octahedral field, the Cr 3d states are split into sub-bands: the triple degenerate t_{2g} and the double degenerate e_g. Understanding the energy position of these 2 bands and their relative contribution to the valance band maximum and conduction band minimum is important in order to understand the optical and electrical properties of this material.

Some reports tend to classified Cr_2O_3 as a Mott-Hubbard insulator[54-56], while for some others this oxide is borderline between the latter and a charge transfer insulator[48,49]. In order to clarify this point, it is necessary to have a closer look to the valence and conduction band structure, to evaluate the contribution of both the Cr 3d level and the oxygen 2p levels to either band. According to the classification by Zaanen et al.[54] and Olalde-Valasco et al[57], the 2 quantities which determine the classification are the Coulomb interaction of the transitional metal (TM) 3d levels (U_{d-d}) and the charge transfer (CT) energy between the TM-3d and anion p-states Δ_{C-T}. If $U_{d-d} < \Delta_{C-T}$ then the fundamental band gap is proportional to U_{d-d} and the material is a Mott-Hubbard insulator. In this case both holes and electrons move in d bands and are heavy (Figure 5.4). If $U_{d-d} > \Delta_{C-T}$, then the energy gap is proportional to Δ_{C-T} and the material is charge transfer insulator (or semiconductor). The top of the valence band is formed by the anion 2p states and the electrons are heavy (d-bands). Intermediate cases tend to have holes of intermediate mass and heavy electrons.

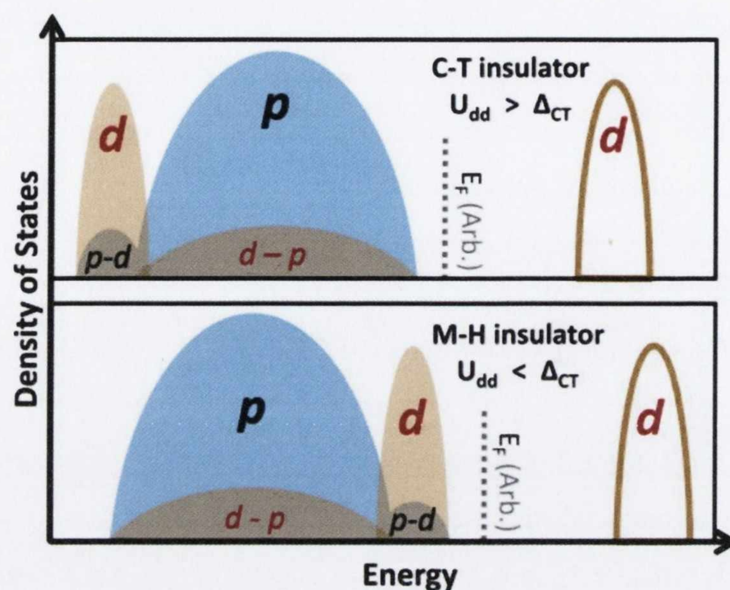

Figure 5.4 Schematic view of the valence band maximum and conduction band minimum for the case of a charge transfer insulator, where the top of the valence band consist of mainly oxygen p states, with only a small or negligible contribution from the metal d states, and a Mott-Hubbard insulator, where the VBM is mostly composed of metal d states. Taken from ref. 57.

Most of the time, photoelectron spectroscopy is used to determine the valence band feature. However, this technique only gives information about the total density of states and, therefore, a theoretical aid is required in order to deconvolute the cation and anion contribution. Moreover, since only the valence band is probed, a direct measurement of the conduction band (inverse photoemission spectroscopy) would be necessary in order to correctly determine $U_{d\text{-}d}$ and $\Delta_{C\text{-}T}$.

According to both calculation and valence band measurements by X-ray or Ultraviolet Photoelectron Spectroscopy (XPS and UPS respectively) the top of the conduction band is formed by a mixture of oxygen 2p and the occupied chromium 3d (t_{2g}) states whose degree of overlapping depends on the type of calculation[48,50,58]. This is the reason why there is still an on-going debate in literature whether Cr_2O_3 is a Mott-Hubbard or an intermediate insulator. It is worth noting that the possibility of having an intermediate insulator would be helpful in order to achieve p-type conductivity. As already mentioned in the introduction of this chapter, strong overlap between O_{2p} and the metal d levels is desirable in order to favor the hopping process. Moreover, such an ad-mixture will be a favorable

condition to a successful valence band modulation by means of simultaneous cation and anion doping.

Regarding the optical properties, the Cr_2O_3 band gap is reported to be 3.4 eV. Beyond the absorption edge, two other optical transitions are clearly present in the visible range, at energy of~2 eV and ~2.6 eV in almost any transmission spectra of Cr_2O_3 reported in literature, despite the growth technique used to deposit the samples. These 2 peaks are traditionally attributed to d-d transitions, from occupied t_{2g} levels to unoccupied e_g levels[59-61]. In this assignment unoccupied e_g levels are present in the middle of the band gap and the crystal field (splitting between the t_{2g} and e_g levels) has been evaluated to be 2.3-2.6 eV[49,62]. However none of the band structure calculation reported so far have shown such mid-gap states[48,56].

From the electrical point of view, Cr_2O_3 is usually reported as an insulator, with the possibility of very low native p-type conductivity. Doping with Mg is well known to induce a p-type semiconductor behavior.

In the following sections the results obtained on the modification of Cr_2O_3 will be presented. The effect of introducing different elements as well as different growth conditions will be outlined.

5.4. Cation-anion doping of Cr_2O_3

In the following paragraphs, the results obtained on both spray-pyrolysis and pulsed laser deposition grown films will be presented. First the results obtained by chemical deposition will be outlined, with particular emphasis on the role of this new material as a p-type TCO and on the effect of different deposition conditions on the defect formation. Following, the results obtained by PLD will be presented. The purpose of this section will be to compare the properties of the same material between the two different deposition techniques.

5.4.1. Spray pyrolysis deposition of Cr_2O_3:(Mg,N): a new p-type transparent semiconductor

Undoped chromium oxide was subject to both cation and anion doping in order to improve both optical and electrical properties. Four different sets of films were deposited: undoped Cr_2O_3, Cr_2O_3:N, Cr_2O_3:Mg, Cr_2O_3:(Mg,N). Films weredeposited on glass substrates (Roth cover slips, thickness 0.17 mm). For the deposition, $Cr(NO_3)_3$ and $CrCl_3{\cdot}6H_2O$ has been used as Cr precursor, deionised water as solvent and oxygen as a carriergas. Doping has been carried out using $MgCl_2{\cdot}6(H_2O)$ as cation dopant while $NH_4(CH_3CO_2)$ and NH_4Cl have been used as anion dopant. All films were deposited by using 0.1M concentration of Cr in solution. N and Mg concentration were changed over a range of 0.2 to 0.5M and from 0.005 to 0.01M respectively. The high nitrogen concentration was required due to the low efficiency of precursor decomposition or nitrogen incorporation. For each precursor solution the pH wasvaried from 6 to 0 by adding HCl, which primarily helped precursor solubility, but has also beenshown to improve the film properties.

Taking into considerations the results obtained in the study of the role of the precursors chemical composition on the physical properties of n-type TCOs, and, in particular, the studies reported in Chap. 4.2, the first set of samples was deposited by using $Cr(NO_3)_3$, $MgCl_2{\cdot}6(H_2O)$ and $NH_4(CH_3CO_2)$ as precursors, HCl as additive, water as a solvent and oxygen as carrier gas.

The crystal phase was determined by X-ray diffraction using a Bruker D8 Discovery. Patternswere analysed by numerical reconstruction of line profiles according to the Rietveld method using the MAUD software package. All samples consist of a single phase, Cr_2O_3, witha corundum structure (PDF number 01-072-3533). The actual incorporation of dopant elements was examined by X-ray photoelectron spectroscopy (XPS). The N1s state was identified at the characteristic binding energy (E_b=397 eV). A

quantitative analysis is however difficult due to the poor signal to noise ratio and modification of the surface due to the Ar sputtering, a procedure necessary to remove any potential precursor contamination before the XPS measurements. Optical transmission measurements in the UV-Visible rangewere performed in order to monitor the effect of nitrogen on the specular transmission of visible light by using a Cary 50 spectrophotometer. A progressive increase in transmissionand a band gap opening is observed as the nitrogen concentration in the solution was increased (Figure 5.5).

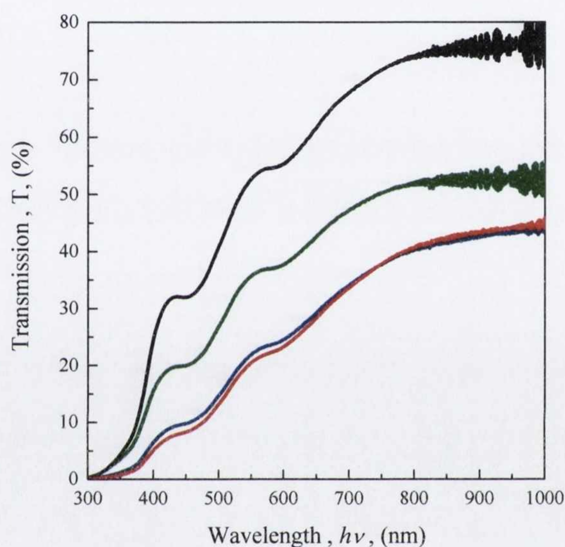

Figure 5.5 UV-VIS transmission measurement of undoped Cr_2O_3 and Cr_2O_3:N as a function of N content: undoped Cr_2O_3(—), Cr:N ratio 1:2 (—), 1:3 (—), 1:5 (—). The Cr:N ratio refers to the precursor solution. A bare substrate was used as a reference.

There are several possibilities why the specular transmission can improve:

1. a systematic difference in sample thickness

2. a systematic difference in microscopic surface roughness and reduction in scattering losses

3. changes in the macroscopic morphology caused by changes in precursor solution density, reaction pathways or droplet sizes induced by the large molarities of the nitrogen precursor in the solution

4. an improvement in optical properties of the material: a difference in the extinction coefficient of the samples could be a consequence of the incorporation of the nitrogen into the Cr_2O_3 matrix.

A detailed analysis was carried out that allowed to dismiss the first two hypotheses. Small scale surface roughness for doped and undoped films is comparable as confirmed by atomic force microscopy (Figure 5.6). Rms roughness values were determined for 20×20 μm and 5×5μm scans. The analysis of the 20 μm scan highlights the presence of a granular structure which gives rise to a long range waviness in all of the samples. The rms values for the scans were on the order of 60-80 nm. Small scale images highlight the roughness arising from the individual grains as also seen in the cross-sectional SEM images (Figure 5.7). Rms values of 20-40nm were measured on that scale. No systematic correlation was found between the rms values and transparency.

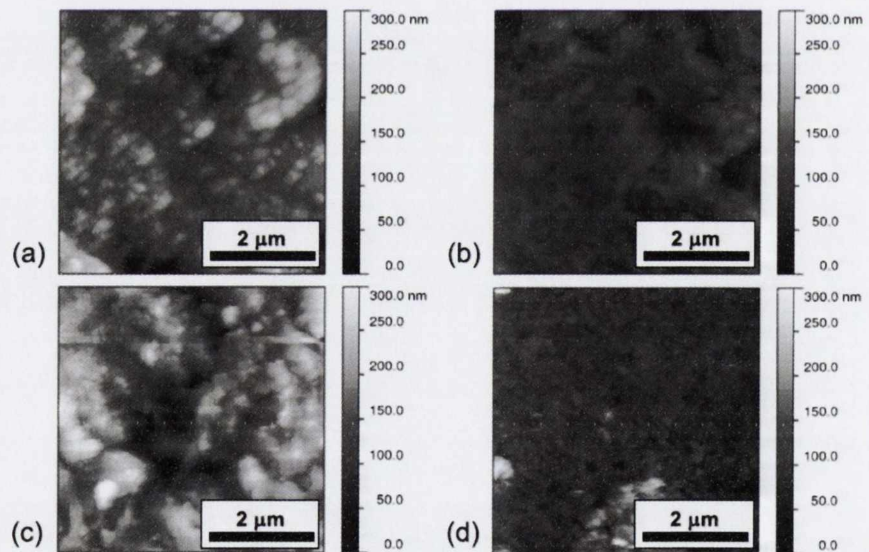

Figure 5.6 AFM images of the undoped and N doped samples at different nitrogen concentrations: (a)undoped Cr_2O_3 (rms = 40 nm), (b) Cr:N 1:2 (rms = 25 nm), (c) Cr:N 1:3 (rms = 50 nm), (d)Cr:N 1:5 (rms = 25 nm).

In order to compare the effect of different nitrogen content in solution, it was necessary to calculate the absorption coefficient. The most rigorous way to determine it, is by spectroscopic ellipsometry, as the complex refractive index of the material can be extracted. However, the high surface roughness of the samples leaded to a strong depolarization of

the light, thus making such measurements impossible or unreliable. Therefore a much more crude method was used, which consist of using the Beer law and determine the absorption coefficient from transmission measurements. Reflectance measurements could not be performed as the required sample holder was not available. Again, in order to take into account the effect of surface roughness, integrated transmission measurements were performed, rather than specular transmission measurements. These were combined with thickness determination by cross-sectional SEM for all individual samples.

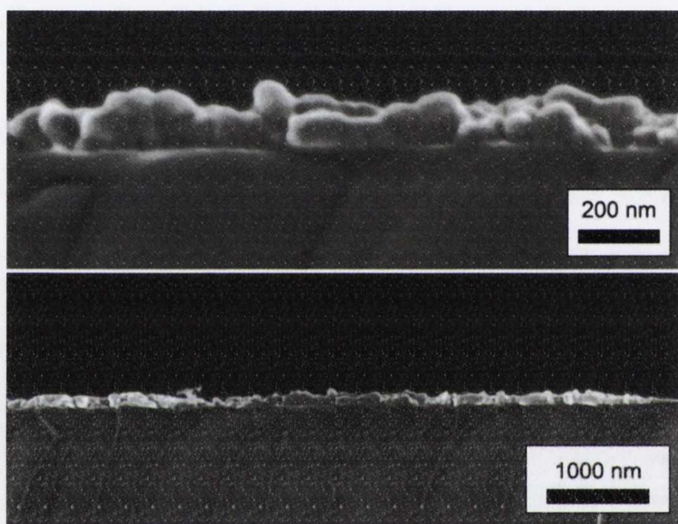

Figure 5.7Cross sectional SEM of Cr_2O_3 doped with both nitrogen and magnesium deposited on glass. The thickness of this particular sample was found to be 115±25 nm.

In this way the absorption coefficient was calculated for the film (Figure 5.8)

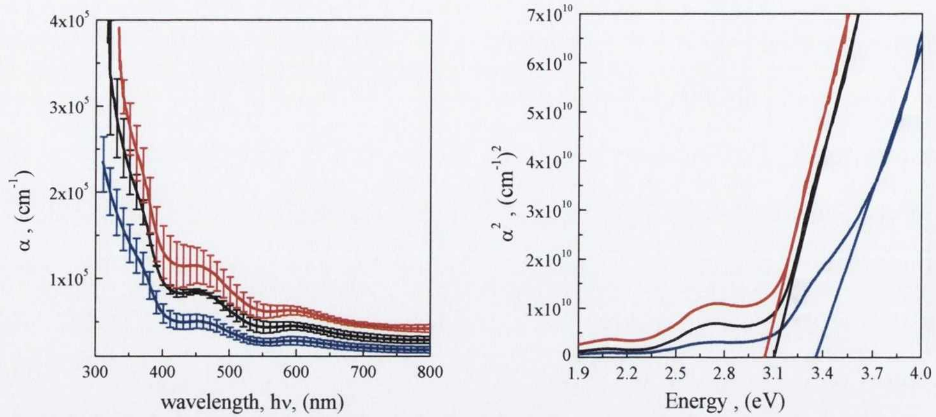

Figure 5.8. Absorption coefficient calculated from transmission measurements and thickness determination from cross sectional SEM and band gap determination for samples grown with different nitrogen content in the solution: (—)no nitrogen in solution, (—)Cr:N ratio in solution 1:3, (—)Cr:N ratio in solution 1:5.

Samples grown with nitrogen show better overall transparency, and SEM micrographs show fully closed layers. Hence the increase in transparency is not caused by an increased number of cracks in samples. Quite the contrary, the presence of nitrogen is improving homogeneity.

The same effects on the optical properties have been observed for amorphous Cr_2O_3 grown by sputtering by Qin et co-workers[63] (Figure 5.9). In this latter case a progressive increase in transmission and band gap opening were observed as the nitrogen flow in the deposition environment is increased. In this contribution the improvements in the optical properties was attributed to the presence of nitrogen itself.

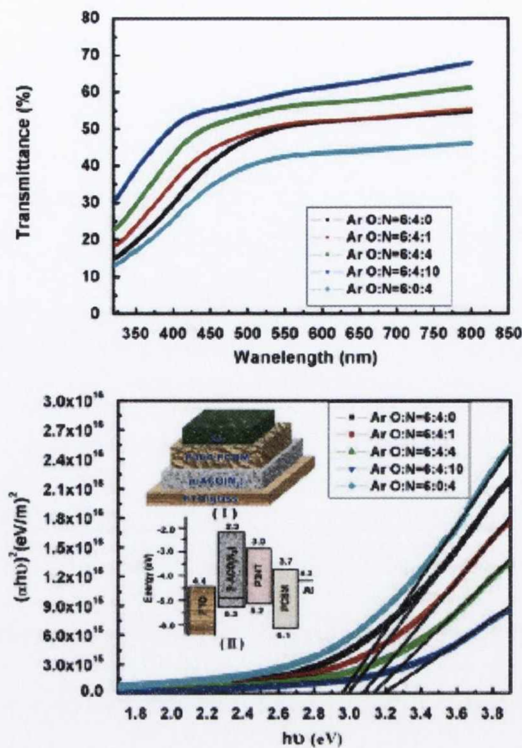

Figure 5.9 Transmittance and band gap determination of amorphous chromium oxide thin films grown by sputtering as a function of nitrogen flow. Taken from ref. 63.

Since all the other possibility have been ruled out, the only explanation left is an effect of the N on optical transitions. This can eitherbe due a direct effect on Cr d-levels and therefore an enhanced crystal field, or by inducing lower broad-band absorption due to either a change in the symmetry around the Cr atom, a modification of the valence band density of states or by preventing the formation of parasitic defects.

All nitrogen-only doped samples are poorly conducting or insulating. Conductivity decreasesas the nitrogen nominal concentration increases. To increase the conductivity of the oxide, Li, Mg, Ca, In and Zn were chosen as doping elements. Li or Ca or In incorporation leads to insulating samples. Mg and Zn lead to conductive samples, but in the case ofZn only slight improvements were observed. Doping with Mg instead, produced a remarkable improvement in the electrical properties while maintaining the p-type character of thecurrent carriers. For the Cr_2O_3 samples doped only with Mg, no major differences in the specular transmission ware observed when compared with the undoped material (Figure 5.10).

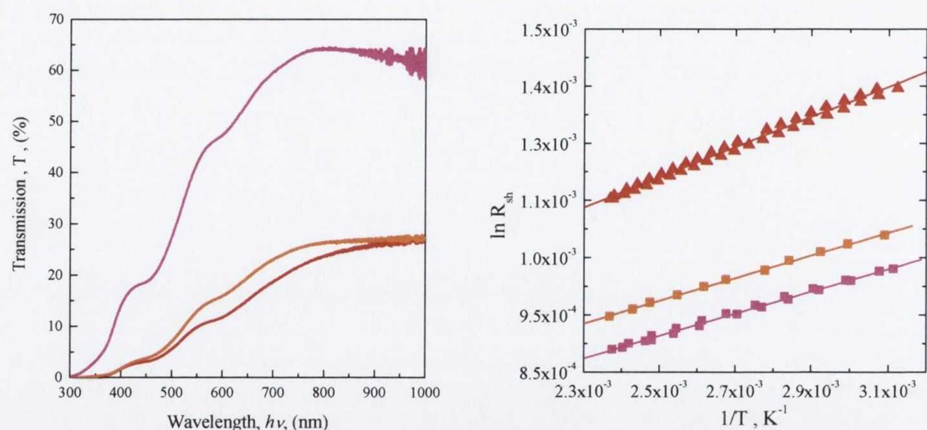

Figure 5.10 Specular transmission measurements (left) and Arrhenius plot (right) of (—) undoped, (—) Mg-doped and(—)Mg,N-codoped films.

However the resistivity decreased from 400 Ωcm for plain Cr_2O_3, reaching its minimum value of 15 Ωcm for Cr_2O_3:Mg at a ratio Cr:Mg of 9:1. The actual incorporation of Mg and its ratiowith respect to Cr were confirmed by XPS measurements. Hall coefficients could not bedetermined for both undoped and Mg doped Cr_2O_3 as the resistivity of the films was too high to achieve good signal to noise ratios in the measurement system available. In the case of undoped Cr_2O_3 it was not possible to identify the carrier type as the conductivity was too poor for the sensitivity of the apparatus. Instead for the Mg doped samples, the Seebeck coefficient was found to be +75 μVK^{-1}, meaning that the films are p-type. Resistivity values were scanned over a temperature range from 323 to 423K. Carrier activation energy of 200 meV was derived from an Arrhenius plot of these measurements (Figure 5.10).

In a second set of samples the two doping methods were combined. (Zn, N) co-doped samples showed a good improvement in the electrical properties, with a minimum resistivity of 18 Ωcm. For Mg,N-co-doped samples, instead a major improvement was observed.

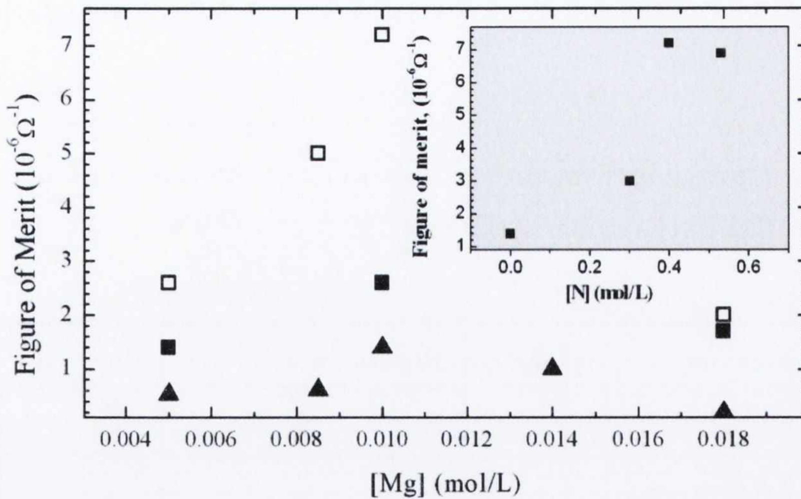

Figure 5.11. Screening process to determine the best compromise between Mg, N and temperature for the deposition. The Figure of merit was used as screening parameter: (▲)[N]=0M and T=753-783K (■) [N]=0.4 M and T=753 K, and (□) [N]=0.4 M and T=753K. The inset shows the figure of merit for Cr_2O_3:(Mg,N) samples grown using [Mg]=0.01 M and T=783K for different [N] concentration.

The figure of merit ($F=1/[R_{sh}\ln(T)]$) was used as the optimization parameter (Figure 5.11), taking into consideration both optical and electrical properties. The values were calculated by taking the average transmission across the entire visible range and the sheet resistance. The best conditions were found at Cr:Mg 9:1 and Cr:N 2:8 (ratios in solution) and deposition temperature of 723K. The transmission for these samples was as high as 65%, average resistivity was 5 Ωcm, with minimum values of 3 Ωcm for films with thickness of about 180 nm. According to Seebeck and Hall coefficients (+75 μVK^{-1}, +1cm^3C^{-1}), these samples are p-typeconductors. Typical Hall mobility values were around 0.1 $cm^2V^{-1}s^{-1}$ and carrier concentration was of the order of $10^{19}cm^{-3}$. The activation energy for the carriers was 190 meV (Figure 5.10). It is worth noting that this is an improvement in the conductance by almost two orders of magnitude with respectto the nominally undoped Cr_2O_3 and by a factor of 3 with respect to doping with Mg only. Preliminary studies on post-annealing treatments showed that conductivity can be further improved by a factor of 2, if

annealing is carried out in oxygen at 823K, without compromising the optical properties.

In order to compare the quality of this material with respect to other materials reported in literature the figure of merit was calculated in a similar way for other p-type oxides reported.

Material	**F($10^{-6}\Omega$)**	**Deposition technique**	**Reference**
$CuAlO_2$	50	PLD	2
$CuAlO_2$	11	PLD	7
$CuCr_{1-x}Mg_xO_2$	500	Sputtering	10
$CuCr_{1-x}Mg_xO_2$	15-28	Spray pyrolysis	64
$SrCu_2O_2$	0.2	PLD	65
$SrCu_2O_2$:K	2	PLD	65
$CuScO_{(2+x)}$	270	Sputtering	66
$CuYO_2$	1	Co-evaporation	67
$CuY_{1-x}Ca_xO_2$	36	Co-evaporation	67
$CuGaO_2$	14	PLD	68
$CuGa_{1-x}Fe_xO_2$	29	Sputtering	9
$AgCoO_2$	4.4	Sputtering	9
a-Cr_2O_3:N	0.2	Sputtering	63
Cr_2O_3:Mg	2	Spin-coating	40
Cr_2O_3:(Mg,N)	7	Spray pyrolysis	69

Table 5.1 Figure of merit for several TCOs reported in literature.

The best figure of merit is that of $CuCrMgO_2$ grown by sputtering. However, the same material grown by spray pyrolysis has a severely lower figure of merit, reaching a value that is only slightly higher than the figure of merit of Cr_2O_3:(Mg,N). Furthermore, Cr_2O_3:(Mg,N) has a higher figure of merit than both the only-Mg doped and only-N doped Cr_2O_3 reported so far in literature. Several other p-type TCOs have a lower or comparable

figure of merit with respect Cr_2O_3:(Mg,N), despite the limitations in the deposition technique used in this study.

Moreover it has to be noted that plain Cr_2O_3 is long been known to be an exceptionally hard and durable material, which promises good stability of films in devices[70,71]. There are also reports of the possibility of n-type doped Cr_2O_3,which may open up prospects of fully transparent homo-junctions, if the anionic co-doping approach with nitrogen can equallybe employed to enhance transparency[72].

Regarding the crystallographic properties, symmetric scans show no major differences between undoped and co-doped samples, most likely due to the poor signal to noise ratio at high angles. However, in grazing incidence configuration, more information could be gathered due to a better signal to noise at higher angles and, therefore, structural and microstructural differences could be detected upon N doping. A comprehensive study in conjunction with the use of different precursor was carried out, as it will be outlined in next section.

5.4.2. Effect of the defect chemistry on the properties of Cr_2O_3 grown by spray pyrolysis

The effect of the chemical precursors was studied with particular focus on the structural and electrical properties. To this end, different precursors have been used, in particular $Cr(NO_3)_3$ and $CrCl_3$ as Cr sources, $MgCl_2$ and $Mg(CH_3CO_2)_2$ for Mg and NH_4Cl and $NH_4(CH_3CO_2)$ as N sources. HCl and HNO_3 were used in order to adjust the pH.

As it can be seen in Figure 5.12 the samples grown in the presence of ammonium acetate show a systematic shift to lower 2θ angles. This shift is not constant for all the diffraction peaks, as it would be expected from an error in the zeroing of the detector, nor can be due from a misalignment of the samples, since this is a random error. Thus it must be related to intrinsic properties of the film (Figure 5.12).

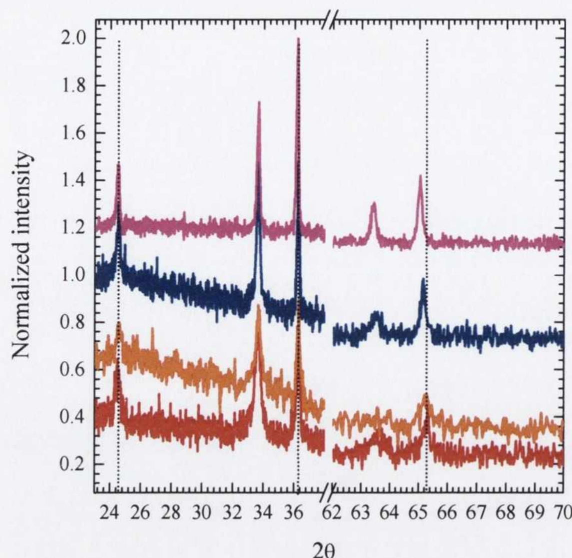

Figure 5.12 Grazing incidence x-ray diffraction of (—) undoped, (—)Mg-doped, (—)N-doped and (—) (Mg,N)-codoped Cr_2O_3. The vertical black dotted lines are guidance for the eyes.

The Rietveld analysis carried out by using the program MAUD. Crystal lattice parameters, dimension of the coherent diffraction domains and micro strain values were extracted. According to the results of the analysis the following features emerge (Figure 5.13):

- the value of the c lattice constant remains unchanged, within the experimental error, for all samples:13.582±0.006 Å for samples grown in the presence of nitrogen versus 13.583±0.0012 for undoped or only Mg doped samples
- for undoped Cr_2O_3, samples grown by using $CrCl_3$ show that the cell parameter *a* is systematically larger than those where the nitrate precursor was used; it is worth noting that the crystal structure of the samples grown by using chloride have the same lattice parameters as the database values, while for the samples grown using nitrate a contraction of the crystal cell structure is observed
- all samples where nitrogen was present in solution show bigger diffraction domains
- all samples where nitrogen was present in the solution show higher *a* lattice constant than undoped or only Mg doped samples

- a correlation between the crystallographic parameters and the crystal size could be determined, however, this cannot be related to lattice relaxation due to the small crystallite dimensions, as the crystal size (300 to 800 nm) is well above 100 nm; moreover the trend expected for size-effect is the opposite with respect to that experimentally observed

According to the above observation it can be deduced that the shift and broadening of the peaks are due to two main effects: the larger crystal size and the expansion of the cell parameter. In other words the presence of ammonium ions in the reaction environment helps to improve the crystal quality of the material deposited by improving the crystallite size. However this latter cannot be responsible for the increased crystal cell parameter *a*. In literature, a similar expansion of the crystal cell has been attributed to the incorporation of nitrogen into the Cr_2O_3 structure[43]. This should be expected as the Cr-N bond (2.06Å) is longer than the Cr-O bond (2.01 and 1.96 Å). This represents an indirect confirmation of the incorporation of N into the crystal structure of Cr_2O_3[43]

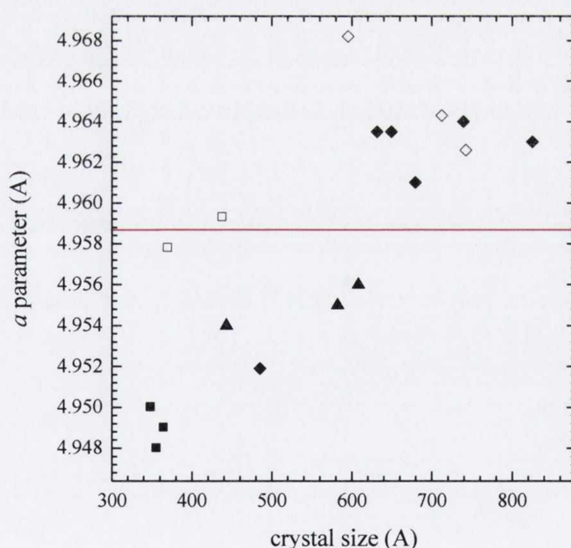

Figure 5.13a-parameter as a function of crystal size. All the empty symbols are for samples grown using chromium chloride; all the full symbols are for chromium nitrate, squared symbols are for undoped samples, triangular symbols are for only N-doped samples, rhombohedral symbol are for Mg,N-codoped samples. The red line represents the database value for the a parameter.

As previously mentioned, films grown by using the nitrate precursors show lower *a* parameter with respect to those deposited by using the chloride precursor. They also show lower resistivity than those grown by using the chloride precursor (Table 5.2). It is worth noticing that undoped chromium oxide is a highly resistive material and that the a crystal parameter *a* for the sample grown using chloride is in line with the database value, while the value for samples grown by using the nitrate show a lower lattice parameter. Theoretical calculation should be necessary to verify if these two observations are related, in other words, if the defect responsible for the conductivity is also causing a contraction of the lattice cell.

Improved electrical properties were obtained by co-doping. For the (Mg,N)-co-doped sample different condition were tested by adjusting the pH. At the beginning of this study chromium nitrate, magnesium chloride and ammonium acetate were used as precursors and HCl as additive. In this case, a systematic variation in the electrical properties was observed as a function of pH. In fact when ammonium acetate is used, the pH of the solution rises to 5-6. HCl was added slowly in order to decrease the pH in steps and the effect on the optical and electrical properties was studied. Due to the difference in the film thickness across samples, the absorption coefficient and the resistivity of the sample was determined. No systematic effect was observed on the optical properties, while a steady decline in the resistivity and in the activation energy was noticed (Figure 5.14).

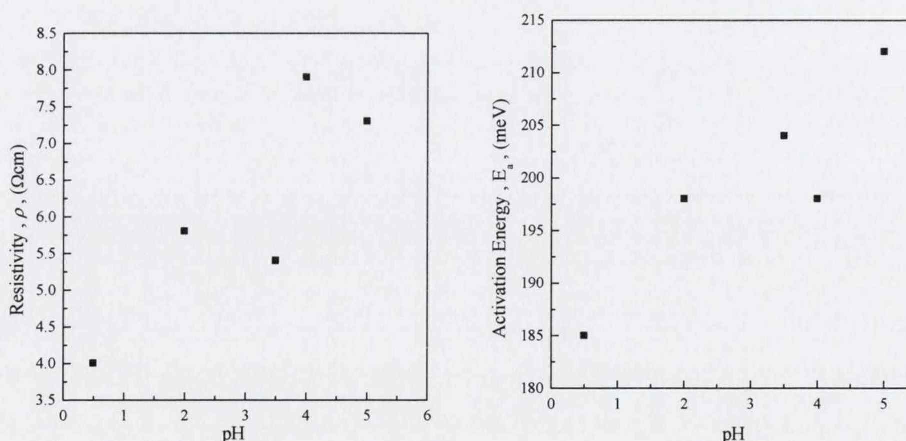

Figure 5.14 Effect of the pH on the electrical properties of Cr_2O_3:(Mg,N). A steady decline in the resistivity and on the activation energy was observed when the pH was brought to lower values.

Lowering the pH has two main consequences

- partial or complete removal of the acetate moiety, by protonation and release of the same as acetic acid
- promotion of the reaction between nitrate and ammonium by favoring the reduction of the nitrate moiety

In order to test if the acetate moiety was interfering with the reaction, samples were grown by using NH_4Cl and $Cr(NO_3)_3$ as N and Cr sources respectively, in simple words, no acetate was present in the solution. The pH of the starting solution was 3, which was later brought down to zero by adding HCl. As it can be seen from Table 2, the sample grown at pH zero has a comparable resistivity to the sample grown by using ammonium acetate, while the sample grown at a pH of 3 has a higher resistance than that grown at a pH 0. The fact that the same trend with pH was observed when ammonium chloride was used, leads to the conclusion that the effect of the pH is not related to the removal of acetate from the solution but has to be linked to the decomposition pathway followed by the nitrate moiety at different pH. It is well known that heating of ammonium nitrate solution under atmospheric pressure is followed by the decomposition of the nitrate moiety by ammonium ions in acidic environment (or ammonia in basic condition) producing N_2 and water as final product (Equation 5.3).

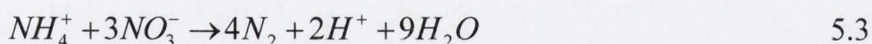

$$NH_4^+ + 3NO_3^- \rightarrow 4N_2 + 2H^+ + 9H_2O \qquad 5.3$$

The reduction of nitrate by ammonia is a spontaneous reaction according to their electrochemical potential and such reaction is favored at acid pH where ammonia is protonated to ammonium ion and behaves as better reducing agent. The final products of the decomposition vary depending on the temperature and pressure at which the reaction is conducted. High temperature, pressure and acidic pH favor this reaction. Nitrous oxides are developed during this decomposition process, and in certain circumstances they are the major final product of the reaction. For example, it was demonstrated that under pressurized condition and at 453K, NH_4NO_3 decomposes giving nitrous oxide and nitrogen with a ratio of 4:1. The content of nitrous oxide was increased as the pH was lowered. Despite the fact that in our case the reaction was conducted at atmospheric pressure but

at much higher temperature, it is reasonable to assume that the reaction between the nitrate and the ammonium ions does occur producing highly reactive species such as NO and NO_2, whose production is favored at low pH. NO and NO_2 has been reported of strictly importance in the development of p-type material, in particular when this is to be achieved by N-doping. Their effect has been attributed to the formation of oxygen precipitates which makes the formation of oxygen vacancies, a type of killer defect for p-type conductors, unfavorable[33].

Thus it can be concluded that nitrate decomposition is a key factor in achieving the right electrical properties. In order to further confirm this, some cross-check experiments were performed. In first place, the depositions have been carried out by employing $CrCl_3$ rather than $Cr(NO_3)_3$. All the other conditions were kept unchanged. The pH was adjusted to be zero by adding HCl. As it can be noticed in Table 1, higher resistivities were observed when only chloride and acetate were used, i.e. no nitrate present in the solution (line 7). In this case higher activation energies were registered as well. Following, the nitrate moiety was inserted in the solution by using HNO_3 rather than HCl to adjust the pH, and again $CrCl_3$, $NH_4(CH_3CO_2)$ and $MgCl_2$ as Cr, N and Mg precursors respectively (line 8). In this case resistivities in line with the best performing samples were achieved. Comparable sheet resistance was obtained when $Cr(NO_3)_3$ and HNO_3 were used for the deposition. These experiments confirm that the presence of nitrate in solution and its decomposition are the necessary in order to achieve the highest conductivity.

	Sample	Cr source	Mg source	N source	pH	ρ, Ωcm	*a* Å
1	Cr_2O_3	$Cr(NO_3)_3$	None	None		400	4.949
2	Cr_2O_3	$CrCl_3$	None	None		›1000	4.958
3	Cr_2O_3:Mg,N	$Cr(NO_3)_3$	$MgCl_2$	(CH_3CO_2)	0, HCl	4.0	-
4	Cr_2O_3:Mg,N	$Cr(NO_3)_3$	$MgCl_2$	(CH_3CO_2)	3,HCl	5.4	4.964
5	Cr_2O_3:Mg,N	$Cr(NO_3)_3$	$MgCl_2$	Cl	0, HCl	4.9	4.963
6	Cr_2O_3:Mg,N	$Cr(NO_3)_3$	$MgCl_2$	Cl	3, HCl	6.0	4.961
7	Cr_2O_3:Mg,N	$CrCl_3$	$MgCl_2$	(CH_3CO_2)	0, HCl	40	4.964
8	Cr_2O_3:Mg,N	$CrCl_3$	$MgCl_2$	(CH_3CO_2)	0, HNO_3	9	4.962
9	Cr_2O_3:Mg,N	$Cr(NO_3)_3$	$MgCl_2$	(CH_3CO_2)	0, HNO_3	to be determine	4.952
10	Cr_2O_3:Mg,N	$Cr(NO_3)_3$	Mg $(CH_3CO_2)_2$	(CH_3CO_2)	0, HCl	5.5	4.963

Table 5.2 Summary table about the grown samples. The sample types and the sources for the different elements are shown along with the electrical and structural

5.4.3. Determination of the nitrogen content by XPS

An attempt was made in order to determine the nitrogen content in the films by XPS. Prior to the XPS investigation, samples were ultrasonically cleaned first in acetone, then in isopropanol, in order to remove as much contamination as possible from the surface. These contaminations are the results of condensation of the precursors' vapours on the surface at the end of the growth procedure, and they may interfere with the analysis itself. This procedure however was not sufficient to completely clean the surface, and strong carbon signal was always present in the survey scan. For this reason it was necessary to proceed with sputter cleaning. As sputtering is a destructive technique, this was performed at a low acceleration voltage in order to limit the damage to the surface of the film itself.

Both undoped and doped samples were characterised. For each sample, the $Cr3p^{3/2}$ peak and the N1s peak were measured. The results for an undoped sample sputtered at E_{beam}=0.8 kV, I_{target}12 μA, P= 6.5×10^{-6} mbar are shown in Figure 5.15 as a function of sputtering time.

Sputtering time: 0 minutes

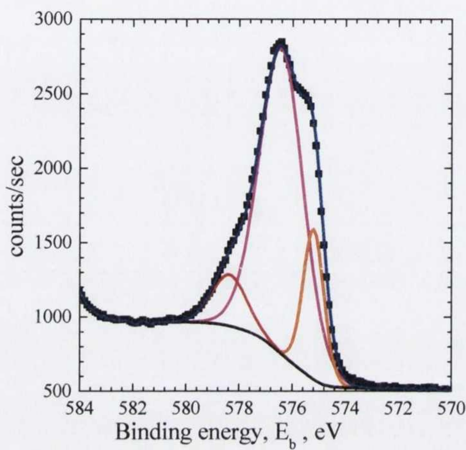

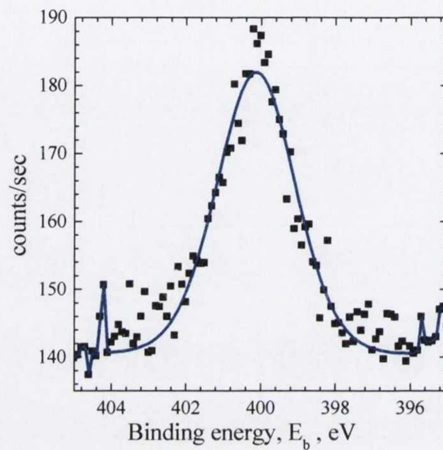

Sputtering time: 3 minutes

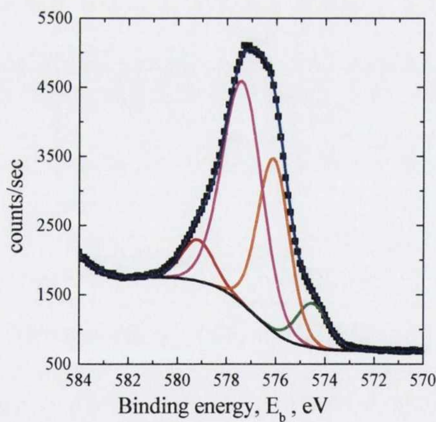

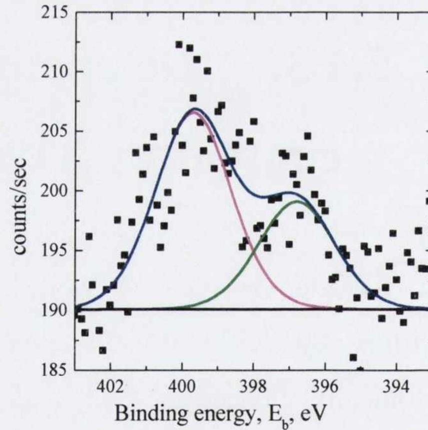

Sputtering time: 13 minutes

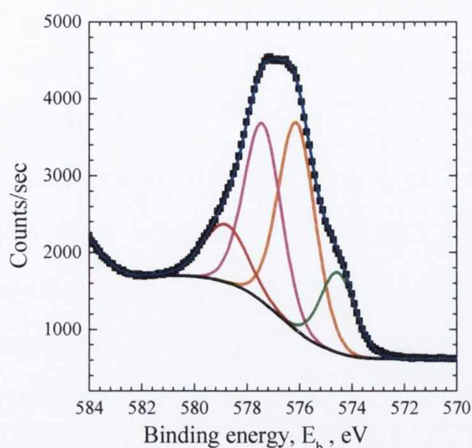

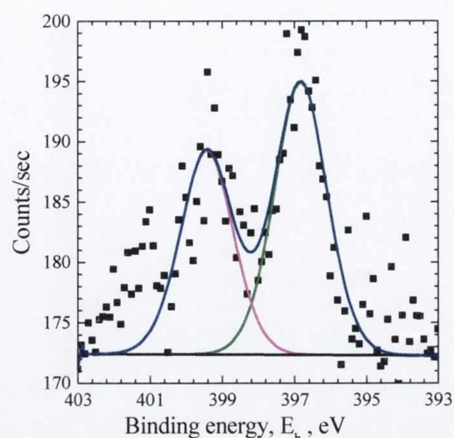

Sputtering time: 23 minutes

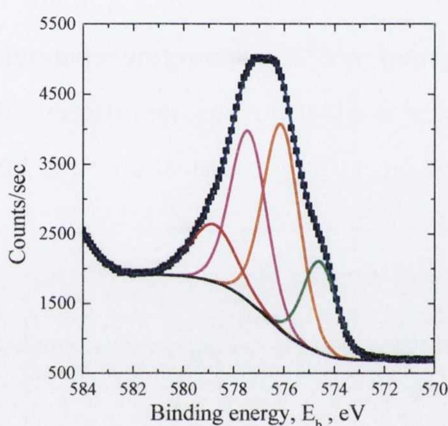

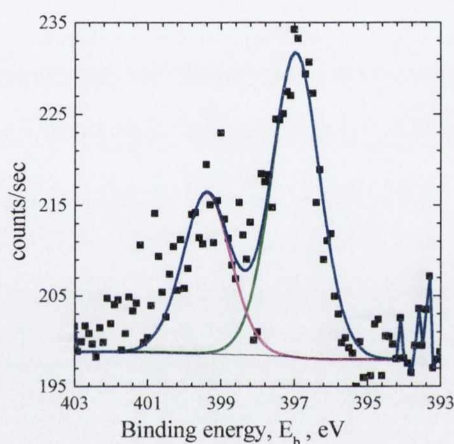

Figure 5.15 Effect of the sputtering process on the nitrogen determination by XPS. The$Cr2p^{3/2}$ and the N1s peak were monitored as a function of the sputtering time for an undoped sample. The first row corresponds to the sample as grown, in the second row the sample has been cleaned for 3 min, in the third row for overall 13 min and in the last row for 23 min. The progressive appearance of a shoulder at 575 eV and of a peak at 397eV (—) is characteristic of a Cr-N bond.

Before the sputtering treatment, 3 components were visible in the Cr peak, the main one being assigned to Cr_2O_3 (E_b = 576.5 eV), and two minor contribution from $Cr(OH)_3$ (E_b = 578 eV) and CrO_2 (E_b = 575.5 eV)[63]. The N1s peak, is centred at the binding energy (E_b =399 eV) characteristic of molecular nitrogen (N_2). After the first sputtering cycle (3 minutes), a fourth component appears in the Cr peak, and at the same time a second component appears in the N peak. According to literature these shifts are characteristic of chromium bonded to nitrogen, and of nitrogen bonded to chromium[73]. As already said, this sample was not N-doped, however since

chromium nitrate was used as precursors, the same procedures need to be repeated for sample grown by using the chloride source or for sample grown by PLD, in order to exclude the possibility of nitrogen contamination coming from the nitrate moiety. In order to assess if there is, in any case, a correlation between the appearance of this shoulders and the sputtering treatment, two more cycles of sputtering were performed and the evolution of the peaks was monitored. As it can be seen from Figure 5.15, the longer the sputtering time, the higher is the intensity of the components relative to the Cr-N bond. This treatment was repeated for other samples, even at more gentle conditions, (a comparison between an undoped and a doped samples sputtered at E_{beam}=0.35 kV, I_{target}=0.7 μA, P= 8×10^{-6} mbar for 5 minutes is shown in Figure 5.16).The conclusion is that after the sputtering treatment Cr-N bondsare detected. For doped sample the situation was not different, in a sense that, no Cr-N bond was visible on the surface before sputtering, but these components were present after the sputtering cycle.

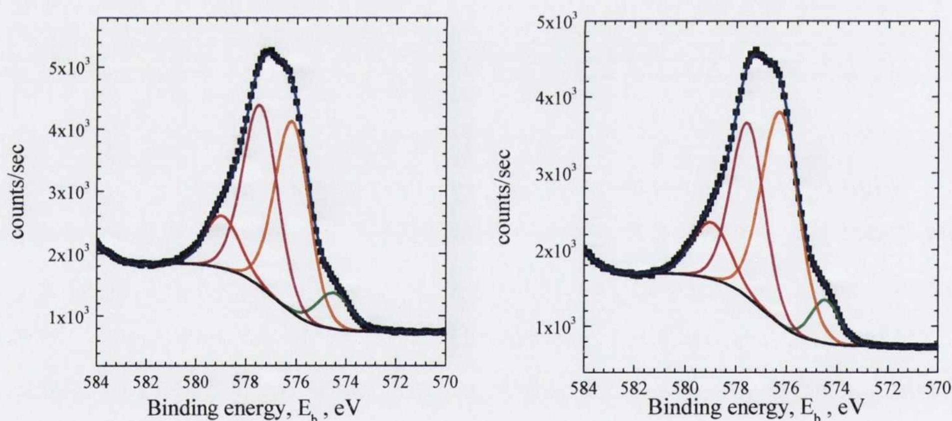

Figure 5.16 Comparison of an undoped (left) and a doped (right) sample. In both case after sputtering a shoulder attributed to the Cr-N bondwas present.

One possible explanation is that Cr-N bonds were created on top of the surface as a result of the sputtering procedure. This problem can arise in part due to the surface sensitivity used for the determination: penetration depth of x-ray during XPS is limited to the very first few nanometres of the sample. For these reasons it was not possible to determine the nitrogen content in the films. In the future, the same sputtering procedure will be repeated for sample grown by other techniques (such as PLD) or by using

precursors which do not contain any N atoms. Moreover, the presence of N will be determined by x-ray absorption studies by using synchrotron radiation. The advantage of this technique is that it is not surface sensitive, quite contrary it is a bulk sensitive technique.

5.4.4. Conclusion on the growth and doping of Cr_2O_3 by spray pyrolysis

So far, it has been shown that it is possible to co-dope a poorly conducting material and absorbing material, Cr_2O_3, improving both optical and electrical properties to such an extent as to make it suitable as a transparent conducting (or semiconducting) oxide. Systematic differences in the structural properties of the material has been noticed when nitrogen was present in the solution, as well as the enhancement of optical transparency of the material. Mg doping improved the electrical properties, however the synergistic effect of N and Mg, provide a better conductor than only Mg. At the same time it was noticed that the presence of ammonium cations and nitrate anions and the reaction between the two is the key mechanism for achieving good electrical properties. Now it has still to be understood if the improved electrical properties are the consequence of the formation of a defect complex (Mg-N) or if this is a consequence of the presence of NOx species in the reaction atmosphere that can prevent, for example, the formation of oxygen vacancies. Indeed, it has to be noted that no direct proof of the incorporation of N in the film has been found so far. This leaves still open the possibility that the role of nitrogen is limited to the passivation of defects. A full understanding of the role of each element and its effect on the physical properties is complicated, first of all, by the polycrystalline nature of the films which can accommodate a high level of defects, and, secondly, by the complicated reaction pathway undertaken by the precursors during the composition, which can lead to a variety of defects. For this reason, it is necessary to proceed with the deposition of high quality

epitaxial films, where a single type of defects can be introduced one at the time. This topic will be the matter of discussion of the following sections.

5.5. Deposition of undoped and Mg-doped Cr_2O_3 by PLD

Deposition of Cr_2O_3 by spray pyrolysis produces low quality, i.e. polycrystalline rough films. Optical and, in particular, electrical properties will be severely affected by this. In order to understand the physical limits of the material itself, it was necessary to grow high quality epilayers. In this way, dopants and eventually defects can be introduced in a controlled manner, to try, at least, to obtain some insights into the role of each element present in this quaternary compound. Furthermore, due to the improved crystal quality and morphology, some limitations of the low quality SP deposited films could be overcome, enabling measurements previously not possible. For example, it was not possible to get any ellipsometric studies on the spray-pyrolysis grown films, due to the surface roughness which was causing a high depolarization of the light. The smoothness of the PLD grown samples, instead, enable this type of study as it will be outlined in paragraph 5.5.2.Furthermore, a better understanding of the limit to resistivity was possible by doping with Mg.

5.5.1. Target preparation and thin film deposition

Chromium oxide and chromium oxynitride have been previously reported in literature, starting from either metallic or ceramic targets[44,47,74]. In the present thesis, only ceramic targets have been employed due to the possibility of preparing them in house, as this was giving an extra degree of flexibility in choosing their composition. Targets were prepared by solid state reaction. For this purpose, fine powders of appropriate precursors were

mixed in a mortar and finely grounded. For undoped Cr_2O_3, nano-powders were used. For Mg doped films, magnesium carbonate was added in order to have ratios of Mg:Cr of 3:97, 5:95, 6:94 and 8:92. In order to have a complete decomposition of the carbonate residual, leaving Mg as a dopant, powders were homogenised and then thermally treated at 1173K for 24 hrs. After the thermal treatment, XRD patterns of the prepared powders were collected, as shown Figure 5.17

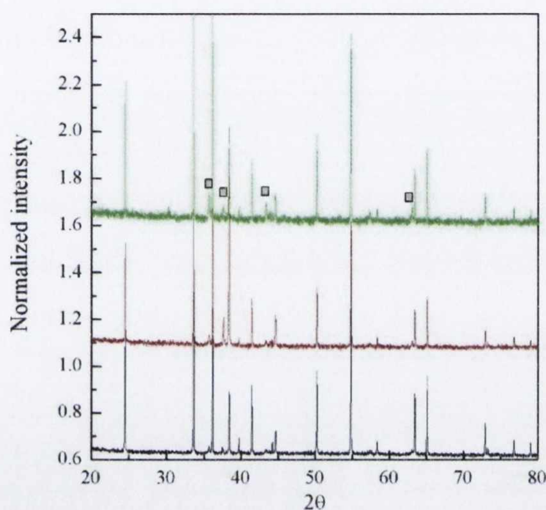

Figure 5.17 XRD patterns of the powders for the target preparation after the first thermal cycle for different Mg:Cr ratios: (—)3:97, (—)5:95, (—) 8:92 . The peaks relative to the $MgCr_2O_4$ are indicated with a square.

According to the XRD analysis, a spurious phase, magnesium dichromate, was present in all of the three patterns as a result of a limited solubility of Mg in Cr_2O_3.

Following, the powders were grounded in a mortar with the addition of few droplets of a solution of polyvinyl alcohol (PVA) in isopropanol (IPA) (15% w/w). This was necessary in order to preserve the integrity of the target during the following annealing steps. The powders were then pressed into pellets and sintered in air for at least 72 hrs. at 1273K.

For the deposition, the target were placed in the appropriate holder and they were kept rotating during the ablation. Prior to ablation, the chamber was evacuated to a pressure lower than 1×10^{-6} bar. Following, the Al_2O_3 substrates were annealed for 2 hrs. at 873K in an oxygen environment

(pressure of 100 μbar). Afterwards the targets were pre-ablated with fluency of roughly 0.3 J/cm^2 and repetition rate of 20 Hz for 5 minutes in order to eliminate any contaminants from the top of the surface. In the screening procedure different conditions of pressure, substrate temperature and laser fluency were tested. After deposition samples were subjected to XRD, XRR and AFM analysis. Optimum growth conditions were achieved at 773K, laser fluency of 0.3-0.5 J/cm^2, substrate to target distance of 7.5 cm and oxygen back-pressure of 100 μbar. These values of laser fluency are quite low in comparison to those normally used for oxides (around 1 J/cm^2), most likely because the in-house made target density is not high enough (maximum density achieved of about 80% of the tabulated density value). These conditions were chosen as a trade-off as lower fluencies lead to a very low ablation rate and therefore low deposition rate, while higher laser fluencies produce rougher films. With a laser fluency of 0.3 J/cm^2 a growth rate of 0.3 Å/min was achieved.

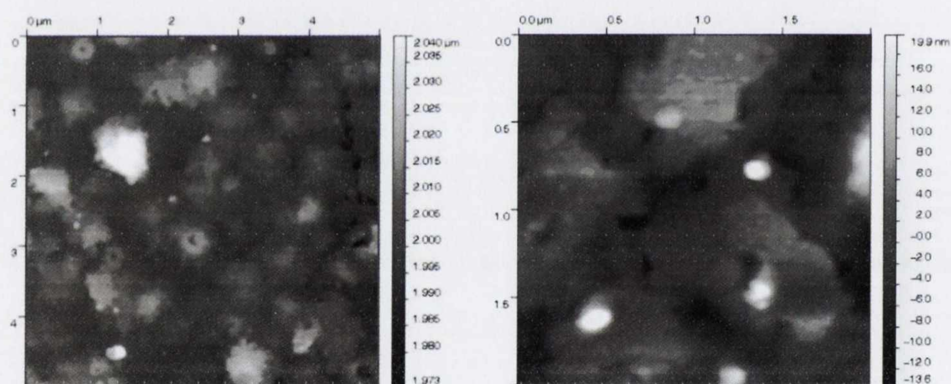

Figure 5.18. Comparison between two samples grown by using different laser fluency. On the left the sample grown by using a fluency of 1J/cm^2 has a rms surface roughness of 8 nm while on the right the sample grown by using a fluency of 0.3 J/cm^{2}has a surface rms roughness of 5 nm

Samples were subjected to XRD characterization in order to verify the crystal quality of the film deposited and the epitaxial relationship with respect to the substrate. Out of plane and in plane scan were performed, an example of which is shown in Figure 5.19.

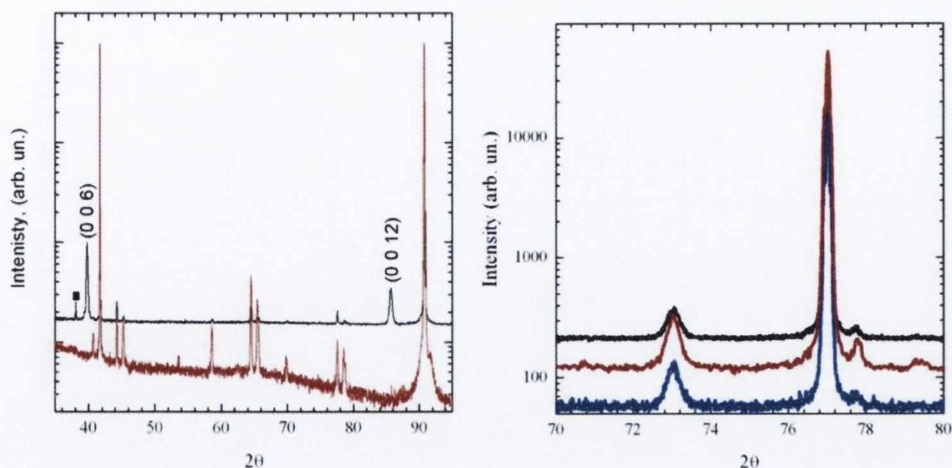

Figure 5.19On the left: the out of plane XRD scan of a Cr_2O_3 film grown on sapphire (—). The substrate pattern is given as a reference (—). The symbol ■ indicate a peak coming from the Ag paint used to load the substrate in the PLD sample holder. On the right: the in plane scan of Cr_2O_3 showing both the substrate and the epilayer reflexes at the same ψ angle: (—)ψ=0, (—)ψ=120 and (—)ψ=240

In the out of plane scans, only the Cr_2O_3 and Al_2O_3 were present. Sometimes residual peaks coming from the Ag paint used to mount the samples could be detected for some samples. From the relative position of (0 0 6) and (0 0 12) reflex of the Cr_2O_3 phase with respect to the same reflex of the Al_2O_3 phase, it could be seen that the films were completely relaxed and no residual strain was present. Indeed, this was an expected result as the critical thickness is 5 nm.

In order to determine the epitaxial relationship, the presence of the (1, 0, 10) reflexes of both phases were analysed as a function of the Ψ angle. As it can be seen in Figure 5.19, both reflexes are present at the same Ψ angles, an indication that no in-plane rotation is present in the deposited layer with respect to the substrate. As a confirmation, a Ψ scan was performed, and diffraction patterns were found at 120° rotation, demonstrating the 3 fold symmetry of this particular plane.

The same analysis was performed on a doped film. The out of plane scan of two films, one doped with a Cr:Mg ratio of 95:5, the other with a ratio of 92:8 are shown in Figure 5.20.

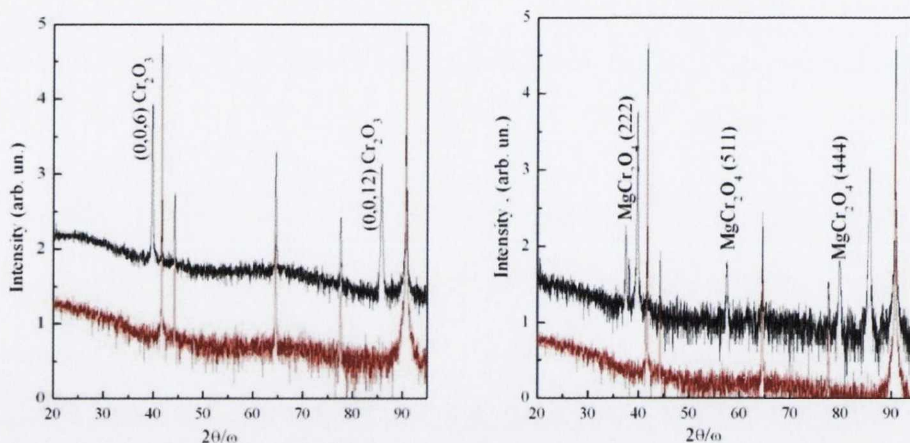

Figure 5.20Out of plane XRD patterns of Cr_2O_3:Mg samples (—). A pattern relative to the bare substrate (Al_2O_3) is reported for comparison (—). On the left, the sample with x=0.05 shows only the peaks attributed to the Cr_2O_3 phase. On the right, the sample with x=0.08 show a secondary phase, magnesium dichromate.

Up to a nominal ratio of Cr:Mg of 94:6, no spurious peak is present, while for a ratio of 92:8, a secondary phase, magnesium dichromate ($MgCr_2O_4$) was identified in the deposited films. Since these ratios represent only the Mg concentration in target, it was necessary to verify the actual content of Mg in the film. For this reason XPS measurements were performed. According to the survey scans, carbon contaminations were present on top of the surface of the as grown samples due to the exposure to the ambient atmosphere during the transfer from the deposition chamber to the XPS apparatus, limiting the signal to noise ratio. For this reason it was necessary to performed sputter cleaning. The sputtering conditions were the following: 0.5 kV beam energy, 1.4μA target current, 1.0×10^{-5}Ar pressure, 5 minutes.

From the analysis of the Mg concentration in the film, it was demonstrated that the transfer from the target was almost stoichiometric (Figure 5.21). This is quite remarkable in comparison to the spray pyrolysis grown films as in the latter case no spurious phase were detected up to a Mg to Cr ratio of 15:85. For epitaxial film, instead, half of the Mg concentration was sufficient to induce phase separation.

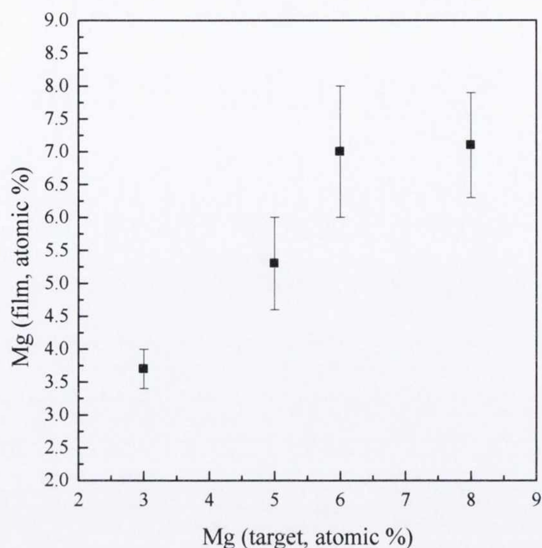

Figure 5.21 Mg concentration incorporated in the deposited film with respect to the relative target composition. Determination has been carried out by XPS measurements.

Electrical properties were determined by measuring the sheet resistance and the activation energy over a temperature range from 323 to 423 K. Resistivity values were compared.The resistivities of the samples grown by PLD are remarkably lower than those obtained from only Mg doped sample and in line with the (Mg,N)-co-doped samples grown by spray pyrolysis. The minimum resistivity for the PLD grown films was obtained with a ratio Cr:Mg of 95:5, and was determined to be 3 Ωcm. This compares with the 15 Ωcm of the only Mg-doped and with the average 5 Ωcm of (Mg,N)-codoped samples (minimum resistivity achieve in the co-doped case 3 Ωcm) grown by spray pyrolysis. Activation energies are also lower than those obtained by spray pyrolysis: 170 meV for the PLD grown samples, 190 meV for the Mg,N-codoped samples, and 200meV for the only Mg-doped samples grown by spray pyrolysis.

5.5.2. Ellipsometric determination of the Cr_2O_3 dielectric function

Fewliterature reports deal with the dielectric function of Cr_2O_3[75-78]. However, none of them gives a complete dielectric model able to correlate the structures present in the dispersion of n and kwith physical optical transitions as according to band structure calculation. High scattering in the determined dielectric functions was present, with all the values of dielectric function determined on polycrystalline or amorphous films. Moreover Uekawa and Kaneko[40] reported that upon Mg doping, an increase in the absorption coefficient was noticed from UV-Visible spectrophotometer measurements. Therefore the optical properties of epitaxial grown films were further investigated by spectroscopic ellipsometry (SE). For this purpose, the spray pyrolysis deposited samples were not useful as the roughness at the surface was very high, resulting in depolarization of the light upon reflection and therefore the only possible method to determine the absorption coefficient was by using the transmission data and applying the Beer's law. Even the for the PLD grown samples only those grown under optimized laser fluency were smooth enough to be suitable foranalysis. Only ellipsometric measurements were performed since UV-Visible spectroscopy could not be usedas it was not possible to completely remove the Ag paint from the rough back of the substrates, and even a small residue of such absorbing material can interfere with measurements. In order to get a complete picture, samples grown by molecular beam epitaxy (MBE) by Dr. Sumesh Sofin were also subjected to investigation. For those MBE samples whose size was big enough to fit the spectrophotometer sample holder, transmission measurements were performed as well.

In order to determine the dielectric function, the thickness was estimated from x-ray reflection (XRR) measurement and this was used to perform the point to point calculation to extract the n and k dispersion (and therefore the dielectric function) from the ellipsometric measurements. By evaluating the line shapes and at the structures present in the dielectric

function, a dielectric model was built up. To this end, the lowest number of fitting parameters was used, trying to attribute a physical meaning to each of them. For this purpose, the structures present in the point to point calculation, the previous results from transmission measurements on spray pyrolysis grown samples and the data from the literature overviewwere taken into account[59-61]. In this way 4 different transitions were identified. In the first attempt, 4 Lorentian oscillators were used for the dielectric model. However these were not enough to get a good fitting on the ellipsometric data and the use of a polynomial equation was required in order to achieve a good matching. The drawback of this approach was that no physical meaning could be attributed to the polynomial variables, which were used only as fitting parameters. This made the comparison between optical transitionsand the band structure calculation performed by Prof. Watson's research group quite difficult. Moreover, in the future, the plan is to study the effect of specific defects introduced in a controlled manner on the optical properties. For this reason a second dielectric model was developed, which includes four critical points according to the optical transition reported in literature and a constant dielectric background, ε_∞. The transitions associated to each critical point are the following:

- 2 excitonic standard critical points to simulate the d-d transition reported at 2.06 and 2.7 eV
- 3D bulk critical point to represent the band gap, usually reported at 3.4 eV
- a single excitonic critical point to reproduce the further absorbance peaks reported in the UV region of the spectra,

Data were collected at an angular range close to the pseudo Brewster angle (69°,71°,73°) over an energy range spanning from 1.5 to 5 eV by Mr. Christopher Smith, using a micro-spot due to the small size of the sample. In this way the spot size could be reduced to about 300 μm. For the fitting, the thickness as determined by XRR measurements was used as an input parameter, in order to reduce the number of free variables. Intensity, position and broadening of the peak as well as the value of ε_∞ were optimized.

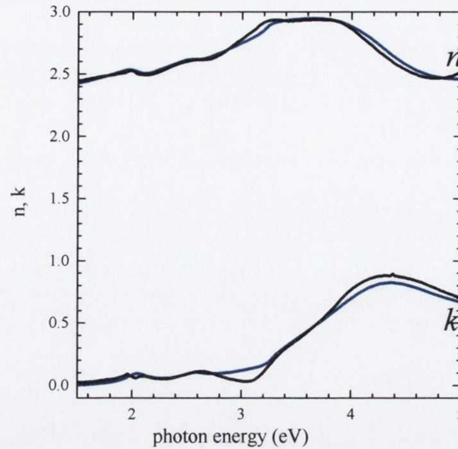

Figure 5.22 Comparison between the n and k as determinedfrom the point to point calculation (—) with the dispersion as determined from the model (—) for a sample grown by MBE.

In order to assess the quality of the model, comparison with the n,k as determined from the point to point calculation was made for each sample, and the level of the agreement was used to judge the quality of the model itself (Figure 5.22).

Regarding the general line shape, this is mostly given by the structure introduced by the 3D bulk critical point. This by itself will be able to account for the dispersion in the dielectric function.The fitting improves when the 2 excitonic critical points are included as they introduce the 2 weak transitions in the visible part of the spectra. Above 3.5 eV the 3D critical point is not able to account for all the absorption and therefore another excitonic critical points is require to reproduce the transition happening in this spectra region. Regarding the energy region around the band gap, (from 3 eV to 3.6 eV), the general line shape is reproduced; however the fine structure is not perfectly reconstructed, even when the phase of the 3D critical point was optimized. This means that probably the shape of the band structure around the band gap is not perfectly parabolic. However at this stage, without any further input from theoretical calculation, it is difficult to assess this issue only from the experimental point of view.

Only for MBE grown samples, both transmission and ellipsometric measurements were available, and therefore it was possible to verify the

accuracy of the fitting procedure, and thus, the reliability of the data extracted. In fact there is an intrinsic limitation in the accuracy of the k values as determined by spectroscopic ellipsometry due to a limited thickness of the sample. All the samples measured had thicknesses values spanning from 30 to 60 nm. In this range, for semi-transparent and transparent materials, reflectance measurements are mostly sensitive to n rather than k. Transmission measurements will be more sensitive to absorption. In order to verify this latter contribution, Dr. K. Fleischer performed the refinement by including the transmission data in the fitting routine, however, only a marginal increase in the k value was obtained (Figure 5.23), and the transmission data were already well fitted by using the complex refractive index extracted by the ellipsometric model.

For the spray pyrolysis grown films, however, no ellipsometric data were available, but only transmission measurements. Thus, it was important to verify if there was any significant difference between the two methods used to extract the absorption coefficient: α from transmission measurements via the Beer's law versus α from ellipsometric measurements via the extinction coefficient ($\alpha=4\pi k/\lambda$). For this purpose, the two methods were used to determine the alpha for the same MBE grown sample. As it can be seen from Figure 5.22, there is quite a mismatch between the two lines. This mismatch is due to the fact that a systematic error is introduced in the determination of alpha from transmissions measurements only. In fact, due to the small size of the sample it was not possible to perform reflectance measurements. This means that, the light which is reflected, is still considered as absorbed in this determination. In other words, the absorption coefficient, determined via transmission measurements, is overestimated by a quantity equals to the reflectance of the films, which is not properly treated. As already mention, reflectance measurements could not be performed due to the lack of an appropriate sample holder. Thus values determined by spectroscopic ellipsometry are the most reliable. However, this type of measurements could not be performed on spray deposited films due to their high roughness. For these, only transmittance data were available. Therefore in order to perform a fair comparison, for

MBE grown samples the value of alpha extracted from only transmission measurements will be used, though acknowledging all the limitation of this latter approach.

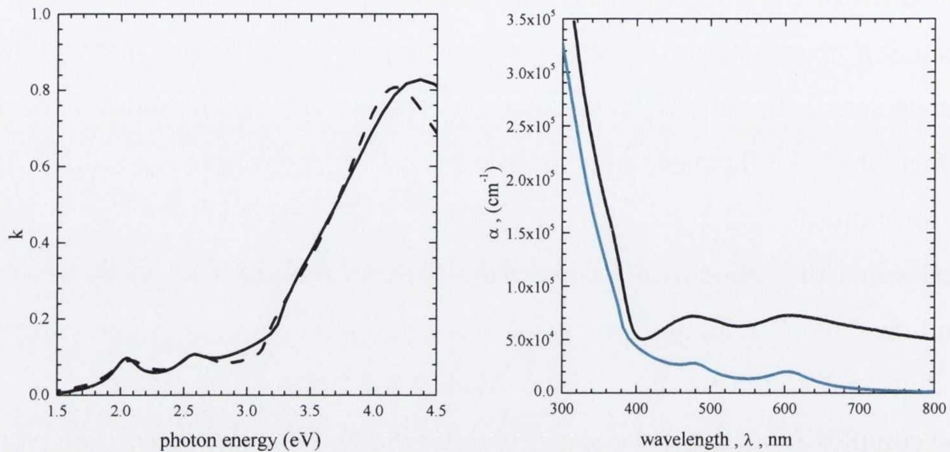

Figure 5.23 Comparison between the k values as derived from a fitting procedure which includes (--) the transmission measurements with respect to the same derived from a fitting routine based only on the SE data (—). It is worth noting that the absorption coefficient as determined from transmission measurements (—) is quite different in comparison to that determined from ellipsometric measurements (—).

Regarding the MBE sample, under-stoichiometric and stoichiometric Cr_2O_3 films were grown, as determined from XRD measurements (Figure 5.24). No major differences in the optical response could be seen between the 2 set of samples.

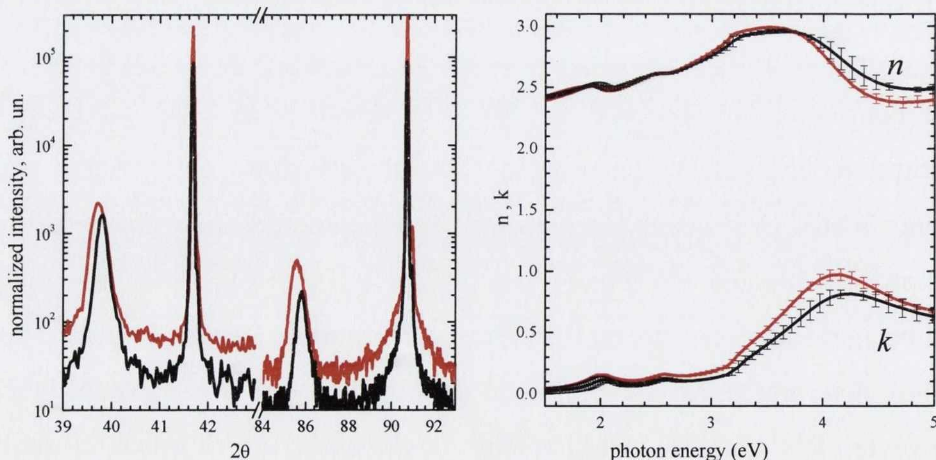

Figure 5.24 XRD pattern of (—)under-stoichiometric and (—)stoichiometric Cr_2O_3 grown by MBE. The difference in stoichiometry has only marginal effect on the optical properties (n,k) as determined by spectroscopic ellipsometry

The n and k are reported in Figure 5.25for both MBE and PLD samples. In both cases the dominant absorption and dispersion is introduced by the 3D critical point around the band gap, which by itself would be able to reproduce the line-shape of the dielectric function. As shown in Figure 5.25, there is quite a difference between the n and k calculated for MBE and PLD samples.

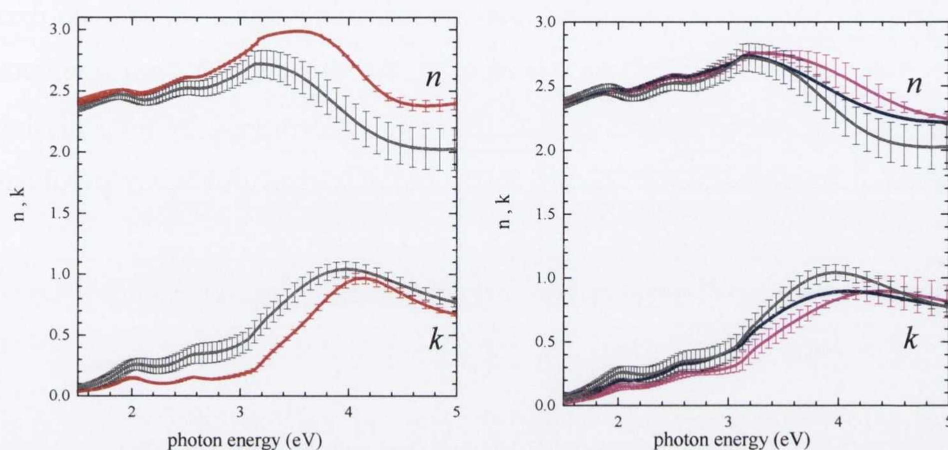

Figure 5.25 On the left. The n, k dispersion as determined for undoped Cr_2O_3 grown by (—) MBE and (—)PLD. On the right, the n and k determined of undoped (—) and Mg doped (0.03, —; 0.05, —) grown by PLD.

From the crystallographic point of view, both samples are similar (perfectly stoichiometric epitaxial Cr_2O_3, 0001 oriented), while from the XRR point of view, samples grown by MBE are denser than both the tabulated values and the PLD grown films. Moreover, from the morphological point of view, samples grown by PLD are slightly rougher (rms = 5 nm) than MBE samples (rms = 2.5 nm). An attempt was made to insert the roughness into the fitting routine, by using the Bruggeman model, however, during the fitting routine itself the thickness of this extra layer was reduce to zero. At the same point, no improvement in the fitting was obtained when this layer was inserted.

Following Mg-doped samples were measured and analyzed by using the same dielectric model as described above. Within the experimental error no change was detected in the extinction coefficient between undoped and doped samples. This result is in contradiction with respect to those reported by Uekawa and Kaneko but in agreement with previous results from spray

pyrolysis grown material for which the value of absorption coefficient determined for Cr_2O_3 was not affected by the presence of Mg. In other words, for both samples the determined absorption coefficient coincides within the experimental error.

Because of the difference in the absorption coefficient as determined from transmission and from SE measurements, for the MBE grown sample, transmission measurements were used to determine alpha. Since such data were not available for PLD grown samples, the ellipsometric measurements were used. These were compared to the values determined by transmission measurements for undoped and N-doped samples grown by spray pyrolysis (Figure 5.26).

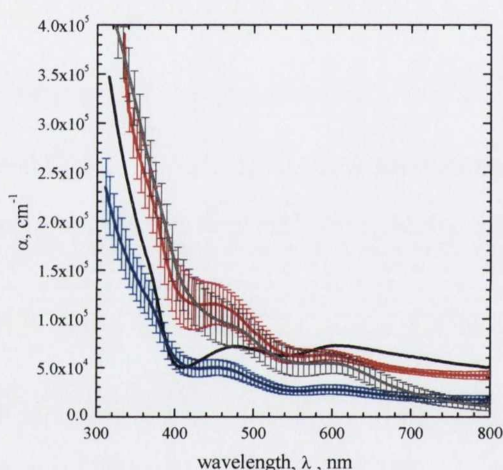

Figure 5.26. Comparison between the absorption coefficients calculated from transmission measurements for (—) undoped and (—) nitrogen doped Cr_2O_3 grown by spray pyrolysis, transmission measurement for an undoped samples grown by MBE (—)and the absorption coefficient calculated from the extinction coefficient for (—) PLD grown samples. The error bars are representative of the scattering between different samples grown with the same technique.

As it can be seen from Figure 5.26 the absorption coefficients as determined from the PLD samples coincide, within the experimental error, with the absorption coefficient of undoped Cr_2O_3 grown by spray pyrolysis. Similar absorption coefficients were found for undoped spray pyrolysis grown samples and MBE grown sample in the visible portion of the spectra, while, around the band gap, the absorption of MBE grown samples coincides with that of N-doped samples. As it can be seen, the line-shape of

the MBE grown samples is different from the others. This is probably due to the superimposition of a Fabry-Perot oscillation, however, further investigations are required in order to confirm it.

5.6. Conclusions on the optical and electrical properties of undoped and doped Cr_2O_3

Cr_2O_3 undoped and Mg-doped was grown by PLD. The samples were subjected to both optical and electrical analysis. An optical model was developed able to reproduce the ellipsometric measurements for all the samples.

Undoped samples were insulating with optical properties comparable to those of undoped Cr_2O_3 grown by spray pyrolysis. Samples doped with Mg have a better conductivity and lower activation energies than those grown by spray pyrolysis. No differences in the optical properties were observed with respect to undoped samples. However a quite remarkable difference was determined in comparison to undoped samples grown by MBE. In this case a lower extinction coefficient was observed with properties quite comparable to those of N-doped samples grown by spray pyrolysis, at least around the band gap. However, one needs to be careful in comparing the optical response as determined from spectroscopic ellipsometry with respect to UV-visible spectrophotometer measurements. In fact, as shown for MBE grown samples, systematic difference were observed between the two cases. A further improvement in the analysis is expected once an appropriate sample holder for small size samples will be available for the integrating sphere spectrophotometer. This will enable both transmittance and reflectance measurements for all the samples, reducing systematic errors when absorption is calculated from transmission measurements alone. Nevertheless, this comparison leads to the conclusion that for undoped chromium oxide, both PLD and spray pyrolysis grown

samples show a broad band absorption which increases the absorption coefficient in comparison with N-doped samples. The reasons for this are still under investigation, however, point defects such as the presence of Cr(VI), for example, have been already reported in literature as the cause of such absorption. At the same time, this shows that, despite the defective nature of Cr_2O_3:(Mg,N) grown by spray pyrolysis, the latter still show the lowest absorption coefficient in the visible range, demonstrating the importance of nitrogen in modifying the optical properties of this material. Future experiments will aim to clarify if the presence of reactive nitrogen (plasma) in the deposition environment, will lead to a comparable reduction of the absorption coefficient for samples grown by PLD and MBE.

(1) Sato, H.; Minami, T.; Takata, S.; Yamada, T. *Thin Solid Films* **1993**, *236*, 27-31.

(2) Kawazoe, H.; Yasukawa, M.; Hyodo, H.; Kurita, M.; Yanagi, H.; Hosono, H. *Nature* **1997**, *389*, 939-942.

(3) Zhang, X.; Li, X. M.; Chen, T. L.; Zhang, C. Y.; Yu, W. D. *Applied Physics Letters* **2005**, *87*, -.

(4) Schulz, C.; Ulrich, S.; Szyszka, B. *Vakuum in Forschung und Praxis* **2012**, *24*, 12-16.

(5) Tate, J.; Ju, H. L.; Moon, J. C.; Zakutayev, A.; Richard, A. P.; Russell, J.; McIntyre, D. H. *Physical Review B* **2009**, *80*, -.

(6) Banerjee, A. N.; Chattopadhyay, K. K. *Progress in Crystal Growth and Characterization of Materials* **2005**, *50*, 52-105.

(7) Yanagi, H.; Inoue, S.-i.; Ueda, K.; Kawazoe, H.; Hosono, H.; Hamada, N. *Journal of Applied Physics* **2000**, *88*, 4159-4163.

(8) Sheng, S.; Fang, G.; Li, C.; Xu, S.; Zhao, X. *physica status solidi (a)* **2006**, *203*, 1891-1900.

(9) Tate, J.; Jayaraj, M. K.; Draeseke, A. D.; Ulbrich, T.; Sleight, A. W.; Vanaja, K. A.; Nagarajan, R.; Wager, J. F.; Hoffman, R. L. *Thin Solid Films* **2002**, *411*, 119-124.

(10) Nagarajan, R.; Draeseke, A. D.; Sleight, A. W.; Tate, J. *Journal of Applied Physics* **2001**, *89*, 8022-8025.

(11) Hidenori, H.; Kazushige, U.; Hiromichi, O.; Masahiro, H.; Toshio, K.; Hideo, H. *Applied Physics Letters* **2003**, *82*, 1048-1050.

(12) Ueda, K.; Inoue, S.; Hirose, S.; Kawazoe, H.; Hosono, H. *Applied Physics Letters* **2000**, *77*, 2701-2703.

(13) Hosono, H. *International Journal of Applied Ceramic Technology* **2004**, *1*, 106-118.

(14) Anderson, J.; Chris, G. V. d. W. *Reports on Progress in Physics* **2009**, *72*, 126501.

(15) D. Ginley, H. H., D.C. Paine *Handbook of transparent conductors*; Springer: New York, 2010.

(16) Kawazoe Hiroshi; Yanagi Hiroshi; Ueda Kazushige; Hideo, H. *MRS Bulletin* **2000**, *25*, 28-36.

(17) Antonio Facchinetti, T. J. M. *Transparent electronics From synthesis to application*; Wiley, 2010.

(18) Sheng, S.; Fang, G. J.; Li, C.; Xu, S.; Zhao, X. Z. *Physica Status Solidi a-Applications and Materials Science* **2006**, *203*, 1891-1900.

(19) Exarhos, G. J.; Windisch, C. F.; Ferris, K. F.; Owings, R. R. *Applied Physics a-Materials Science & Processing* **2007**, *89*, 9-18.

(20) Lynch, C. C. B.; Egdell, R. G.; Law, D. S. L. *Chemical Physics Letters* **2005**, *401*, 223-226.

(21) Ohta, H.; Kamiya, M.; Kamiya, T.; Hirano, M.; Hosono, H. *Thin Solid Films* **2003**, *445*, 317-321.

(22) Dekkers, M.; Rijnders, G.; Blank, D., H. A. *Applied Physics Letters* **2007**, *90*, 021903.

(23) Mansourian-Hadavi, N.; Wansom, S.; Perry, N. H.; Nagaraja, A. R.; Mason, T. O.; Ye, L.-h.; Freeman, A. J. *Physical Review B* **2010**, *81*, 075112.

(24) Mizoguchi, H.; Hirano, M.; Fujitsu, S.; Takeuchi, T.; Ueda, K.; Hosono, H. *Applied Physics Letters* **2002**, *80*, 1207-1209.

(25) Narushima, S.; Mizoguchi, H.; Shimizu, K.; Ueda, K.; Ohta, H.; Hirano, M.; Kamiya, T.; Hosono, H. *Advanced Materials* **2003**, *15*, 1409-1413.

(26) Scanlon, D. O.; Watson, G. W. *Physical Chemistry Chemical Physics* **2011**, *13*, 9667-9675.

(27) Guo, W.; Fu, L.; Zhang, Y.; Zhang, K.; Liang, L. Y.; Liu, Z. M.; Cao, H. T.; Pan, X. Q. *Applied Physics Letters* **2010**, *96*, 042113-1,3.

(28) Ogo, Y.; Hidenori, H.; Kenji, N.; Hiroshi, Y.; Toshio, K.; Masahiro, H.; Hideo, H. *Applied Physics Letters* **2008**, *93*, 032113.

(29) Fortunato, E.; Raquel, B.; Pedro, B.; Vitor, F.; Sang-Hee Ko, P.; Chi-Sun, H.; Rodrigo, M. *Applied Physics Letters* **2010**, *97*, 052105.

(30) Hosono, H.; Ogo, Y.; Yanagi, H.; Kamiya, T. *Electrochemical and Solid-State Letters* **2011**, *14*, H13-H16.

(31) Hosono, H.; Ohta, H.; Hayashi, K.; Orita, M.; Hirano, M. *Journal of Crystal Growth* **2002**, *237-239*, 496-502.

(32) Allen, J. P.; Scanlon, D. O.; Parker, S. C.; Watson, G. W. *The Journal of Physical Chemistry C* **2011**, *115*, 19916-19924.

(33) Zunger, A. *Applied Physics Letters* **2003**, *83*, 57-59.

(34) Chen, L.; Xiong, Z.; Wan, Q.; Li, D. *Optical Materials* **2010**, *32*, 1216-1222.

(35) Cao, Y.; Miao, L.; Tanemura, S.; Tanemura, M.; Kuno, Y.; Hayashi, Y. *Applied Physics Letters* **2006**, *88*, 251116.

(36) Chen, L. L.; Lu, J. G.; Ye, Z. Z.; Lin, Y. M.; Zhao, B. H.; Ye, Y. M.; Li, J. S.; Zhu, L. P. *Applied Physics Letters* **2005**, *87*, 252106.

(37) Krtschil, A.; Dadgar, A.; Oleynik, N.; Blasing, J.; Diez, A.; Krost, A. *Applied Physics Letters* **2005**, *87*, 262105.

(38) Wang, X. H.; Yao, B.; Wei, Z. P.; Sheng, D. Z.; Zhang, Z. Z.; Li, B. H.; Lu, Y. M.; Zhao, D. X.; Zhang, J. Y.; Fan, X. W.; Guan, L. X.; Cong, C. X. *Journal of Physics D: Applied Physics* **2006**, *39*, 4568.

(39) T.J. Coutts, J. D. P., D.S. Ginley, T.O. Mason In *195th Meeting of the Electrochemical Society* Seattle, Washington, 1999.

(40) Uekawa, N.; Kaneko, K. *The Journal of Physical Chemistry* **1996**, *100*, 4193-4198.

(41) Holt, A.; Kofstad, P. *Solid State Ionics* **1997**, *100*, 201-209.

(42) Constantin, C.; Haider, M. B.; Ingram, D.; Smith, A. R. *Applied Physics Letters* **2004**, *85*, 6371-6373.

(43) Castaldi, L.; Kurapov, D.; Reiter, A.; Shklover, V.; Patscheider, J. *Journal of Applied Physics* **2011**, *109*, 053720.

(44) Suzuki, T.; Saito, H.; Hirai, M.; Suematsu, H.; Jiang, W.; Yatsui, K. *Thin Solid Films* **2002**, *407*, 118-121.

(45) Urgen, M.; Ezirmik, V.; Senel, E.; Kahraman, Z.; Kazmanli, K. *Surface and Coatings Technology* **2009**, *203*, 2272-2277.

(46) Mientus, R.; Grotschel, R.; Ellmer, K. *Surface and Coatings Technology* **2005**, *200*, 341-345.

(47) Tabbal, M.; Kahwaji, S.; Christidis, T. C.; Nsouli, B.; Zahraman, K. *Thin Solid Films* **2006**, *515*, 1976-1984.

(48) Yuzheng, G.; Stewart, J. C.; John, R. *Journal of Physics: Condensed Matter* **2012**, *24*, 325504.

(49) Catti, M.; Sandrone, G.; Valerio, G.; Dovesi, R. *Journal of Physics and Chemistry of Solids* **1996**, *57*, 1735-1741.

(50) Zimmermann, R.; Steiner, P.; Hufner, S. *Journal of Electron Spectroscopy and Related Phenomena* **1996**, *78*, 49-52.

(51) Dera, P.; Lavina, B.; Meng, Y.; Prakapenka, V. B. *Journal of Solid State Chemistry* **2011**, *184*, 3040-3049.

(52) Gaudry, É.; Sainctavit, P.; Juillot, F.; Bondioli, F.; Ohresser, P.; Letard, I. *Physics and Chemistry of Minerals* **2006**, *32*, 710-720.

(53) Mejias, J. A.; Staemmler, V.; Freund, H. J. *Journal of Physics: Condensed Matter* **1999**, *11*, 7881.

(54) Zaanen, J.; Sawatzky, G. A.; Allen, J. W. *Physical Review Letters* **1985**, *55*, 418-421.

(55) Li, X.; Liu, L.; Henrich, V. E. *Solid State Communications* **1992**, *84*, 1103-1106.

(56) Shi, S.; Wysocki, A. L.; Belashchenko, K. D. *Physical Review B* **2009**, *79*, 104404.

(57) Olalde-Velasco, P.; Jimenez-Mier, J.; Denlinger, J. D.; Hussain, Z.; Yang, W. L. *Physical Review B* **2011**, *83*, 241102.

(58) Rohrbach, A.; Hafner, J.; Kresse, G. *Physical Review B* **2004**, *70*, 125426.

(59) Mejias, J. A.; Staemmler, V.; Freund, H. J. *Journal of Physics: Condensed Matter* **1999**, *11*, 7881-7891.

(60) Allos, T. I. Y.; Birss, R. R.; Parker, M. R.; Ellis, E.; Johnson, D. W. *Solid State Communications* **1977**, *24*, 129-131.

(61) Brik, M. G.; Avram, N. M.; Avram, C. N. *Solid State Communications* **2004**, *132*, 831-835.

(62) Chambers, S. A.; Williams, J. R.; Henderson, M. A.; Joly, A. G.; Varela, M.; Pennycook, S. J. *Surface Science* **2005**, *587*, L197-L207.

(63) Qin, P.; Fang, G.; He, Q.; Sun, N.; Fan, X.; Zheng, Q.; Chen, F.; Wan, J.; Zhao, X. *Solar Energy Materials and Solar Cells* **2011**, *95*, 1005-1010.

(64) Lim, S. H.; Desu, S.; Rastogi, A. C. *Journal of Physics and Chemistry of Solids* **2008**, *69*, 2047-2056.

(65) Kudo, A.; Yanagi, H.; Hosono, H.; Kawazoe, H. *Applied Physics Letters* **1998**, *73*, 220-222.

(66) Duan, N.; Sleight, A. W.; Jayaraj, M. K.; Tate, J. *Applied Physics Letters* **2000**, *77*, 1325-1326.

(67) Jayaraj, M. K.; Draeseke, A. D.; Tate, J.; Sleight, A. W. *Thin Solid Films* **2001**, *397*, 244-248.

(68) Ueda, K.; Hase, T.; Yanagi, H.; Kawazoe, H.; Hosono, H.; Ohta, H.; Orita, M.; Hirano, M. *Journal of Applied Physics***2001**, *89*, 1790-1793.

(69) Arca, E.; Fleischer, K.; Shvets, I. V. *Applied Physics Letters* **2011**, *99*, 111910-1, 111910-3.

(70) Tronche, A.; Fauchais, P. *Materials Science and Engineering* **1987**, *92*, 133-144.

(71) Misho, R. H.; Murad, W. A.; Fattahallah, G. H. *Thin Solid Films* **1989**, *169*, 235-239.

(72) Holt, A.; Kofstad, P. *Solid State Ionics***1999**, *117*, 21-25.

(73) Soto, G.; de la Cruz, W.; Farias, M. H. *Journal of Electron Spectroscopy and Related Phenomena* **2004**, *135*, 27-39.

(74) Popovici, N.; Parames, M. L.; Da Silva, R. C.; Monnereau, O.; Sousa, P. M.; Silvestre, A. J.; Conde, O. *Applied Physics A* **2004**, *79*, 1409-1411.

(75) Hones, P.; Diserens, M.; Levy, F. *Surface and Coatings Technology* **1999**, *120-121*, 277-283.

(76) Ivanova, T.; Gesheva, K.; Cziraki, A.; Szekeres, A.; Vlaikova, E. *Journal of Physics: Conference Series* **2008**, *113*, 012030.

(77) Lai, F. D.; Huang, C. Y.; Chang, C. M.; Wang, L. A.; Cheng, W. C. *Microelectronic Engineering* **2003**, *67-68*, 17-23.

(78) Al-Kuhaili, M. F.; Durrani, S. M. A. *Optical Materials* **2007**, *29*, 709-713.

Chapter 6

Concluding remarks and future prospective.

6.1 Conclusions and outlook

This PhD study has been devoted to the synthesis and optimization of transparent conductive oxides with particular regards to their possible implementation in solar cell devices. This latter aspect is presently on-going within the scheme of the Ulysses project.

The thesis discusses two main strands, according to the classification of TCOs as n-type or p-type depending on the type of carriers responsible for the conductivity. Prospective and goals for these two main subjected are rather different.

For the n-type TCO, focus was on basic studies, in particular the relationship between the physical properties of deposited films and how these relate to the different chemicals used. This offered also the opportunity to get a better understanding of the deposition technique and explore its limits. The following two applications were pursued: the first deals with the tuning of the optical properties, in particular the refractive index of ZnO to use it as an internal antireflecting layer for minimizing the loss due to the index mismatch between the front glass and the TCO. Aluminium was used for this purpose, and the capability of this material to fulfill this tasked was assessed from a theoretical point of view by Dr. Fleischer. In the near future this material will be tested in a real device. The second application was to find an alternative precursor for the synthesis of FTO. At the time the study was performed, BSF as a source of fluorine looked promising as it was still classified as non-toxic. Regardless the fact that this classification was changed, this precursor turned out to be an effective fluorine source and doped samples showed improved conductivity and degenerate behaviour in comparison to the semiconducting undoped tin oxide.

In the second part of the thesis, the deposition and the properties of a new p-type TCO will be discussed. This task was accomplished by co-doping of $Cr_2O_3$with Mg and N. The effect of the two elements, combined together, produced a p-type TCO with performance comparable, in terms of figure of merit, to many TCOs reported so far, despite the acknowledged

limitation of the deposition technique used. The deposition of such material opened a number of questions, which could be answered only partially during the course of the present PhD study. The role of Mg is so far the clearest, being a dopant in classical terms. As demonstrated by the growth of Mg doped films by PLD, the crystal quality influences the electrical properties, i.e. the epitaxial films have a 5 times better conductivity than the polycrystalline films prepared by SP. It has to be noted that the minimum conductivity reached for the epitaxial grown films is comparable with that of the co-doped films, proving the success of the co-doping approach. So far there are 2 possible explanations for that: the first is that a Mg-N complex is formed, an indication of which was found in the increased parameter *a* of the crystal structure for co-doped films with respect to the database value. On the other side, the reaction between nitrate and ammonium ions could be responsible for the enhanced conductivity, due to the formation of NO_x species in the reaction atmosphere. In order to verify which one of the above is responsible for the higher conductivity of co-doped samples, it will be necessary to grow the same type of sample by using a different technique.

Regarding the optical properties, the effect of the nitrogen has still to be clarified. Direct measurement of the nitrogen concentration by XPS is complicated by the surface sensitivity of the technique and by the reaction taking place upon Ar sputtering. So far only an indirect confirmation could be given, i.e. the band gap opening and the increase in the crystal lattice parameter *a*. Direct determination of the nitrogen content will be performed by x-ray absorption at the Synchrotron facilities of the Maxlab, Sweden. Comparison with epitaxial undoped films grown by MBE and PLD confirm the importance of the N in the reaction environment, as N-doped samples still show a lower absorption coefficient with respect to undoped samples in the visible range of the spectra. Regarding the n and k dispersion, differences could be found between samples grown by MBE and PLD, with the latter having a higher extinction coefficient. It has to be clarified if this difference is due a systematic overestimation of the absorption coefficient of the films grown by PLD because of a higher roughness or if thiscoincides with the previously reported broadband absorption due to the presence of chromium in different oxidization states.

Regardless of these fundamental questions, it will be still interesting to explore the possibility of using these materials as buffer layers in organic solar cells. To this end, undoped and Mg-doped films will be tested in real devices, thanks to the collaboration with the University of Nantes.

Appendix

Appendix A1: DFT calculations of the band structure of Cr_2O_3 and $Mg:Cr_2O_3$

Development of a new p-type transparent conducting oxide was achieved, from an experimental point of view, by co-doping of Cr_2O_3 with Mg and N. In order to get a better understanding of the doping mechanisms and in order to assess the role of each single element on both electrical and optical properties, comparison with theoretical calculation is required. To this end, collaboration with prof. Graeme Watson and Dr. David Scanlon was established.

Density functional theory calculations were performed by Ms. Aeofa Kehoe under the supervision of prof. Graeme Watson and Dr. David Scanlon.

All density functional theory (DFT) calculations were carried out using the Vienna ab initio simulation package (VASP)[1], which employs periodic boundary conditions to expand crystal wave functions in terms of a plane-wave basis and describe valence electronic states. Calculations were performed with the general gradient approximation (GGA) of Perdew, Burke, and Ernzehoff[2] and included a Hubbard-like +U term of Dudarev et al. to account for on-site Coulombic interactions[3]. U_{eff} values of 3 eV and 5 eV were applied to the Cr d states and O p states, respectively, and were obtained by comparing the valence band structure of density of states calculations with photoemission spectra in references [4] and [5]. All calculations were spin polarised to simulate the antiferromagnetic structure of the system.

Calculations were performed on a 30 atom hexagonal representation of the unit cell of Cr_2O_3, the lattice parameters of which were optimised by fitting an energy-volume curve to the Murnaghan equation of state[6]. A 2 x 2 x 1 supercell containing 120 atoms was created, and a range of intrinsic and

extrinsic point defects were introduced. The defect formation energies were calculated according to the equation A.1.

$$\Delta H_f(D,q) = \left(E^{(D,q)} - E^{H}\right) + \sum_i n_i \left(E_i + \mu_i\right) + q\left(E_{Fermi} + \varepsilon^{H}_{VBM}\right) + E_{align}[q] \quad \text{A.1}$$

$E^{(D,q)}$ and E^{H} are the energies of the pure and defective cell, respectively. E_i, the elemental reference energies, were found from calculations of the standard states, and n represents the number of each of these types of atom that are formally added to or taken from an external reservoir. The equilibrium growth conditions are considered using the chemical potentials, μ_i, while the electronic chemical potential, E_{Fermi}, ranges from the valence band to the conduction band edges. $\varepsilon^{H}{}_{VBM}$ represents the valence band maximum eigenvalue in pure Cr_2O_3. The alignment term $E_{align}[q]$ both aligns the electrostatic potential between the pure and defective cells, and corrects for finite-size effects in the charged impurities calculations[7]. For a given defect, the thermodynamic transition level for charge states q and q' ($\varepsilon_D(q/q')$) are equal to the Fermi level at which the two charge states have equal energy (Eq A.2)

$$\varepsilon_D(q/q') = \frac{\Delta H^f(D,q) - \Delta H^f(D,q')}{q' - q} \quad \text{A.2}$$

A Γ-centred 6 x 6 x 2 k-point mesh and a Γ-centred 2 x 2 x 2 k-point mesh were employed for the unit cell and 2 x 2 x 1 supercell, respectively. Projector augmented wave (PAW) pseudopotentials were used to describe the interactions between the cores (Cr:[Ar] and O:[He]) and valence electrons. A plane wave cut-off of 400 eV was employed, and calculations were deemed to have converged when the forces on each atom were less than 0.01 eV $Å^{-1}$.

The band structure is reported in Figure A.1.

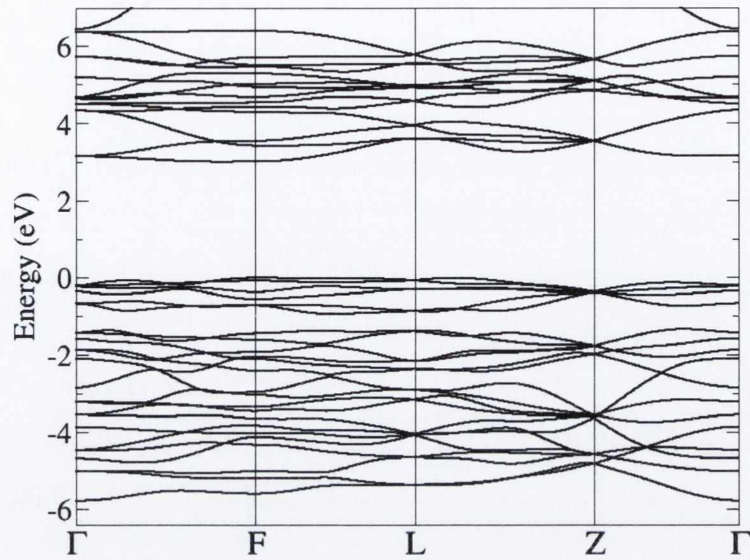

Figure A.1. Band structure calculation of undoped Cr_2O_3

It can be notice that the VBM is rather flat, leading to heavy effective mass, which is in agreement with the poor electrical properties reported in literature for this material. Doping with Mg leads to the introduction of a defect level 400 meV above the VBM. This level is attributed to be responsible for the improved conductivity of Mg:Cr_2O_3 with respect to undoped Cr_2O_3. The fact that this defect is not shallow, explain why the conductivity in low.

(1) G. Kresse and J. Hafner. Phys. Rev. B, **1994**, 49, 14251–14271

(2) J. P. Perdew, K. Burke and M. Ernzerhof. Phys. Rev. Lett., **1996**, 77, 3865

(3) S. L. Dudarev, G. A. Botton, S. Y. Savrasov, C. J. Humphreys and A. P. Sutton. Phys. Rev.B, **1998**, 57, 1505

(4) R. Zimmermann, P. Steiner and S. Hufner J. Electron Spectrosc. Relat. Phenom., **1996,** 79, 49-52

(5)S. A. Chambers, J. R. Williams, M. A. Henderson, A. G. Joly, M. Varela and S. J. Pennycook Surf. Sci., **2005**, 587, L197-L207

(6) F. D. Murnaghan. Proc. Natl. Acad. Sci. USA, **1944**, 30(9), 244–247

(7) C. Freysoldt, J. Neugebauer, and C. G. Van de Walle, Phys. Rev.Lett., **2009**, 102, 016402